BONNMAG A COMPUTER PROGRAM FOR ANGULAR OVERLAP MODELING OF ALL f^n-SYSTEMS: NEW INSIGHTS INTO LIGAND-FIELD SPLITTING OF LANTHANIDE AND ACTINIDE IONS

DISSERTATION ZUR ERLANGUNG DES DOKTORGRADES (DR. RER. NAT.)

DER

MATHEMATISCH-NATURWISSENSCHAFTLICHEN FAKULTÄT

DER

RHEINISCHEN FRIEDRICH-WILHELMS-UNIVERSITÄT BONN

VORGELEGT VON

ANNA BRONOVA (M. SC.)

AUS MOSKAU/RUSSLAND

BONN
AUGUST 2017

Die vorliegende Arbeit entstand in der Zeit vom 01.12.2013 bis zum 15.08.2017 am Institut für Anorganische Chemie und am Mulliken Center für Theoretische Chemie der Mathematisch-Naturwissenschaftlichen Fakultät der Rheinischen Friedrich-Wilhelms-Universität Bonn.

1. Gutachter: Prof. Dr. Robert Glaum
2. Gutachter: Prof. Dr. Thomas Bredow
Tag der Promotion: 19.01.2018
Erscheinungsjahr: 2018
Diese Dissertation ist auf dem Hochschulschriftenserver der ULB Bonn
http://hss.ulb.uni-bonn.de/diss_online elektronisch publiziert.

Schriftliche Versicherung

Hiermit versichere ich, dass ich die vorliegende Dissertation selbstständig verfasst und keine anderen als die angegebenen Quellen und Hilfsmittel benutzt, sowie Zitate kenntlich gemacht habe.

Bonn, 15.08.2017

_____

Anna Bronova

1 Introduction

Lanthanides[1] comprise the elements between lanthanum and lutetium. They were discovered in the 19th and 20th centuries [1]. Their compounds are widely applied in different natural sciences due to their various physical and chemical properties. The special position of the lanthanides in the periodic table is based on their electron configuration. The 4*f* orbitals close to the nucleus are stepwise occupied from lanthanum ([Xe] $4f^0\ 5d^1\ 6s^2$), which might be regarded as true d-block metal to lutetium ([Xe] $4f^{14}\ 5d^1\ 6s^2$).

The chemistry of the lanthanides is of interest to basic and applied research and a large number of technical applications of lanthanide compounds is known. $Nd_2Fe_{14}B$ [2] and $SmCo_5$ [3, 4] are used as permanent magnets due to their high coercivity. $Y_3Al_5O_{12}$ with Y^{3+} substituted by Nd^{3+} is used as solid state laser material [1]. Further applications are to be found in photooptics [5], in the automotive industry, where CeO_2 is used as oxygen storage material in the Three-Way-Catalyst [6] or in enantiopure organic synthesis ($LaLi_3$-tris(binaphthoxide)) [7]. Extremely important and diverse are the applications of the lanthanides in medicine. Ho- or Er-YAG lasers are used in the ophthalmology [8]. Special well-tolerated contrast agents containing gadolinium(III) are used for magnetic resonance imaging (MRI) [9] for the separation of different tissue types (Gd^{3+}, f^7: high magnetic moment). This procedure provides a valuable diagnosis tool.

The lanthanides are mainly trivalent, sometimes di- or tetravalent. The oxidation state +2 is known for neodymium, samarium, europium, dysprosium, thulium and ytterbium (LnX_2), and the oxidation state +4 for cerium, praseodymium, neodymium, terbium and dysprosium (LnO_2). In aqueous solutions Ce^{4+} is stable, the oxidation states different from +3 are mostly found in the solid state. With increasing atomic number the effective nuclear charge becomes larger and shows strong influence on the 4*f* orbitals which are already in the neutral atom close to the nucleus. The orbitals are contracted further by this effect. An important property of the lanthanides results from this behavior, the so called lanthanides contraction. For the coordination number six the ionic radii $\mathbb{R}$ decrease from La^{3+} (IR = 1.032 Å) to Lu^{3+} (IR = 0.861 Å) [10]. The different size of the ions has an influence on the coordination number and defines the chemistry of the various lanthanids.

The optical spectra (*f-f* transitions) of the lanthanides in their compounds show rather narrow bands compared to d^n ions. Furthermore, their magnetic behavior exhibits significant

[1] Rare-earth compounds: compounds of Y, Sc and La-Lu (for example oxides), lanthanides: lanthanum till luthetium, lanthanoides: elements similar to lanthanum

differences to that of d^n ions. KLEMM described the magnetochemistry of the lanthanides for the first time [11]. He had shown, that it is possible to determine the oxidation states of the lanthanide ion in CeS_2 and CeO_2 by the theory of paramagnetism developed by VAN VLECK [12]. The lanthanide ions show paragmagnetic behavior except for the diamagnetic ions La^{3+}, Ce^{4+}, Yb^{2+} and Lu^{3+}. The reciprocal magnetic susceptibilities of most lanthanide ions follow fairly well the CURIE law, only Sm^{3+} and Eu^{3+}, or more general, f^5 and f^6 ions show large deviations. In case of Eu^{3+} the small splitting due to the spin-orbit-coupling is slightly larger than kT. Thus, according to the Boltzmann distribution the first excited state is populated and contributes to the magnetic moment. The effective Bohr magneton numbers of the rare-earth elements at high temperatures ($T \geq 300$ K) can be calculated using HUND's formula [39]. The temperature dependent magnetic moments are caused by energetically close lying and thus thermally accessible states, that lead to those deviations from the CURIE behavior [13]. The contribution of the temperature dependent paramagnetism (VAN VLECK's paramagnetism) to the magnetic moment is large for these cases.

In this thesis the development of the computer program BonnMag is described. By using BonnMag the excited state energies, magnetic susceptibilities and moments can be calculated for all f^n systems ($1 \leq n \leq 13$) within the framework of *angular overlap model* [24, 60-62]. BonnMag should contain a symmetry analysis of the electronic states (calculation of J projections), assignment of the irreducible representations to the split terms for all thirty two point groups, estimation of the absorption coefficients by using the Judd-Ofelt theory [82-83]. As test for BonnMag compounds containing Nd^{3+} (f^3), Eu^{3+} (f^6), and U^{4+} (f^2) have been investigated. Detailed experimental data on different lanthanide and actinide compounds comprising powder reflectance and single-crystal UV/vis/NIR spectra as well as temperature dependent magnetic moments form the basis for the investigation of the electronic structure of the considered ions. The AOM calculations using BonnMag allow separation of ligand-field effects and spin-orbit coupling on the energy of the observed electronic states. Due to the simple and fast procedure a large number of calculations with variation of parameters is possible. Thus, assessment of the "best fit AOM parameters" as well as the transferability of these parameters is accomplished.

2 Theoretical background

2.1 Ligand-field theory

Ligand field theory [14] represents and extension and refinement of the crystal field theory. The first derivation of the influence of the symmetry and electrostatical crystal field strength on the electronic structure of transition metal ions was given by the crystal field theory of Bethe [15]. This theory considers only the electrostatic interaction of the ligands with the valence electrons of the central ion. In contrast, ligand field theory starts from the unspecified disturbance of the energy levels of the central ion due to the ligands. The precise nature of this interaction is not determined.

The *d* orbitals of free 3*d* transition metal ions are fivefold degenerated. If ligands approach the free ion, they introduce the electrostatic field. Thereby, the energy of the electrons in the orbitals is increased. Because of the anisotropically distributed charge of the ligands the magnitude of repulsion is not the same for all *d* orbitals. Thus, the degeneracy of the five *d* orbitals is lifted.

In a perfect octrahedral ligand field the ligands interact stronger with the $d(x^2-y^2)$ and $d(z^2)$ orbitals (e_g set) than with the d(xy), d(xz), d(yz) orbitals (t_{2g} set). Therefore, the orbitals of the t_{2g} set are less rised in energy than those of the e_g set. In case of *f*-orbitals the splitting in an octahedral ligand field is different from *d*-orbitals. The energies of *d*- and *f*-orbitals in the free ion, in a spherical and a ideal octahedral ligand field are given in Figure 2.1.

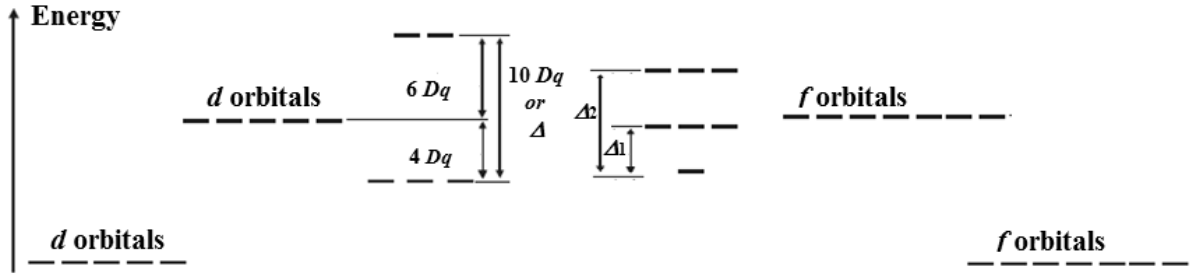

Figure 2.1 Energy levels of the in a free ion , in spherical and octahedral crystal fields for *d*-orbitals (a-c) and *f*-orbitals (d-f).

The energy difference for *d*-orbitals between the t_{2g} and e_g orbitals, the ligand-field splitting, is denoted as Δ or $10Dq$ (unit cm^{-1}) and classified as ligand-field strength parameter. Related to the average energy of the *d* orbitals the t_{2g} set is stabilized by 4 Dq and the e_g set is

destabilized by 6 Dq. This follows from the center-of-mass theorem [14]. The total energy of the five *d* orbitals does not change. The f-orbitals split into three blocks, whereby two ligand-field parameters Δ_1 and Δ_2 are denoted (detailed description in section 2.2).

The magnitude Δ depends on several factors as the type and number of ligands, ionic radius, metal-to-ligand distances and charge of the central atom. The ligands are ordered in the spectrochemical series according to their ability to split the *d* orbitals. This series for the kind of the interaction between selected ligands and metal cations is as follows: $I^- < Br^- < SCN^- < Cl^- < F^- < OH^- < O^{2-} < H_2O < NCS^- < NH_3 << NO_2^- < CN^- < CO$ [16]. Δ amounts to 3000 cm^{-1} to 35000 cm^{-1} for $3d^n$ systems in octahedral coordination spheres.

In a tetrahedral ligand field in case of *d*-orbitals the ligands interact stronger with to d(xy)-, d(xz)-, d(yz)-orbitals of the central atom than with $d(x^2-y^2)$ and $d(z^2)$-orbitals. In contrast to the octahedral coordination the t_{2g}-orbitals are energetically higher then the e_g-set. For the same central atom and ligands the tetrahedral splitting amounts just to 4/9 of the octahedral splitting [17]. For the *f*-orbitals the order of the three sets of orbitals is reverse compared to the octahedral field, the splitting Δ_2 is just 70% (determined using BonnMag) of the octahedral splitting (Fig 2.2).

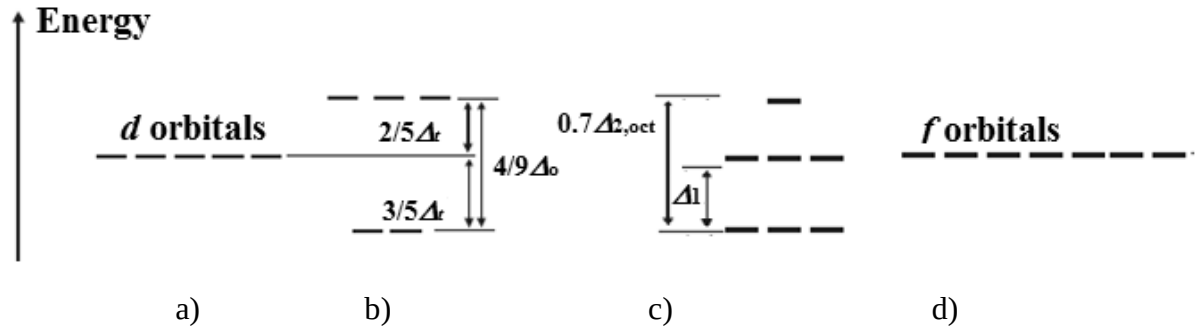

Figure 2.2. Splitting of the *d*- (b) and *f*-orbitals (c) in a tetrahedral ligand-field.

Molecular orbital theory describes the interactions of the ligands´orbitals with the *d*- or *f*-orbitals of the central metal ion. The orbitals of the central atom are combined with those of the ligands [18]. The orbitals are considered to have the proper symmetry for σ-bonding. Each ligand owns a σ-bonding orbital (example sp^n hybrid orbitals). These orbitals build six bonding and two anti-bonding molecular orbitals with the σ-orbitals of the central atom in case of an octahedral complex (Fig. 2.3). Each ligand (Lewis base) provides two electrons that occupy bonding molecular orbitals. The electrons of the central atom (*d* system) are distributed over the energetically unchanged orbitals d(xy), d(xz), d(yz) and σ-antibonding

orbitals d(x^2-y^2) and d(z^2). In case of *f*-orbitals four orbitals are still energetically unchanged and three orbitals are anti-bonding.

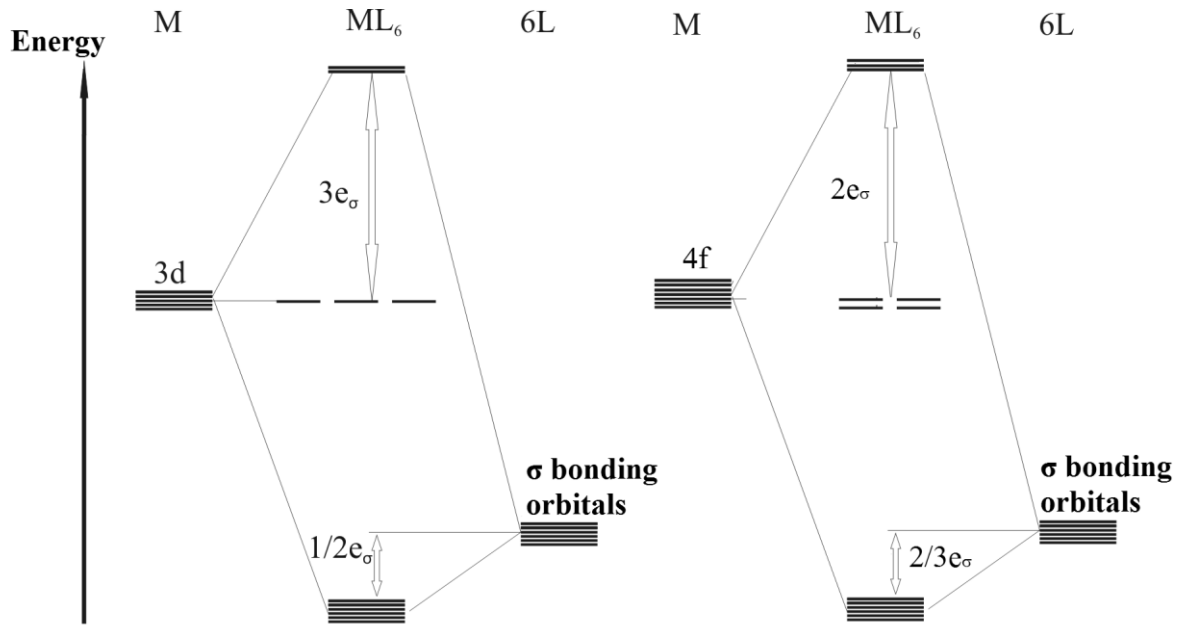

Figure 2.3. Molecular orbitals in the octahedral ML_6 complex taking into account only σ bonding [14]. Atomic orbitals of central atom (a,d), molecular orbitals (b, f), σ-bonding orbitals of ligands (c, e).

The orbitals d_{xy}, d_{xz} and d_{yz} are only capable to form only π bonds with ligands in an octahedral coordination sphere through the interaction with p orbitals of monoatomic ligands or with π molecular orbitals of polyatomic ligands (e.g.: CO, CN^-, PH_3). Two cases are distinguished. In the first case the π orbitals of the ligands are occupied and have lower energy then the metal orbitals (example: OH^-, O^{2-}, F^-). The bonding molecular orbitals are mainly occupied by electrons of the ligands and the antibonding by electrons of the metal. Such ligans are referred as π donators. Due to this bonding situation Δ decreases (Fig. 2.4a). In second case the π bonding orbitals of the ligands are not occupied (example: antibonding orbitals of CN^-, CO) and are therefore energetically higher then the orbitals of the metal. These orbitals are stabilised by π interaction and Δ increases (Fig 2.4a). For the *f*-orbitals the whole splitting for both cases is slightly larger than without π-bonding. The difference is the order of the orbitals (Fig. 2.4b).

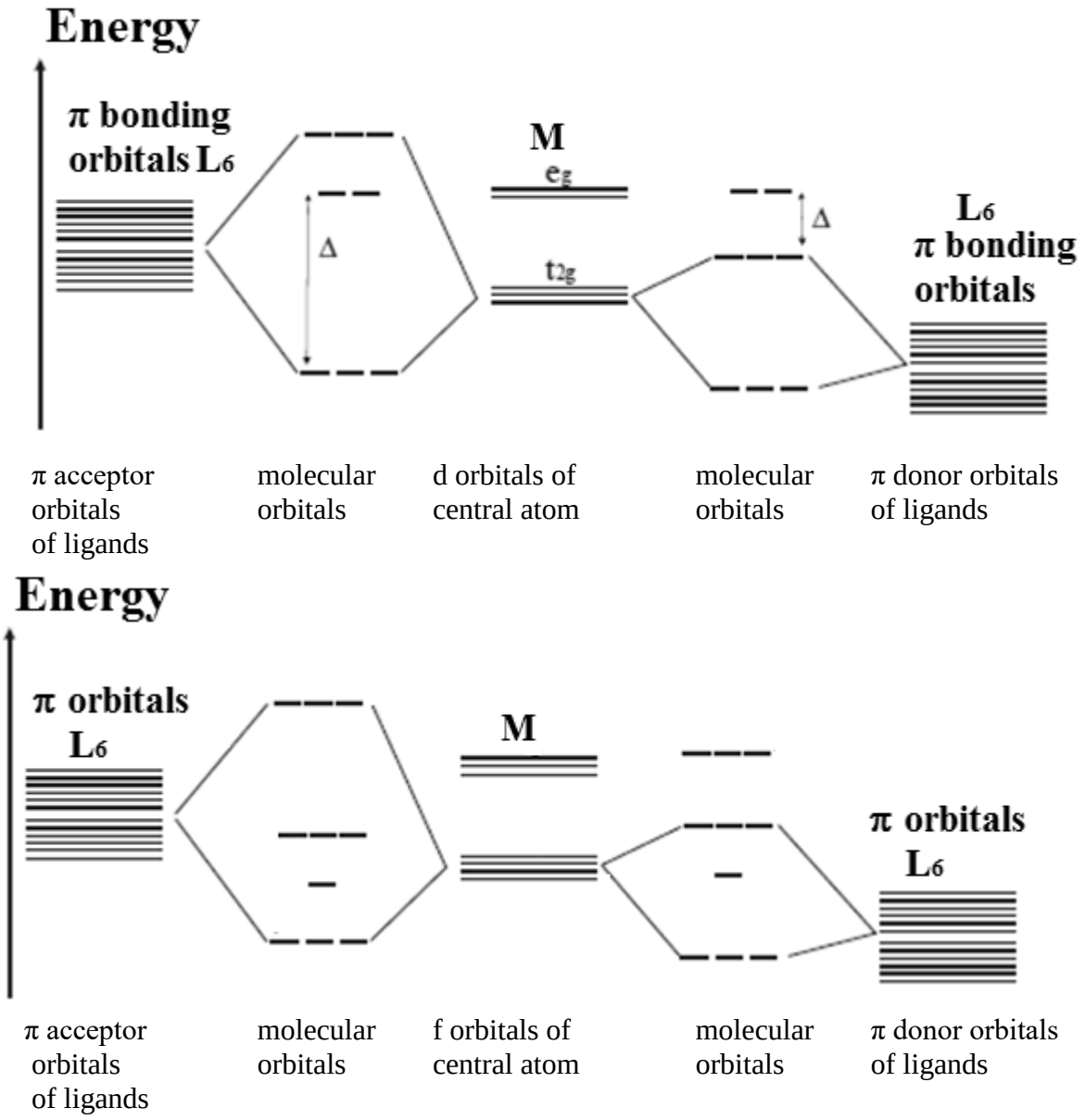

Abbildung 2.4 Splitting diagram of *d*- and *f*- orbitals (top and bottom, respectively) for the interaction with π-donor and π-acceptor ligands in addition to the σ interaction [19].

The *f* orbitals are sevenfold degenerated and can be occupied by a maximum offourteen electrons (principal quantum number $n \geq 4$, orbital quantum number $l = 3$). The seven spherical orbitals are denoted as f_z^3(m = 0), $f_{z(x^2-y^2)}$ (m = -2), f_{xyz} (m = 2), f_{xz}^2 (m = -1), f_{xy}^2 (m = -1), $f_{y(3x^2-y^2)}$ (m = 3) and $f_{x(x^2-3y^2)}$ (m = -3) which are shown in Figure 2.5. Lanthanides and actinides belong to the elements of the *f* group [1]. The lanthanides are found in the oxidation states of +2, +3 und +4 in the solid state. Thereby the electrons are removed from 5*d*- and 6*s*-shells and the 4*f* shell is partially occupied. The energy levels for the transitions within the $4f^n$ shell are approximately until 40000 cm^{-1}. The 4*f* electrons of lanthanide ions undergo only weak interaction with ligands. The overlap of the 4*f* orbitals with orbitals of the ligands is

small. The energy levels rising from the $4f^n$ electron configurations are described by three quantum numbers L (total orbital angular momentumt), S (total spin) und J (total angular momentum). Individual levels of the free ions are assigned in the Dieke-diagram [71]. The splitting of the states by the ligand-field is not included by this diagram. The detailed account on the ligand-field effects are important for the descpriton of chemical bonding between the lanthanides and different ligands. From that reason the ligand field splitting of Pr^{3+} (f^2 system) in different ligand fields was investigated by W. URLAND [20, 21]. He studied $PrCl_3$, as an axample for the nearly octahedral ligand-field, where $[Pr^{III}Cl_6]$ chromophors with the point symmetry C_{3h} are present. The electronic ground state of Pr^{3+} is $^3H_4$ (section 2.4). It splits due to the ligand field into six crystal field levels: E'(Γ_6), A_2"(Γ_4), E'(Γ_6), E"(Γ_5), A_1"(Γ_3), A_1'(Γ_1). The splitting amounts to ~ 100 cm^{-1}.

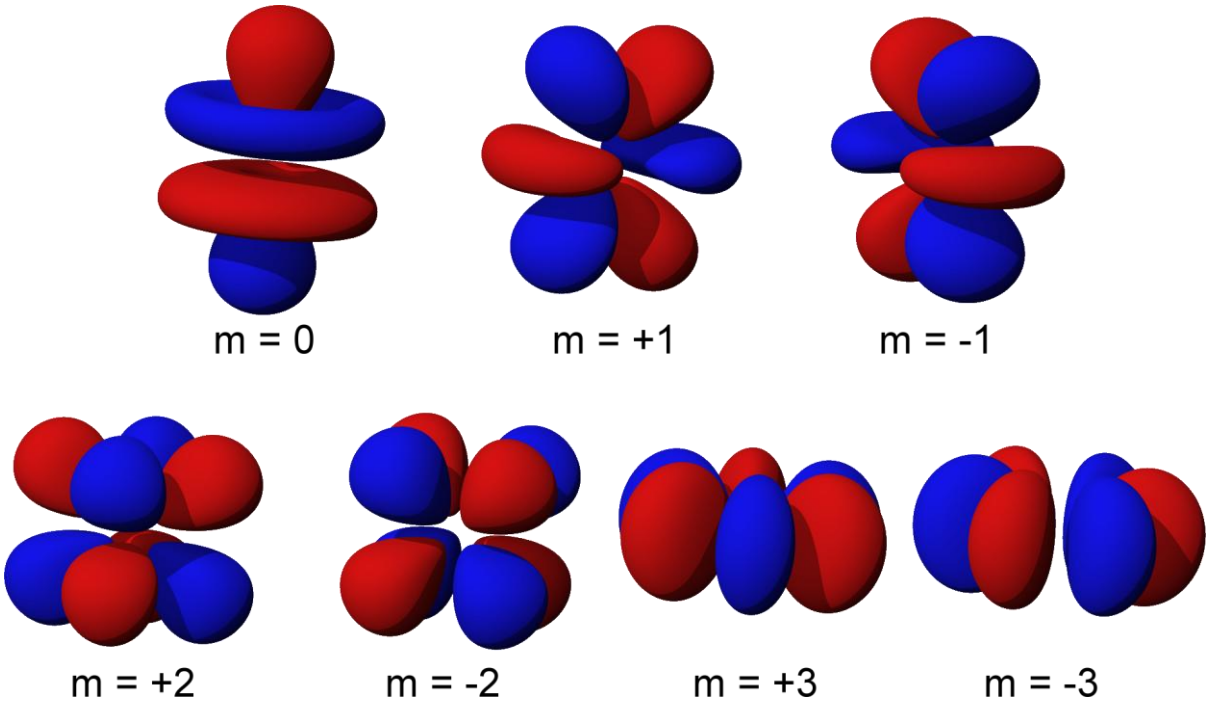

Figure 2.5 Schematic representation of f orbitals with n = 4, l = 3 and different magnetic quantum number m [22]. f_z^3(m = 0), $f_{z(x^2-y^2)}$ (m = -2), f_{xyz} (m = 2), f_{xz}^2 (m = -1), f_{xy}^2 (m = -1), $f_{y(3x^2-y^2)}$ (m = 3) and $f_{x(x^2-3y^2)}$ (m = -3).

2.2 Angular Overlap Model

Already in the 1960s and 1970s the angular overlap model (AOM) was used for calculation of the optical and magnetic properties based on the energies of the f electronic states of rare earth metal compounds (later also for transition metal compounds) [23, 24, 25].

In the AOM the ligand field, which ist given by 10Dq or Δ (for d^n systems), is decomposed into the contributions of individual metal-ligand interactions. Chromophores with different

geometric structures can be discriminated by this model. The splittings Δ_o und Δ_t are the result from σ-, π- and δ- interactions between the ligands and the central atom. The interaction energies are described by empirical parameters e_σ, e_π and e_δ. For the consideration of novel systems these parameters can be transferred from already parameterized compounds or can be optimized for each compound separately. The transfer of parameters is preferable since it allows the modeling of a large number of new phases. For homoleptic, octahedral complexes containing d^n ions the link between Δ_o, e_σ and e_π is given by Eq. 2.1.

$$\Delta_0 = 3e_\sigma - 4e_\pi \qquad \text{Equation 2.1}$$

The term $3e_\sigma$ corresponds to the increase of the energy of e_g orbitals by the summation of the σ-interactions of these orbitals with the σ-bonding orbitals of the six ligands. If these six ligands are oxygen atoms, which show ligator behavior, the π interaction between the ligand orbitals with π-symmetry and the t_{2g} orbitals of the metal leads to destabilization of t_{2g} set of $4e_\pi$ (Fig 2.6).

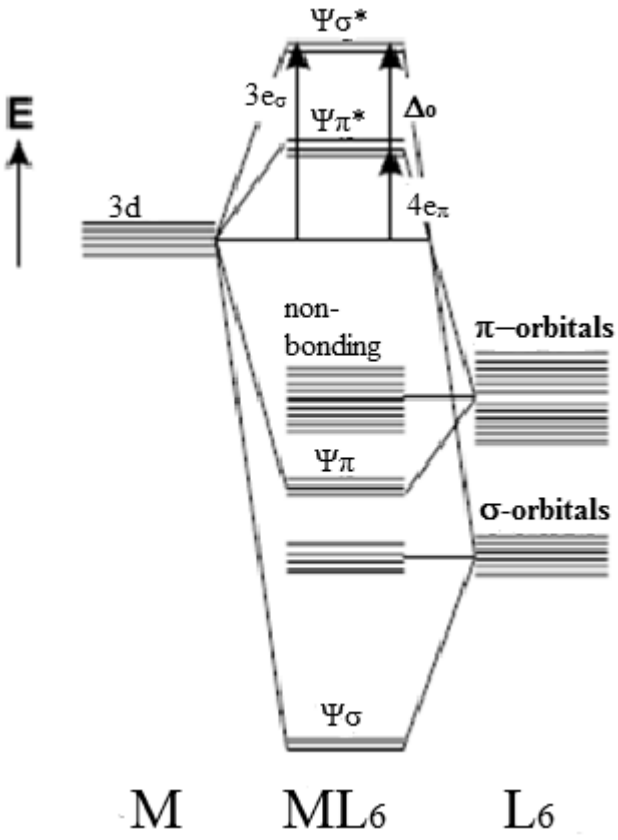

Figure 2.6. σ- and π-interactions between the d-orbitals of the central atom *M* and six ligands [26].

For the f^n systems the relations become more complicated. Thus, for an octahedral chromophore two parameters are needed to describe the ligand-field for a f^n system (Eq 2.2) . The f-orbitals split into the three sets a_{2u}, t_{2u}, and t_{1u} (Figure 2.7).

$\Delta_1 = 5e_\pi/2$ and $\Delta_2 = 2\ e_\sigma + 3e_\pi/2$ (2.2)

with the approximation $e_\pi = 1/4\ e_\sigma$ follows for $\Delta_1 = 5e_\sigma/8$ and $\Delta_2 = 2\ e_\sigma + 3e_\pi/2 = 19e_\sigma/8$

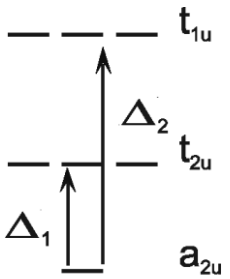

Figure 2.7. Splitting of *f*-orbitals under an octahedral ligand field. a_{2u}: f_{xyz}; t_{2u}: $f_{z(x^2-y^2)}$ and linear combination of f_{xz}^2, f_{xy}^2, $f_{y(3x^2-y^2)}$ and $f_{x(x^2-3y^2)}$; t_{1u}: f_z^3 and linear combination of f_{xz}^2, f_{xy}^2, $f_{y(3x^2-y^2)}$ and $f_{x(x^2-3y^2)}$.

The magnitude of the interaction energies decreases in the order $e_\sigma > e_\pi > e_\delta$. These interaction parameters are proportional to the overlap integral between the respective orbitals of the central atom and the ligand orbitals and attain specific values for each kombination of central atom M^{n+} and ligand L depending on the distance d(M-L). The energy contribution can be split into an angular part and radial part (Eq. 2.3).

$$S_{ab} = S_\lambda \cdot \theta_{ab}$$ Equation 2.3

S_{ab} overlap integral

S_λ radial part ($\lambda = \sigma, \pi, \delta$)

θ_{ab} angular part of the interactions

Since the overlap integrals depend on spatial arrangement of the ligands around the central atom, the geometric structure of the polyhedra influences the energy levels of the central atom [26].The σ- or π-interaction for some mutual alignments of orbitals of the central atom *M* and the ligand L are shown in Figure 2. The angle φ determines the magnitude of the angular part of the overlap integral which attains values from 0 (φ = 90°) to 1 (φ = 0°) for the σ-interaction between $f(z^3)$ and p_z orbital. For the π-interaction between p_x and $f(z(x^2-y^2))$ orbital the angular parts of the overlap integrals vary from -1 (φ = 90°) to 1 (0°). In case of φ = 54.73° the bonding and anti-bonding interactions for π bonding cancel each other. The general setting of f-orbitals (f_z^3, $f_{z(x^2-y^2)}$, f_{xyz}, f_{xz}^2, f_{xy}^2, $4f_{y(3x^2-y^2)}$ and $4f_{x(x^2-3y^2)}$) as given in Ref. 27 are used.

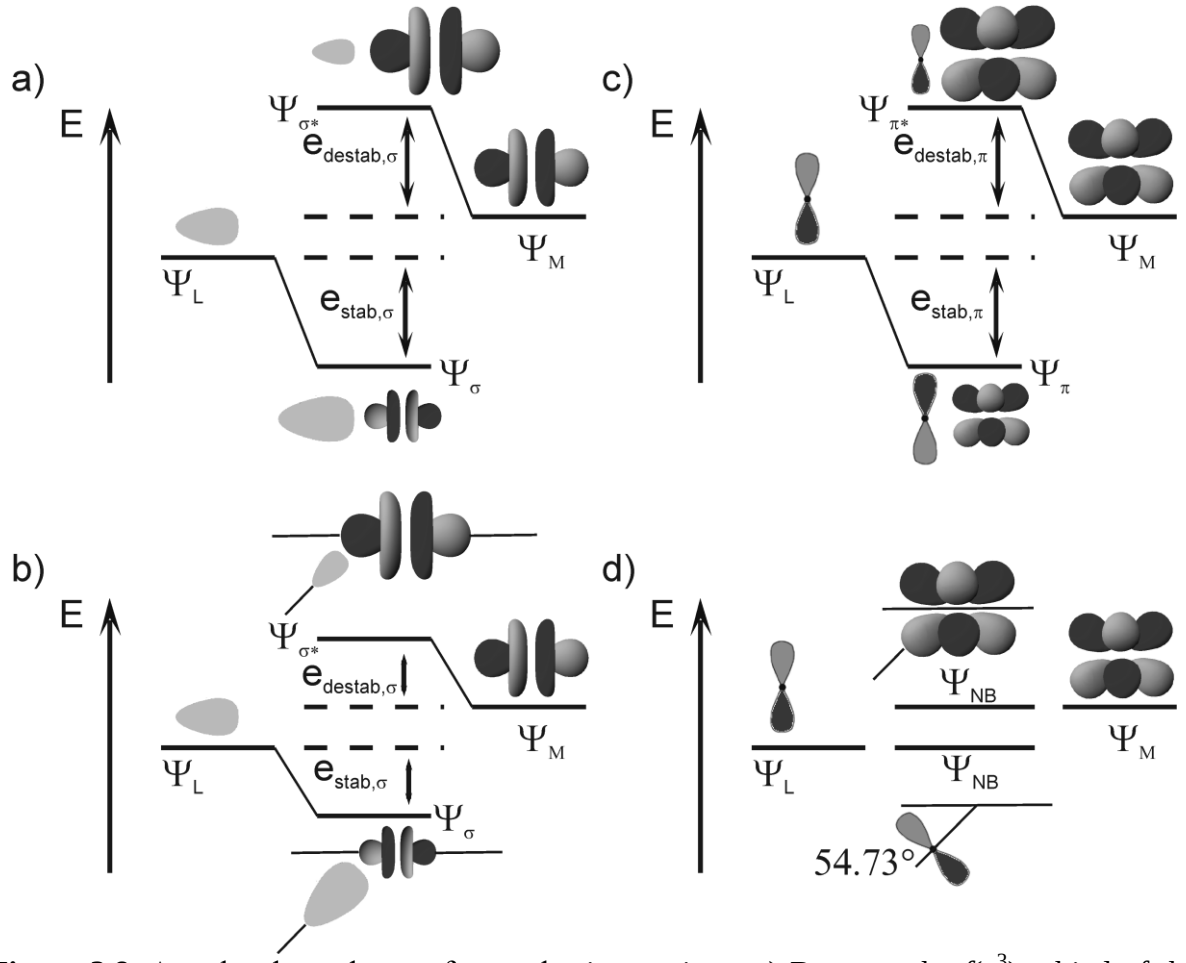

Figure 2.8. Angular dependence of σ- and π-interactions. a) Between the $f(z^3)$ orbital of the metal and a σ-orbital of a ligand (φ = 0°), b) between the $f(z^3)$ orbital of the metal and a σ-orbital of a ligand (φ), c) between the $f(z(x^2\text{-}y^2))$ orbital of the metal and a p-orbital of a ligands (φ = 0°), d) between the $f(z(x^2\text{-}y^2))$ orbitals of the metal and a p-orbital of a ligand (φ = 54.73°). Figure adapted from literature. [28].

2.3 AOM parameters

For the calculation of the UV/vis spectra and magnetic properties of compounds containing an open f-shell within the AOM parametrization schemethe interaction energies e_σ and e_π for all *M-L* interactions, Condon-Shortley parameters F_2, F_4, F_6, spin orbit coupling constant ζ and Stevens orbital reduction factor k [29] are used.

The AOM model assumes a weak interaction between ligands and central atom. As a consequence the energy states of a cation in a specific coordination are obtained as a pertubation of the states of the free gaseous ion. The pertubation is derived from the bonding properties of the ligands. The differences between the ground state and the excited electronic states of the free ions are experimentally accsessible and are approximated by Condon-Shortley theory with parameters F_2, F_4 and F_6 [30]. These parameters are calculated from F^2, F^4 and F^6 via equations 2.4a-c [31].

$F^2 = 225F_2$ Equation 2.4a

$F^4 = 1089F_4$ Equation 2.4b

$F^6 = 184041F_6/25$ Equation 2.4c

The Slater-Condon-Shortley parameters for an atom in a complex are smaller then the values of the free ions. For transition metal complexes the reduced values are in the range of 80% of the free ion values. This decrease of the parameters is denoted as nephelauxetic effect. The nephelauxetic ratio β describes the ratio B(ion in complex) / B(free ion). The nephelauxetic effect is quite small for f^n systems. The electron density is partially transferred from the metal ion to the ligands, so that the electron-electron interaction at the metal ion is reduced. The spin orbit coupling constant ζ undergoes a similar reduction in comparison to the free ion values. For the calculation of the UV/vis spectra of transition metal complexes ζ has a minor importance because the vibronic broadening of the bands is very large. The influence of the spin-orbit coupling is small compared to the ligand-field effect, so that the coupling is hardly observed in the UV/vis spectra. In contrast, for the energies of *f* electron systems accounting for spin-orbit coupling is very important (section 2.4).

For the parametrization of the AOM with respect to measured spectra the interaction energies e_σ and e_π are needed besides the interelectronic repulsion parameters F_2, F_4, F_6. For a low-symmetric complex the three interaction parameters e_σ, $e_{\pi,x}$ and $e_{\pi,y}$ have to be determined for each ligand. A large numer of parameters follows as a result. Based on additional information the number of independent parameters is reduced. In the early 1960s the pressure dependence of ligand-field splitting was investigated [32, 33] and a relation between Δ and the metal-to-ligand distance was found. It could be expressed by $\Delta \sim d(M\text{-}L)^{-n}$ with $4 \leq n \leq 7$. Therefore the relation $e_\sigma \sim d(\text{M-L})^{-n}$ is often used in AOM. In complexes with several identical ligands at different distances all e_σ are related to the value $e_{\sigma,max}$ for $d(\text{M-L})_{min}$.

The values β, ζ and the interaction parameters e_σ and e_π show for 3*d*, 4*d*, 5*d* and 4*f* systems large differences. The spin orbit coupling constant ζ increases strongly from 3*d* to 4*f* and has to be accounted for in case of 4*f* systems. For 5*d* elements it is possible to use the total angular momentum quantum number *J* as well as orbital angular momentum quantum number *L* together with total spin quantum number *S*. The nephelauxetic ratio β is smaller for 4*f* elements then for 3*d*, because the overlap of *f* orbitals with ligand orbitals is smaller. Similarly the e_σ values are smaller for lanthanide complexes compared to the transition metals. Currently, e_π for *Ln-L* interactions is accepted to be isotropic. Thus, $e_{\pi,x}$ and $e_{\pi,y}$ can be replaced by an isotropic π interaction $e_{\pi,iso}$ between the metal and the ligand. As a further

approximation the ratio e_π/e_σ can be assumed between 1/4 and 1/3. Therefore the number of independent parameters for octahedral complexes can often be reduced to just one, $e_{\sigma,max}$. However, this consideration is valid only in the case of an isotropic π-interaction between metal and ligand. This simple bonding situation might be assumed if, for example, all oxygen atoms in a [MO_n] polyhedron have a coordination number of two. In this case the σ-interaction between the metal atom and the ligand might be assumed through a sp-orbital and the two remaining p-orbitals at oxygen atoms form an isotropic π-interaction. If the coordination number of oxygen is larger than two consideration of different π-interactions is needed [34]. Further reasons for the π-anisotropy are reported by REINEN [34].

For the parametrization of f^n systems different schemes can be used. Besides the AOM approach the so-called WYBORNE parametrization exist [35], which however do not provide any chemical information, different from the AOM. Global parametrization according to Wybourne include two parameters similar to Δo and Δt, whereby AOM decomposes the ligand-field into the contributions of the individual metal-ligand interactions.

2.4 Magnetic measurements

The electrons in molecular orbitals have a magnetic orbital momentum due to their angular momentum. The magnetic spin momentum of an electron follows from the intrinsic rotation. For electron pairs the magnetic spin moments are of equal or opposite sign (spin pairing). If the electrons are brought into an external magnetic field, the external field induces an additional current, which in turn generates a magnetic field. The induced magnetic field is opposite to the external field (LENZ rule). As a result the magnetic field (B = magnetic flux density) in the sample is smaller than the external field ($B_{in} < B_{ext}$), so the sample becomes repulsive. This phenomenon is called diamagnetism. If B_{in} is larger then B_{ext}, the system is paramagnetic (Equations 2.5) While paramagnetism is due to the presence of unpaired electrons, all electrons contribute to the diamagnetism.

$$B_{in} = B_{ext} + B' \qquad \text{Equation 2.5}$$

The magnetic field B_{in} is expressed in terms of the magnetic susceptibility (Eq. 2.6), which is defined as the ratio ob B' and B_{ext}, $\chi_v = B'/B_{ext}$.

$$B_{in} = (1 + \chi_v)B_{ext} \qquad \text{Equation 2.6}$$

The volume susceptibility normalizes χ_v to molar volume.

$\chi_{mol} = \chi_v \cdot V_{mol}$ ($cm^3 \cdot mol^{-1}$)

The total magnetic molar susceptibility χ_{mol} of a compound is the sum over all diamagnetic and paramagnetic contributions of all electrons (Equation 2.7).

$$\chi_{mol} = \chi_{mol}^{dia} + \chi_{mol}^{para} \qquad \text{Equation 2.7}$$

The diamagnetic part can be determined using the LANGEVIN formula.

$$\chi_{mol}^{dia} = -\frac{e^2 \cdot N_A}{6 \cdot m_e} \sum_{i=1}^{n} \overline{R_i}^2 \qquad \text{Equation 2.8}$$

e elementary charge ($1.602 \cdot 10^{-19}$ C)

N_A Avogadro number ($6.02 \cdot 10^{23}$ mol^{-1})

m_e mass of an electron ($9.109 \cdot 10^{-31}$ kg)

n number of electrons

R_i mean distance between electrons and core (cm)

A correction of the measured values taking into account the diamagnetic moment and the used sample tube leads to the paramagnetic part of the susceptibility. Measurements are performed at different temperatures. Using the CURIE-WEISS law the magnetic moment μ_{exp} can be obtained from the slope $1/\chi_{mol}$ (T), and the paramagnetic WEISS temperature Θ_p from the x-intercept. This law assumes a constant magnetic moment in the whole temperature range. The CURIE-WEISS law predicts a linear behavior ($\chi_{mol} = C/T$) with $1/\chi_{mol} = 0$ for T = 0 for compounds with isolated paramagnetic ions. The WEISS temperature represents the shift of the zero point of $1/\chi_{mol}$ due to the mutual interaction between the spin centers. The WEISS temperature is a therefore measure of the deviation from pure paramagnetic behavior. A negative Θ_p indicates an antiferromagnetic interaction (example: NiO, MnO, CoO), because antiparallel spins lead to a decrease of the susceptibilities (and therefore to an increase for $1/\chi_{mol}$), positive Θ_p indicates ferromagnetic behavior (Co, Ni, Fe, CrO_2). For an understanding of the magnetic behavior it is important to know, how the magnetic interactions are achieved. It has been found [36] that direct coupling between paramagnetic metal ions is relevant for distances below 2.9 Å. An indirect interaction is possible over a common ligand, the so called "super exchange". Super exchange requires the suitable arrangement of the orbitals of

participating atoms to each other. The bonding angle is therefore important for the strength of the interaction [37].

$$\frac{1}{\chi_{mol}} = \frac{(T-\Theta)}{C} = \frac{1}{C}T - \frac{1}{C}\Theta = mT + b \qquad \text{Equation 2.9}$$

χ_{mol} molar susceptibility ($cm^3 \cdot g^{-1}$)
T absolute temperature (K)
Θ Curie temperature (K)
C Curie constant ($K \cdot mol \cdot cm^{-3}$)
m slope of line of best fit
b y-intercept of line of best fit

$$\mu_{exp} = \sqrt{\frac{3 \cdot R}{n \cdot m \cdot N_A^2} \cdot \mu_B} \qquad \text{Equation 2.10}$$

μ_{exp} experimental magnetic moment ($erg \cdot Oe^{-1}$)
μ_B Bohr magneton ($9.27 \cdot 10^7$ $erg \cdot Oe^{-1}$)
R ideal gas constant ($8.31441 \cdot 10^7$ $erg \cdot K^{-1} \cdot mol^{-1}$)
n number of unpaired electrons
m slope of line of best fit (from $1/\chi_{mol}$ vs. T)
N_A Avogadro constant ($6.022 \cdot 10^{23}$ mol^{-1})

Equation 2.10 allows calculation of the average value of the magnetic moment, if several magnetic centers are contained in the compound. The theoretical calculation of the magnetic moment of d^n ions can be done applying equation 2.11, if only the spin of the electrons („spin-only“) has to be considered, which means that the contributions from the orbital momentum can be neglected.

$$\mu_{th} = g \cdot \sqrt{S \cdot (S+1) \cdot \mu_B} \qquad \text{Equation 2.11}$$

μ_{th} theoretical magnetic moment with spin-only behavior ($erg \cdot Oe^{-1}$)
μ_B Bohr magneton ($9.27 \cdot 10^7$ $erg \cdot Oe^{-1}$)
S total spin quantum number of the atom
g Landé factor

In a paramagnetic solid the degenerancy of the energy levels is removed by the internal magnetic field. Due to the occupation of the low-lying energy levels the solid is stabilized. The effect becomes more pronouncal due to the increase of the applied magnetic field and the splitting of the energy levels. If a single molecule is considered, the microscopic magnetization can be defined as well as the macroscopic magnetization

$$\mu_n = \frac{\partial E_n}{\partial H} \qquad \text{Equation 2.12}$$

The macroscopic or molar magnetization is obtained by a weighted sum up of μ_n according to Boltzmann law.

$$M = \frac{N_A \sum_n (-\frac{\partial E_n}{\partial H}) e^{(-\frac{E_n}{kT})}}{\sum_n e^{(-\frac{E_n}{kT})}} \qquad \text{Equation 2.13}$$

In order to calculate the molar magnetization, the energy levels have to be determined dependent on a magnetic field for an atom. For this purpose the simplification introduced by J. H. VAN VLECK is used, which contains several assumptions: the paramagnetic susceptibility does not depend on the field, the energy of the ith level can be expressed as series and h/kT is smaller then 1 [30].

$$E_n = E_n^{(0)} + E_n^{(1)} H + E_n^{(2)} H^2 + \ldots \qquad \text{Equation 2.14}$$

It follows

$$e^{(-\frac{E_n}{kT})} = \left[e^{(-\frac{E_n^{(0)}}{kT})} \right] [1 - E_n^{(1)} \frac{H}{kT}] \qquad \text{Equation 2.15}$$

$E_n^{(0)}$ is the energy in the absence of a magnetic field and $E_n^{(1)}$ and $E_n^{(2)}$ are the Zeeman coefficients of the first and second order, respectively. The microscopic magnetization is

$$\mu_n = \frac{\partial E_n}{\partial H} = -E_n^{(1)} - 2E_n^{(2)} H - \ldots \qquad \text{Equation 2.16}$$

The following is obtained using the last two assumptions in equation 2.13

$$M = \frac{N_A \sum_n (-E_n^{(1)} - 2E_n^{(2)} H)(1 - \frac{E_n^{(1)} H}{kT}) e^{(-\frac{E_n^{(0)}}{kT})}}{\sum_n (1 - \frac{E_n^{(1)} H}{kT}) e^{(-\frac{E_n^{(0)}}{kT})}}$$ Equation 2.17

If the external magnetic field is zero, the magnetization disappears, so that equation 2.20 follows. This has direct consequences for the accomplishment of magnetic measurements. In general they are performed under so called Zero Field Cooling (ZFC) condition. The sample is cooled below 10 K without application of a magnetic field. At this temperatures small magnetic fields are activated and the magnetic moment is measured with increasing temperature [38].

$$\sum_n E_n^{(1)} e^{(-\frac{E_n^{(0)}}{kT})} = 0$$ Equation 2.18

This condition excludes compounds, which have a spontaneous magnetization. The above equation 2.18 is simplified and the VAN VLECK equation 2.19 is obtained, that shows the relation between the magnetic susceptibility and thermally populated electronic energy states [39].

$$\chi = \frac{N_A \sum_n (\frac{(E_n^{(1)})^2}{kT} - 2E_n^{(2)}) e^{(-\frac{E_n^{(0)}}{kT})}}{\sum_n e^{(-\frac{E_n^{(0)}}{kT})}}$$ Equation 2.19

2.5 Magnetic behavior and ligand-field splitting

Investigations of magnetic properties are especially provide valuable infomation on the electronic ground state of transition and rare earth metals. For example the measurement of magnetic susceptibilities provides distinction between low- and high spin configuration. In case of transition metals the investigated compounds could be the high-spin or low-spin complexes depending on the ligand field. The magnetic ground state is a result of the spin pairing energy on the one hand and ligand field stabilization energy on the other.

The spin-only approximation is valid only for transition metals. It results from the simplification of the VAN VLECK formula by neglecting the orbital momentum [14, 39]. In case of $3d^1$ - $3d^4$ systems pure spin magnetism is approximately observed due to the small contribution of the orbital momentum. The values for the magnetic moment are in general

only slightly smaller than the calculated spin-only values. For $3d^6$ - $3d^9$ the orbital momentum is larger than for $3d^1$ - $3d^4$ systems and is summed with the spin momentan. Thus, the experimental magnetic moment is for most cases larger than the spin-only value. This effect is explained by increasing spin-orbit interaction along the 3*d* row. For Co^{2+} compounds a large range for the magnetic moment is found (4,3-5,2 μ_B). The ligand field symmetry (octahedral or tetrahedral) has a large influence. In case of 4*d* and 5*d* metals diamagnetic behavior and low-spin configurations occur more often than for 3*d* metals. Since the ligands are stronger attracted by the higher nuclear charge, the 4*d* and 5*d* orbitals show larger splitting. the interelectronic repulsion in 4*d* and 5*d* orbitals decreases due to larger expansion, whereby it counteracts the spin pairing [39]. For rare-earth metals the orbital momentum has to be taken into account for the calculations of magnetic moments, because spin-orbit coupling of *f*-electron configurations is larger compared to most transition metals. For the calculation of the magnetic moment the total angular momentum has to be used instead of the spin-only approximation (Equation 2.20).

$$\mu_{th} = g \cdot \sqrt{J \cdot (J+1) \cdot \mu_B} \qquad \text{Equation 2.20}$$

J total angular momentum quantum number, $J = L+S$.

The Landé factor can be calculated by the HUNDS formula (Equation 2.21) [39].

$$g = 1 + \frac{S(S+1) - L(L+1) + J(J+1)}{2J(J+1)} \qquad \text{Equation 2.21}$$

L orbit angular momentum quantum number

The measured magnetic moments μ_{exp} of f^n systems result from the theoretical values μ_{th} of the different populated states (Boltzman distribution). In some cases (f^5 and f^6 systems) they show large deviations from the CURIE behavior.

The splitting of the electronicground state is caused by the ligand field and spin orbit coupling. Those resulting states are occupied as given by the Boltzmann distribution. As a result a non-linear behavior is observed for the reciprocal molar susceptibility against temperature [40].

As an example, Pr^{3+}, which has two *f* electrons, is considered here. Due to the occupation of two *f* orbitals according to Hunds rules the orbit angular momentum quantum number $L = 5$ and the total spin S is one. Therefore $M = 2S+1 = 3$. The configuration term symbol (Mulliken-Plazek [41, 42, 43]) for the ground state is ^3H. Due to spin-orbit coupling the ground state leads to several states: $^3H_4$, $^3H_5$, and $^3H_6$ (^ML_J) with $J = [L\text{-}S,..., L+S, \Delta J = 1]$. In

the octahedral ligand field of the chromophore [$Pr^{III}F_6$], e. g. in Cs_2KPrF_6 [44], the ground state $^3H_4$ splits into: A_{1g} (Γ_1), T_{1g} (Γ_4), E_g (Γ_3) and T_{2g} (Γ_5).

At high temperatures (T ≥ 298 K) a constant magnetic moment can be approximately expected for most f^n ions. The experimentally observed magnetic moments correspond well to those calculated with HUND's formula except for Eu^{3+} and Sm^{3+} (f^5 and f^6 systems) (Table 2.1). Eu^{3+} is an f^6 ion with the ground state $^7F_0$. Here "unmagnetic" behavior is expected despite six unpaired electrons due to the compensation of spin and orbital moment (S = 3 and L = 3 lead to J_{min} = 0). The first excited states is populated due to the small spin-orbit coupling, whereby the splitting $^7F_0 \rightarrow {}^7F_1$ ~ 350 cm^{-1}, which is only slightly larger than kT (200 cm^{-1}). The observed magnetic moment is a result of the Boltzmann population of excited states [45]. For Sm^{3+} a significant deviation between the calculated and experimental magnetic moment is found similar to Eu^{3+} (Table 2.1, highlighted in grey).

Table 2.1. Magnetic moments of Ln^{3+} ions [39].

Ion	Electronic configuration of ground state	Term symbol[a)]	Magnetic moment	
			Calculated[a)]	experimental
La^{3+}	[Xe]$4f^0$	$^1S_0$	0	0
Ce^{3+}	[Xe]$4f^1$	$^2F_{5/2}$	2.54	2.3-2.5
Pr^{3+}	[Xe]$4f^2$	$^3H_4$	3.58	3.4-3.6
Nd^{3+}	[Xe]$4f^3$	$^4I_{9/2}$	3.62	3.5-3.6
Pm^{3+}	[Xe]$4f^4$	$^5I_4$	2.68	2.7
Sm^{3+}	[Xe]$4f^5$	$^6H_{5/2}$	0.84	1.5-1.6
Eu^{3+}	[Xe]$4f^6$	$^7F_0$	0	3.4-3.6
Gd^{3+}	[Xe]$4f^7$	$^8S_{7/2}$	7.94	7.8-8.0
Tb^{3+}	[Xe]$4f^8$	$^7F_6$	9.72	9.4-9.6
Dy^{3+}	[Xe]$4f^9$	$^6H_{15/2}$	10.63	10.4-10.5
Ho^{3+}	[Xe]$4f^{10}$	$^5I_8$	10.60	10.3-10.5
Er^{3+}	[Xe]$4f^{11}$	$^4I_{15/2}$	9.58	9.4-9.6
Tm^{3+}	[Xe]$4f^{12}$	$^3H_6$	7.56	7.1-7.4
Yb^{3+}	[Xe]$4f^{13}$	$^2F_{7/2}$	4.54	4.4-4.9
Lu^{3+}	[Xe]$4f^{14}$	$^1S_0$	0	0

a) The ground state for $1 \leq n \leq 6$ is $^{2S+1}L_J$ ($J = L\text{-}S$) and for $8 \leq n \leq 13$ is $^{2S+1}L_J$ ($J = L\text{+}S$)

b) $\mu_{th} = g \cdot \sqrt{J \cdot (J+1) \cdot \mu_B}$ with $g = 1 + \frac{S(S+1) - L(L+1) + J(J+1)}{2J(J+1)}$

2.6 Comparison between transition metals and lanthanides

As already mentioned in section 2.3, pronounced differences exist between the electronic states of transition metals and rare earth metals. In Figures 2.9 and 2.10 two UV/vis spectra

are compared. ErZnPO [46] is an example of a rare earth element compound and α-$CrPO_4$ [47] as a compound with a transition metal cation. Table 2.2 shows the comparison of different charasteristic values needed for description of the free ion energies and ligand-field splitting for a transition metal and lanthanide ion.

Table 2.2. Comparison between Δ_o, F_2 (Er^{3+}) or B(Cr^{3+}), ζ and β for Cr^{3+} and Er^{3+}.

	Cr^{3+}	Er^{3+}
Ligand-field splitting Δ_o	~10000 cm^{-1}	~100 cm^{-1}
B / F_2	~1000 cm^{-1}	~450 cm^{-1}
ζ	~100 cm^{-1}	~3000 cm^{-1}
β	0.7-0.9	0.95-1.0

In the spectrum of ErZnPO a series of sharp transitions is visible. The optical excitations occur from the ground state $^4I_{15/2}$ into different excited states, that can be matched with the DIEKE diagram [71] (Figure 2.9). The single bands are split by the ligand field. This is visible for all observed transitions. In comparison in α-$CrPO_4$ the excitation occurs from the ground state $^4A_{2g}$(F) into different quartet states, $^4T_{2g}$(F), $^4T_{1g}$(F) and $^4T_{1g}$(P) (this is above 30000 cm^{-1} and can not be measured). In the spectra some duplet states are observed, too (comp. Figure 2.10). The assignment of each state is possible using TANABE-SUGANO diagrams [48].
Comparison of both UV/vis spectra shows, that bands in the spectrum of α-$CrPO_4$ are much wider then in the spectrum of the erbium compound. For ErZnPO rather sharp and narrow peaks are visible. For transition metal complexes a considerably larger ligand field splitting is observed compared to the rare earth metal compounds. It is in the range of several thousand wavenumbers for transition metals and only some hundreds for rare earth ions. Small ligand-field splitting is only visible in high-resolved spectra.
The effect of "vibronic" broadening of bands, that occurs in the spectra of transition metal complexes, obscurs the splitting due to spin-orbit coupling which is in the range of 100 cm^{-1}. The broadening caused by the strong interaction between *d* orbitals with the ligand orbitals. *f* orbitals are better shielded and therefore undergo no vibronic overlap. For rare-earth metal complexes the influence of spin-orbit coupling is clearly visible due to the missing broadening of the bands, spin-orbit coupling for these elements is in the range of ~5000 cm^{-1}. In contrast to the spectra of 3*d* metal ions the consideration of spin-orbit coupling is absolutely necessary for the modelling of the spectra of f^n systems.

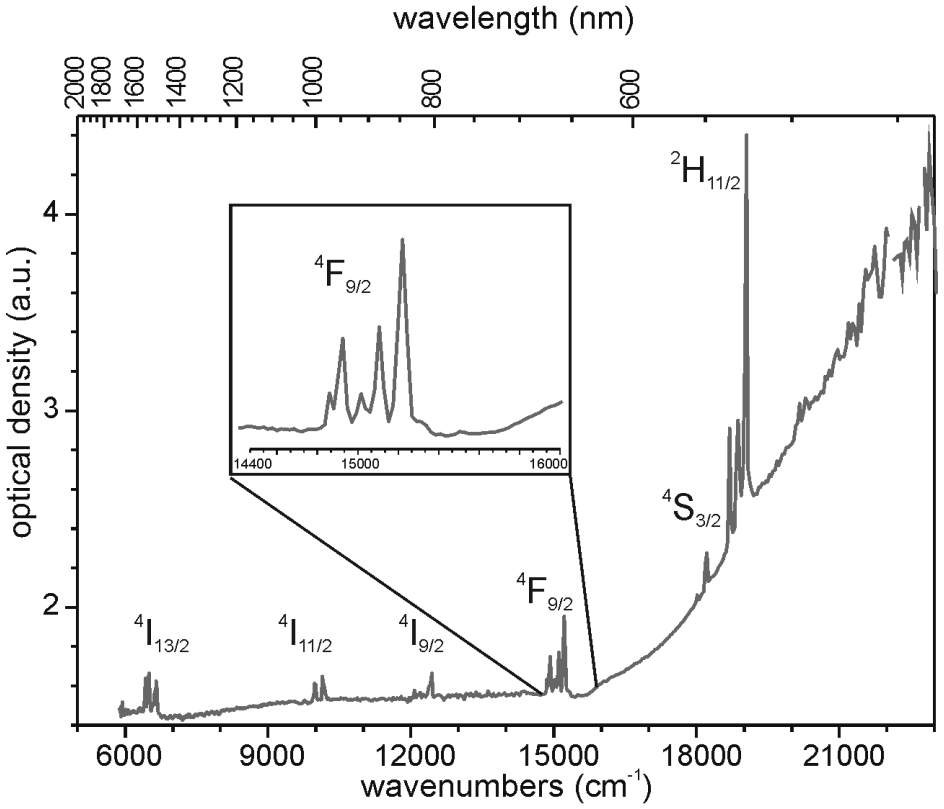

Figure 2.9 Single crystal UV/vis/NIR spectrum of ErZnPO at room temperature. Polarization perpendicular to *c*-axis [49].

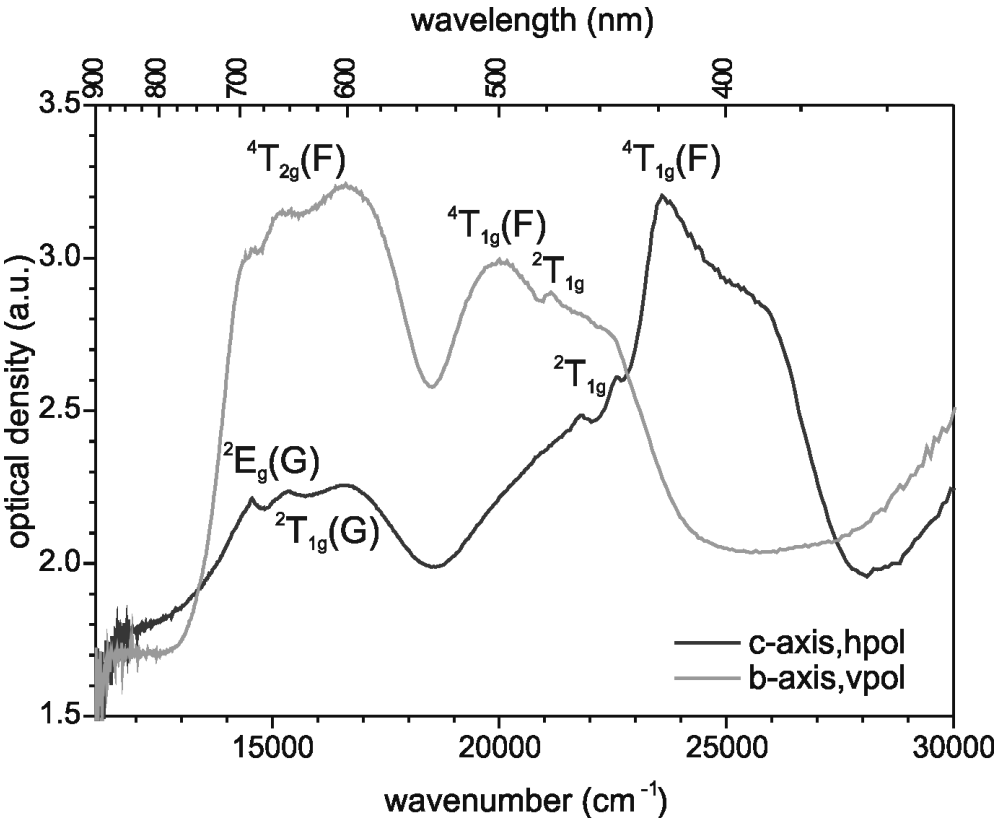

Figure 2.10 Polarized UV/vis/NIR spectra of α-$CrPO_4$ at room temperature [50].

2.7 The g-tensor of Ln^{3+} ions [40]

The electronic Zeeman interaction can be be given by the following term in the Hamiltonian (equation 2.22),

$$\mathcal{H} = \beta \cdot H \cdot g \cdot S \qquad \text{Equation 2.22}$$

where *g* is a 3x3 tensor, if only the angular momentum is considered, the *g*-tensor is isotropic and has diagonal elements of g_e = 2.0023. If the *g*-tensor is anisotropic *S* does not represent the true spin, so that it should be distinguished from the real spin (capped *S*, equation 2.23).

$$\mathcal{H} = \beta \cdot H \cdot g \cdot \hat{S} \qquad \text{Equation 2.23}$$

Due to the interaction of *H* with the angular momentum *L* the full Hamiltonian has to be extended

$$\mathcal{H} = \beta \cdot H \cdot L + \beta \cdot H \cdot g_e \cdot \hat{S} \qquad \text{Equation 2.24}$$

The perturbing Hamiltonian is denoted as "effective spin Hamiltonian where $\hat{S}$ is the effective spin.

For a molecule with a single unpaired electron the Zeeman energies can be calculated by the first order perturbation theory as follows where the field *H* is along the z axis.

$$\begin{aligned} E &= \beta \cdot H \cdot \langle \psi_0 \alpha \,|\, L_z + g_e S_z \,|\, \psi_0 \alpha \rangle \\ &= \beta \cdot H \cdot \langle \psi_0 \,|\, L_z \,|\, \psi_0 \rangle + g_e \cdot \beta \cdot H \cdot \langle \alpha \,|\, S_z \,|\, \alpha \rangle \\ &= \beta \cdot H \cdot \langle L_z \rangle + \frac{1}{2} \beta \cdot H \cdot g_e \end{aligned} \qquad \text{Equation 2.25}$$

For molecules without orbitally degenerated ground states the mean value L_z vanishes, so that the energy is just $1/2\beta H g_e$, whereby g_e is a free electron *g* value. L_z is represented by the quantum mechanical operator

$$L_z = -i\hbar \frac{\partial}{\partial \varphi} \qquad \text{Equation 2.26}$$

and the wave function of non-degenerated state is always real

$$L_z = -i\hbar \int \psi_0 \frac{\partial}{\partial \varphi} \psi_0 dv = -i\hbar \frac{\partial}{\partial \varphi} \int (\frac{1}{2}) \psi_0 \psi_0 dv = 0 \qquad \text{Equation 2.27}$$

Systems with an odd number of electrons can acquire a small contribution of angular orbital momentum only through spin-orbit coupling given by the following expression 2.28 where ζ is the spin-orbit coupling constant. The ground state wave function is mixed with the excited states, so that the modified wave function is

$$|+\rangle = |\psi_0\alpha\rangle - \sum_n \frac{\langle n|\zeta L\cdot S|\psi_0\alpha\rangle}{E_n - E_0} \qquad \text{Equation 2.28}$$

The operator $L\cdot S$ can be expressed in form

$$L\cdot S = L_z S_z + \frac{1}{2}(L^+S^- + L^-S^+) \qquad \text{Equation 2.29}$$

with ladder operators L^+ and L^- which operate on the space wave functions ψ_0 und ψ_n. The coupling term L_zS_z is responsible for the mixing of $|\psi_0\alpha\rangle$ and $|\psi_n\alpha\rangle$ whereby the spin is still unchanged. The $1/2L^+S^-$ mixes the α ground state with the β excited states, so that the following wave functions are obtained

$$|+\rangle = |\psi_0\alpha\rangle - \frac{1}{2}\zeta\sum_n \frac{\langle\psi_n|L_z|\psi_0\rangle}{E_n - E_0}|\psi_n\alpha\rangle - \frac{1}{2}\zeta\sum_n \frac{\langle\psi_n|L_x + iL_y|\psi_0\rangle}{E_n - E_0}|\psi_n\beta\rangle \qquad \text{Equation 2.30}$$

Spin-orbit coupling converts the unperturbated state $|\psi_0\beta\rangle$ into a corrected function

$$|-\rangle = |\psi_0\beta\rangle + \frac{1}{2}\zeta\sum_n \frac{\langle\psi_n|L_z|\psi_0\rangle}{E_n - E_0}|\psi_n\beta\rangle - \frac{1}{2}\zeta\sum_n \frac{\langle\psi_n|L_x - iL_y|\psi_0\rangle}{E_n - E_0}|\psi_n\alpha\rangle \qquad \text{Equation 2.31}$$

|+> and |-> are eigenstates of the fictitious spin $\hat{S}$. The operators $\hat{S}_x$, $\hat{S}_y$ and $\hat{S}_z$ act on the these states in the same way as S_x, S_y and S_z do on the states |α> and |β>, so that

$$\hat{S}_z|+\rangle = \frac{1}{2}|+\rangle, \hat{S}_x|+\rangle = \frac{1}{2}|-\rangle$$
$$\hat{S}_z|-\rangle = \frac{1}{2}|-\rangle, \hat{S}_y|+\rangle = \frac{1}{2}i|-\rangle \quad \text{etc.} \qquad \text{Equation 2.32}$$

The spin Hamiltonian along the *z* axis is represented as follows

$$\mathcal{H} = \beta \cdot H \cdot (g_{zx} \cdot \hat{S}_x + g_{zy} \cdot \hat{S}_y + g_{zz} \cdot \hat{S}_z) \qquad \text{Equation 2.33}$$

$$\begin{array}{c} \\ \langle + | \\ \langle - | \end{array} \begin{array}{c} \begin{array}{cc} |+\rangle & |-\rangle \end{array} \\ \begin{pmatrix} \frac{1}{2}\beta H g_{zz} & \frac{1}{2}\beta H (g_{zx} - i g_{zy}) \\ \frac{1}{2}\beta H (g_{zx} - i g_{zy}) & -\frac{1}{2}\beta H g_{zz} \end{pmatrix} \end{array} \qquad \text{Equation 2.34}$$

The true Zeeman Hamiltonian $\beta H(L_z+g_eS_z)$ is given by

$$\beta H \begin{bmatrix} \langle + | L_z + g_e S_z | + \rangle & \langle + | L_z + g_e S_z | - \rangle \\ \langle - | L_z + g_e S_z | + \rangle & \langle - | L_z + g_e S_z | - \rangle \end{bmatrix} \qquad \text{Equation 2.35}$$

If the two matrices are identical, the *g*-tensor becomes

$$g_{zz} = 2 \langle + | L_z + g_e S_z | + \rangle \qquad \text{Equation 2.36}$$

$$g_{zx} + i g_{zy} = 2 \langle - | L_z + g_e S_z | + \rangle \text{ etc.} \qquad \text{Equation 2.37}$$

It is necessary to calculate <+|L_z|+> and <+|S_z|+>. To first order in ζ S_z has the value of 1/2 and L_z is calculated from the excited states with spin β.

$$g_{zz} = g_e - 2\zeta \sum_n \frac{\langle \psi_0 | L_z | \psi_n \rangle \langle \psi_n | L_z | \psi_0 \rangle}{E_n - E_0} \qquad \text{Equation 2.38}$$

The calculation of the cross components <-|L_z|+> and <-|S_z|+> is given e. g. as

$$g_{zx} = g_e - 2\zeta \sum_n \frac{\langle \psi_0 | L_z | \psi_n \rangle \langle \psi_n | L_x | \psi_0 \rangle}{E_n - E_0} \qquad \text{Equation 2.39}$$

In summary it is important to say, that the *g*-tensor applies only for the ground state ψ_0 and has in general different components in other terms ψ_n [40, 51, 52].
The expressions of the *g*-tensor are less straightforward if it is anisotropic. At the same time this behavior leads to more information about the electronic structure of the investigated ion.

The *g* tensor is anisotropic if the electron has spin and orbital angular momentum. As already mentioned the interaction between the magnetic field *H* and the electron spin angular momentum can be represented as $\beta \cdot H \cdot g \cdot S$.

At the beginning the set of the orthogonal axes *x*, *y* and *z* fixed in the crystal is chosen. These axes are usually not the principal directions of the *g* tensor. The spin Hamiltonian is this case

$$\mathcal{H} = \beta \cdot [H_x, H_y, H_z] \cdot \begin{bmatrix} g_{xx} & g_{xy} & g_{xz} \\ g_{yx} & g_{yy} & g_{yz} \\ g_{zx} & g_{zy} & g_{zz} \end{bmatrix} \cdot \begin{bmatrix} S_x \\ S_y \\ S_z \end{bmatrix} \qquad \text{Equation 2.40}$$

The electron spin does not directly interact with the field **H**. It affects the magnitude and the direction of the vector $H \cdot g$. The direction is given by a unit vector *h*' and the magnitude by $H \cdot g'$ [39, 40].

$$h' \, H \cdot g' = \mathbf{H} \cdot g \qquad \text{Equation 2.41}$$

The number *g*' is quantized along the direction *h*' and describes the magnetic moment of the molecular spin. Two spin states exist with a quantization along h' and the energies $\pm(1/2) g' \beta H$. The separation between electron spin levels is equal to $g' \beta H$.

$$(\Delta E)^2 = g'^2 \beta^2 H^2 = \beta^2 (\mathbf{H} \cdot \mathbf{g})(\mathbf{g} \cdot \mathbf{H}) = \beta^2 \mathbf{H} \cdot \mathbf{g}^2 \cdot \mathbf{H} \qquad \text{Equation 2.42}$$

$\mathbf{g}^2$ is the square of the *g*-tensor. In the experiment the apparent g value is measured. The magnetic field **H** has directions I_x, I_y, I_z relativ to the crystal axes, so that the equation 2.43 is obtained

$$(g')^2 = \begin{bmatrix} I_x I_y I_z \end{bmatrix} \begin{bmatrix} (g^2)_{xx} & (g^2)_{xy} & (g^2)_{xz} \\ (g^2)_{yx} & (g^2)_{yy} & (g^2)_{yz} \\ (g^2)_{zx} & (g^2)_{zy} & (g^2)_{zz} \end{bmatrix} \begin{bmatrix} I_x \\ I_y \\ I_z \end{bmatrix} \qquad \text{Equation 2.43}$$

The measurement of the *g*' value at different orientations leads to the elements of the tensor $\mathbf{g}^2$, which can be transformed to the principal axes. By considering the rotating plane as xy, the relation between $\mathbf{g}^2$ and direction cosines are

$$(g')^2 = (g^2)_{xx} \cos^2\theta + (g^2)_{xy} \sin\theta\cos\theta + (g^2)_{yy} \sin^2\theta \qquad \text{Equation 2.44}$$

so that three tensor elements are measured in the experiment. Measurements of the xz and yz planes give the other three values, respectively.

2.5.1 Ions with Kramers degeneracy

The crystal field leads for ions with an odd number of electrons (half integer values of *J*) to a twofold degeneracy according to Krames theorem, so that the levels consist of (*J* + 1/2) doublets. The maximum value of *J* in the ground state is 15/2 for Erbium(III). The wave-functions of the Kramers doublets are linear combinations of states $|\pm M\rangle$ of the form

$$\begin{aligned} &\pm\frac{15}{2},\pm\frac{3}{2},\pm\frac{9}{2},\\ &\pm\frac{13}{2},\pm\frac{1}{2},\pm\frac{11}{2},\\ &\pm\frac{7}{2},\pm\frac{5}{2} \end{aligned} \qquad \text{Equation 2.45}$$

As already mentioned the actual energy levels depend on the size of the crystal field parameters. The energy difference between two states for the doublets is 10 to100 cm^{-1}, so that a magnetic resonance transtion is observed in the microwave region only between the two components of a doublet. At higher temperatures where excited doublets are populated, the lifetimes of the excited state is rather short, so that the resonance is always restricted to the ground state doublet.

To find the resonance condition the Zeeman effect for each doublet has to be calculated. In the first approximation the Zeeman operator **L**+2**S** reduces to the simpler form $g_j\mathbf{J}$. The calculation of the first-order Zeeman effect is reduced to find the matrix elements of J_x, J_y and J_z within each doublet. In case of axial symmetry the elements of J_x, J_y are equal, but normally different from J_z. Each doublet is described by a spin Hamiltonian with a spin S = 1/2 and an ansitropic g tensor with axial symmetry as follows

$$\mathcal{H} = g_{\|}\beta\cdot H_z\cdot S_z + g_{\perp}\beta\cdot(H_x\cdot S_x + H_y\cdot S_y) \qquad \text{Equation 2.46}$$

with

$$\begin{aligned} g_{\|} &= 2\langle J\,||\,\Lambda\,||\,J\rangle\langle +|J_z|+\rangle,\\ g_{\perp} &= \langle J\,||\,\Lambda\,||\,J\rangle\langle +|J_+|-\rangle. \end{aligned} \qquad \text{Equation 2.47}$$

It is already seen that there are no matrix elements of the operators J_+, J_- between the two states of the first doublet in 2.45, so that $g_\perp$ is zero and no transition is allowed within the

doublet. In case of other two doublets $g_\perp$ the transitions are allowed. Both *g* values can be measured by resonance experiments with the external field directed parallel or perpendicular to the *z*-axis. For the second doublet from 2.45 all the admixture coefficients can be calculated. E. g. for the third doublet written

$$cos\,\theta\,|\pm\frac{7}{2}\rangle + sin\,\theta\,|\mp\frac{5}{2}\rangle \qquad \text{Equation 2.48}$$

The following relations are given

$$g_{\parallel} = \langle J\,||\,\Lambda\,||\,J\rangle\left(cos^2\theta - 5\,sin^2\theta\right),$$
$$|\,g_\perp\,| = \langle J\,||\,\Lambda\,||\,J\rangle 2\,|cos^2\theta - 5\,sin^2\theta\,|\left\{(J+\frac{7}{2})(J-\frac{5}{2})\right\}^{\frac{1}{2}}. \qquad \text{Equation 2.48}$$

In more accurate measurements it may be necessary to take into account corrections of $\langle J\,||\,\Lambda\,||\,J\rangle$. One of these is the use of 2.0023 for g_s instead of 2. The other important correction to the Zeeman energy calculation is given by the linear combination of states of different *J*.

For J < 11/2 the second doublet is $|\pm\frac{1}{2}\rangle$, where the *g* values are completely defined if admixtures of different *J* are neglected

$$g_{\parallel} = \langle J\,||\,\Lambda\,||\,J\rangle; g_\perp = \left(J+\frac{1}{2}\right)\langle J\,||\,\Lambda\,||\,J\rangle. \qquad \text{Equation 2.49}$$

The first doublet will include only the values $|\pm\frac{3}{2}\rangle$ and $|\mp\frac{9}{2}\rangle$, so that it can be written similar to equation 2.48. For every doublet with states involving two values of J_z another orthogonal doublet with different energy exists, given by changing θ to $\theta + \pi/2$. If three values of J_z are admixed there are three orthogonal doublets with different energies.

If the Zeeman energy is not small compared to the crystal field splittings it is necessary to consider higher-order Zeeman effects. The second-order effect affects both levels of a doublet and therefore does not change the frequency of a transition between the two states of a doublet. The third-order effect changes the transition energy since it can have the opposite

sign for the two components of a doublet. It modifies the wave function of a doublet in the following form

$$\left(1+\alpha^2\right)^{-\frac{1}{2}}\left\{|+\rangle+\alpha|+'\rangle\right\}$$
$$\left(1+\alpha^2\right)^{-\frac{1}{2}}\left\{|-\rangle+\alpha|-'\rangle\right\}$$

Equation 2.50

α is an admixture coefficient for the other states and is proportional to *H*. By using the modified states for the calculation of the first-order Zeeman effect its energy will be modified by the fraction of order α^2, so that a correction to the energy separation of order H^3 is obtained. This effect ist most pronounced for a doublet state, where $g_\perp = 0$, which is splitted by a perpendicular magnetic field in third-order and leads to the weak allowed transitions at high magnetic fields [40, 53].

2.5.2 Non-Kramers ions

In case of rare earth elements with an even number of *f* electrons the *J* numbers are integers. The maximal value of *J* is eight for holmium(III). The effect of spin operators on a manifold of 2*J*+1 states is to give a series of doublet and singlet energy levels. The doublets are of the form

$$\pm 8, \pm 2, \pm 4,$$
$$\pm 7, \pm 1, \pm 5,$$

Equation 2.51

while the singlets are linear combinations of the form

$$|3^s\rangle = \frac{1}{\sqrt{2}}\left\{|+3\rangle+|-3\rangle\right\}; |3^a\rangle = \frac{1}{\sqrt{2}}\left\{|+3\rangle-|-3\rangle\right\}$$

Equation 2.52

or of the form +6, 0, -6. The degeneracy of the states $M = \pm 3$ is lifted by the V_6^6 term in the crystal field, which has a coupling matrix element for states of the simple symmetrical and antisymmetrical form as given in 2.52. The operator J_z has a matrix element $\langle 3^s | J_z | 3^a \rangle = 3$, whereby follows that the magnetic field along the *z*-axis produces transitions between the states 3^S and 3^α. This transition is usually observed in the infrared region.

In a similar way the states $M = \pm 6$ are split through the action of V^6 term with the following matrix elements $\langle +6 | V_6^6 | 0 \rangle = \langle 0 | V_6^6 | -6 \rangle$.

By chosing the linear combinations 2.52 as basic states this energy matrix can be simplified as follows

$$|6^S\rangle = \frac{1}{\sqrt{2}}\{|+6\rangle + |-6\rangle\}; |6^a\rangle = \frac{1}{\sqrt{2}}\{|+6\rangle - |-6\rangle\} \qquad \text{Equation 2.53}$$

since the second state $|6^a\rangle$ has no matrix element with $|0\rangle$ and is an eigenstate. The other eigenstates can be found from the energy matrix

$$\begin{array}{c|cc} & |6^s\rangle & |0\rangle \\ |6^s\rangle & 0 & \sqrt{(2)}c \\ |0\rangle & \sqrt{(2)}c & d \end{array}$$

where $d = \langle 0 | \sum_k V_k^0 | 0 \rangle - \langle 6 | \sum_k V_k^0 | 6 \rangle$ and $c = \langle 0 | V_6^6 | \pm 6 \rangle$. The eigenstates are of the form

$$p|6^S\rangle + q|0\rangle; (p^2 + q^2 = 1) \qquad \text{Equation 2.54}$$

Initially the ground doublet states are

$|\xi'\rangle = p|6^S\rangle + q|0\rangle$

$|\eta'\rangle = |6^a\rangle$

where q is small and p is close to unity. These states are replaced by the following linear combinations if a magnetic field is present

$$\begin{aligned} |\xi\rangle &= \frac{1}{\sqrt{2}}(|\xi'\rangle + |\eta'\rangle) = \frac{1}{2}(1+p)|+6\rangle - \frac{1}{2}(1-p)|-6\rangle + (q/\sqrt{2}|0\rangle \\ |\eta\rangle &= \frac{1}{\sqrt{2}}(|\xi'\rangle - |\eta'\rangle) = -\frac{1}{2}(1-p)|+6\rangle + \frac{1}{2}(1+p)|-6\rangle + (q/\sqrt{2}|0\rangle. \end{aligned} \qquad \text{Equation 2.55}$$

The Zeeman interaction $\mathbf{Z} = -\boldsymbol{\mu}.\ \mathbf{H} = \Lambda \cdot \beta \cdot \mathbf{J}.\ \mathbf{H}$ has no matrix elements between $|\xi'\rangle$ and $|\eta'\rangle$ and has opposite expectation values of opposite sign in either state:

$$\langle \xi | Z | \xi \rangle = -\langle \eta | Z | \eta \rangle = 6\Lambda\beta p H_z \approx 6\Lambda\beta(1 - \frac{q^2}{2})H_z \qquad \text{Equation 2.56}$$

The spin Hamiltonian can be written by using a fictitious spin $S = 1/2$ as follows

$$\mathcal{H} = g_{\|}\beta \cdot H_z \cdot S_z + \Delta_x \cdot S_x + \Delta_y \cdot S_y \qquad \text{Equation 2.57}$$

where

$$g_{\|} = 12\Lambda(1-\frac{q^2}{2}) = 12\Lambda(1-\frac{c^2}{d^2})$$
$$\Delta = (\Delta_x^2 + \Delta_y^2)^{\frac{1}{2}} = 2\frac{c^2}{d}. \qquad \text{Equation 2.58}$$

Transitions occur at

$$\hbar\omega = \left\{(g_{\|}\beta H_z)^2 + \Delta^2\right\}^{\frac{1}{2}} \qquad \text{Equation 2.59}$$

and are allowed if the magnetic field is along the *z*-axis. The square of the magnetic dipole matrix element for the transition is

$$|\mu^2| = \frac{1}{4}(g_{\|}\beta\Delta/\hbar\omega)^2 \qquad \text{Equation 2.60}$$

Thus, the magnetic dipole decreases if the frequency increases. This corresponds to a change from the states $|\xi'\rangle$ and $|\eta'\rangle$ which are correct without magnetic field, through intermediate states in a finite magnetic field to the states $|\xi'\rangle$ and $|\eta'\rangle$ from equation 2.55, which are correct if the Zeeman interaction is very large compared to Δ.

The operation of J_j on the two doublet states operating with J_z gives diagonal matrix elements with opposite sign. If the magnetic field is along *z*-axis they have a linear Zeeman splitting. There are no matrix elements between the two states, therefore no Zeeman splitting is observed for a perpendicular magnetic field. In case of non-Kramer ions the doublets can be split by a crystal field of lower symmetry, which can arise through the Jahn-Teller effect or through crystal defects. Any such splitting that results from a matrix element of the distorted crystal field between two states of the doublet will admix the two states, so that the transition is allowed with a magnetic field along *z*-axis. The spin Hamiltonian for this doublet is given by Eq. 2.57 with certain values of Δ_x and Δ_y. Δ has more than one value. The energy required

for a transition is given by 2.59 and depends on Δ. The transition intensity depends on Δ, too (Eq. 2.60), and vanishes if $\Delta = 0$, so that a broad assymetric line is expected.

When the site symmetry of the lanthanide ion has no inversion symmetry, a non-Kramer ion can have an electric dipole moment normal to this plane. For example in case of the C_{3h} point group there is only one plane of reflection symmetry, normal to the *c*-axis. The electric dipole moment for a non-Kramer ion can be observed normal to the *c*-axis, but not parallel. If an additional term represents the effect of the electric field on this dipole moment $g_{\perp}^{(E)}\beta\cdot(E_x\cdot S_x + E_y\cdot S_y)$ in the spin Hamiltionian, transitions are allowed for an eletric field $(E_1)_{\perp}$ normal to the *c*-axis, whereby the intensity is depend on $(g_{\perp}^{(E)}E_1)^2$.

If resonance is observed at constant frequency and variable magnetic field, it will lie at field strengths below the value $H_0 = (\hbar\omega / g_{\parallel}\beta)$ corresponding to $\Delta = 0$, and will be assymetric in shape. If the transition is due to $(H_1)_{\parallel}$ it will have zero intensity at $H_z = H_0$, whereby if it is due to $(E_1)_{\perp}$ it will have a finite intensity at $H_z = H_0$.

The hyperfine Hamiltonian for a non-Kramer doublet has the form

$$A_{\parallel}S_zI_z + P_{\parallel}\left\{I_z^2 - \frac{1}{3}I(I+1)\right\} \qquad \text{Equation 2.61}$$

with just one change compared to the behavior discussed above, that $g_{\parallel}\cdot\beta\cdot H_z$ must be replaced by $(g_{\parallel}\cdot\beta\cdot H_z + A_{\parallel}m)$ in 2.59 for each hyperfine component, where $m = I_z$ [40, 53].

3 Characterization methods

3.1 Single-crystal UV/vis/NIR spectroscopy

The colour of lanthanide compounds is caused by electronic transitions through the absorption of light in the Vis region, 400-800 nm (25000-12500 cm^{-1}). Using the UV/Vis absorption spectroscopy electronic transition of lanthanide compounds are investigated in order to determine the symmetry of the chromophore as well as the oxidation state of the lanthanide ion. However, the investigations of the following two kinds of transitions in UV/Vis/NIR spectroscopy are of special importance:

The transition of an electron from one orbital to another at a higher energy state of the same atom. This type of transition is known as *f-f* electron transition, observed in transition metal complexes. These transitions in centrosymmetric chromophores are Laporte-forbidden. However, sometimes it is observed (example in ideal octahedra) where the intensity is comparatively low.

With these processes parts of the electromagnetic radiation are absorbed. The measurements were accomplished at a single-crystal spectrometer CARY 17, which was developed at the Research School of Chemistry (Canberra, Australia) [54, 55]. The schematic diagram of the spectrometer is represented in Figure 3.1. A halogen lamp is used as a light source and a photomultiplier is used as a detector for the measurement at the UV/Vis range (12000-30000 cm^{-1}). For measurement in the near infrared (6000-16000 cm^{-1}) region, a germanium semiconductor detector is used, which was cooled in liquid nitrogen. A polarization filter allows measurements at horizontal as well as vertical polarization of the incident light beam.

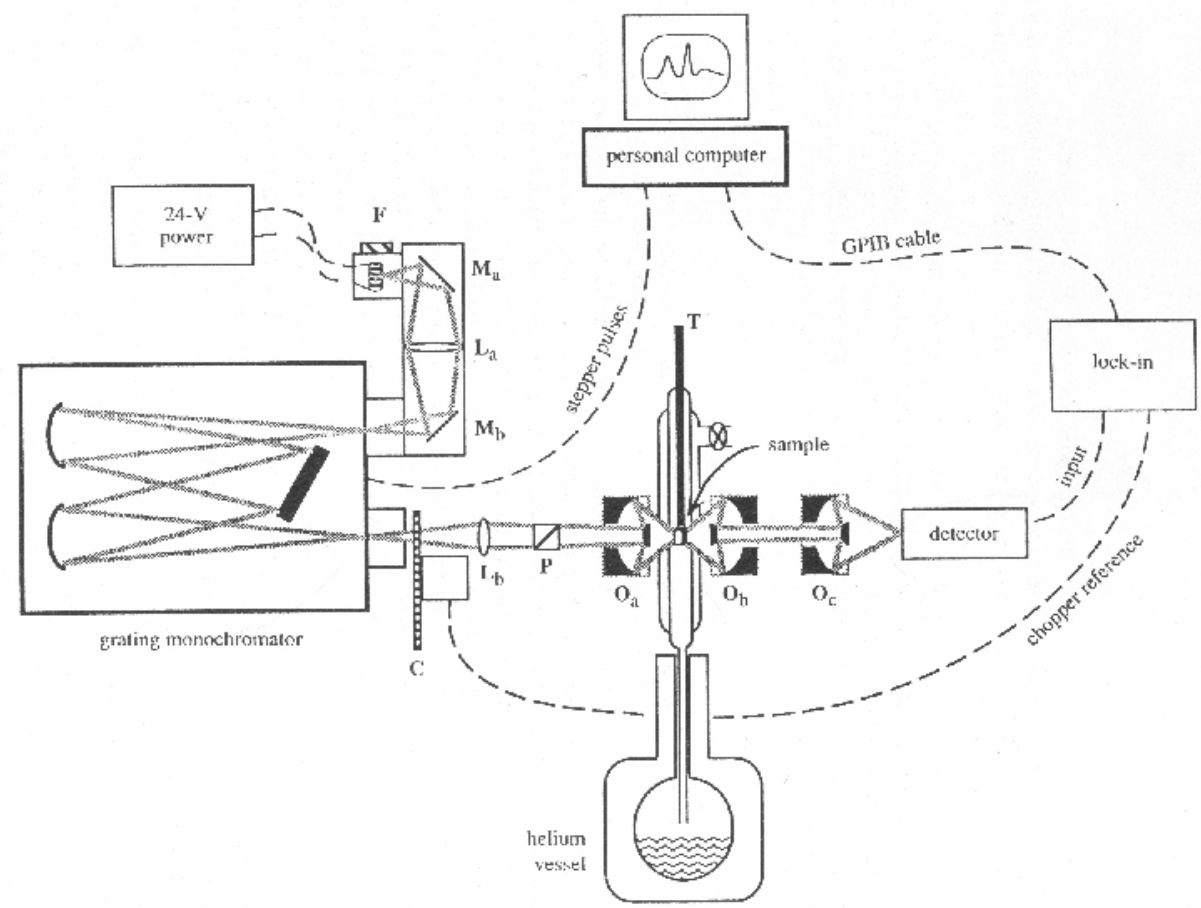

Figure 3.1. Schematic construction of microcrystal UV/Vis/NIR spectrophotometer CARY 17 [55].

A small transparent single-crystal is selected under a microscope. Subsequently, an aluminum foil is attached on a sample holder so that the holes of the sample holder are masked. Under the microscope two equally large holes (sample hole and reference hole) are made into the foil with the help of pin. The holes should be some smaller than the selected crystals. The crystal is then carefully placed on the grease at the sample hole under the microscope (Fig. 3.2). Grease has been introduced before to attach the crystal. The sample holder is then placed to the spectrophotometer for the measurement of the absorption spectra of the crystal. It is necessary to mention that a base line measurement with the reference hole is necessary for each measurement.

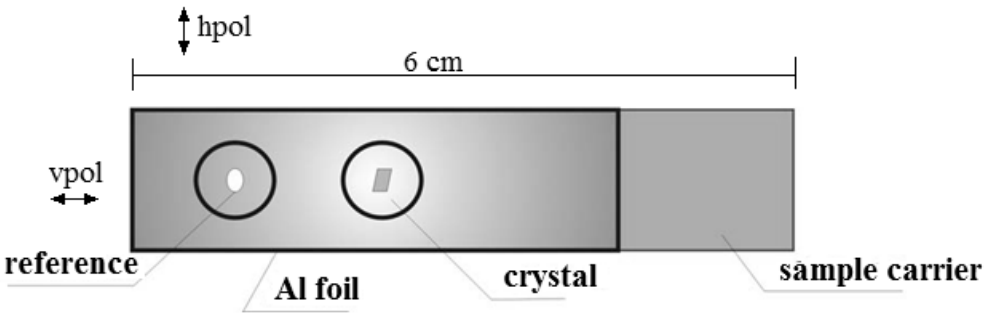

Figure 3.2. Sample holder for the single-crystal photometer. After fixing on spectrometer the indicated polarisation directions are given.

The Lambert-Beer- law (eq 3.2) represents the link between the measured intensity *I*, baseline I_0 and on the other side concentration *c*, molar absorption coefficient *ε*, and thikness of the crystal *l*. The plot of *A* or, if the concentration *c* and thickness of the crystal are known, ε against the wavenumber or wavelength produces the absorption spectra. The concentration of the chromophors [LnL_n] can by calculated from the number of formula units (Eq. 3.1).

$$c = \frac{Z}{N_A \cdot V}$$ Equation 3.1

c concentration (mol/m^3)
Z number of formula units
V cell volume (m^3)

$$A = \log \frac{I_0}{I} = \varepsilon \cdot c \cdot l$$ Equation 3.2

I_0 intensity of the incident beam
I intensity of the transmitted beam
c concentration of chromophore
ε molar absorption coefficient
l thickness of the crystal

The dimensionless ratio I_0/I is called transmittance. The negative logarithm of transmittance is known as absorbance or optical density and is represented by *A*. For the grafical representation in this work the absorbance in relative units is plotted against the wavenumber. The thickness of the crystals was not considered. It was always around 0.1 mm.

3.2 Powder reflectance spectrometry

The light absorption of diffuse scattering materials is analyzed by powder reflectance spectroscopy. The accurate energies of the absorption bands of a material can be obtained by this method, so that a statement about the color of the material can be made. For measurements spectral photometer Cary 17 modified by OLIS Inc. is used for the wavelength range $400 \leq \lambda \leq 2600$ nm. A halogen bulb serves as light source, optical lattice as a monochromator. The light coming from the monochromator is directed to the sample via a mirror system. Different detectors are used depending on the wavelength range. A photomultiplier is applied for the UV/vis range and PbS- or InP-semiconductor for the infrared range. The thechnical sketch of the measuring cell is given in Figure 3.1. About 200 mg of a sample were typically used for the powder reflectance measurements. $BaSO_4$ powder is used as a white standard (purity p.A., Firma Merck). It is also used for the dilution of intensively colored samples to prevent too strong absorption. The reflectance is calculated by the MUNK-KUBELKA function [56] (equation 3.3) and plotted against the wavelength or wavenumber for grafical representation.

Both methods (powder reflectance spectrometry and Single-crystal spectroscopy) show several advantages and disadvantages. Single-crystal UV/vis spectroscopy provides certain information about the intensities and a better resolution of the spectra. Direction-dependent (anisotropic) measurements are possible in comparison to powder reflectance spectroscopy. In contrast all transitions can be detected by powder reflectance spectroscopy, because crystallites in the powder are oriented in all directions. For the measurement of all three crystallografic directions the single crystal should be specially cut. This is rarely possible. A further disadvantage of the single-crystal UV/vis method is the absence of single-crystals of many compounds. For that reason only powder reflectance spectra of those materials could be measured.

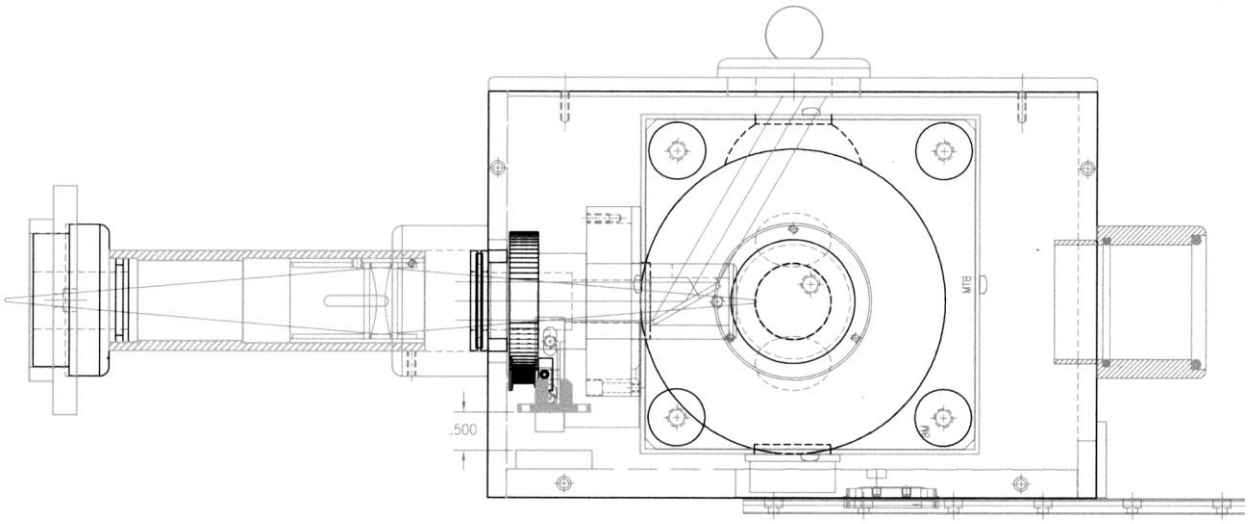

Figure 3.3 Schematic construction of the Ulbricht sphere [57]. S = mirrow, L = lens system, M = detector, B = diaphragm slide, RL = scattered light und P = sample.

$$F(R_\infty) = \frac{(1-R_\infty)^2}{2R_\infty} \text{ with } R_\infty = \frac{R_{Pr}}{R_{St}} \qquad \text{Equation 3.3}$$

$F(R_\infty)$ degree of reclection

R_{Pr} reflection of the sample

R_{St} reflection of the standard

3.3 Vibrating Sample Magnetometer (VSM)

The Vibrating Sample Magnetometer is used nowadays for determination of the magnetic properties of materials. The measuring device has a flexible design and high sensibillity at one's command. It is possible to mount and exchange easily the samples. The VSM method is based on the Faraday's induction law. The current induced by oscillating of a sample in a pick-up coil is directly proportional to a magnetic moment of an investigated material.

For those measurements a magnetized sample is put in vibration in a homogenous static magnetic field. A magnetic dipole moment of a material produces a magnetic field around the sample called magnetic scatter field. This field changes through the vibration and is measured by detection coils as a function of time. This field induces an electrical field in detector coils according to Faraday's law. The signal is amplified by a lock-in amplifier. The magnetic moment can be determined via calibration with a reference sample.

3.4 Superconducting Quantum Interference Device (SQUID)

Another device for the measurements of magnetic properties of different materials is SQUID (Superconducting Quantum Interference Device). This method allows magnetic measurements for the temperature range between 1.7 K and 800 K and magnetic field force from 500 Oe until 70000 Oe.

The detector coils (flux transformer) are interspersed the homogenous external field at the time of the measurement. The applied magnetic field induced a screening current inside of the flux transformer. According to Lenz's law this current has such a direction that the original field is compensated. The magnetic field generated by the superconducting magnetic coil leads to the magnetization of the sample. The sample field is directed either parallel (paramagnetic) or antiparallel (diamagnetic) to the external field. In a sensitive region of the transformer additional screening currents are induced due to the interfering field of the sample produced by entry of the magnetic flux into a defined coil region. These currents enhance or attenuate the original inductive current depend on the direction of the interfering field. Whereas the total flux inside the superconducting loop has to be constant, flux variations occur in the further coil regions.

The combination of two anti-clockwise detector coils (Fig. 3.4) allows determination of the magnetic field gradient by the flux transformer.

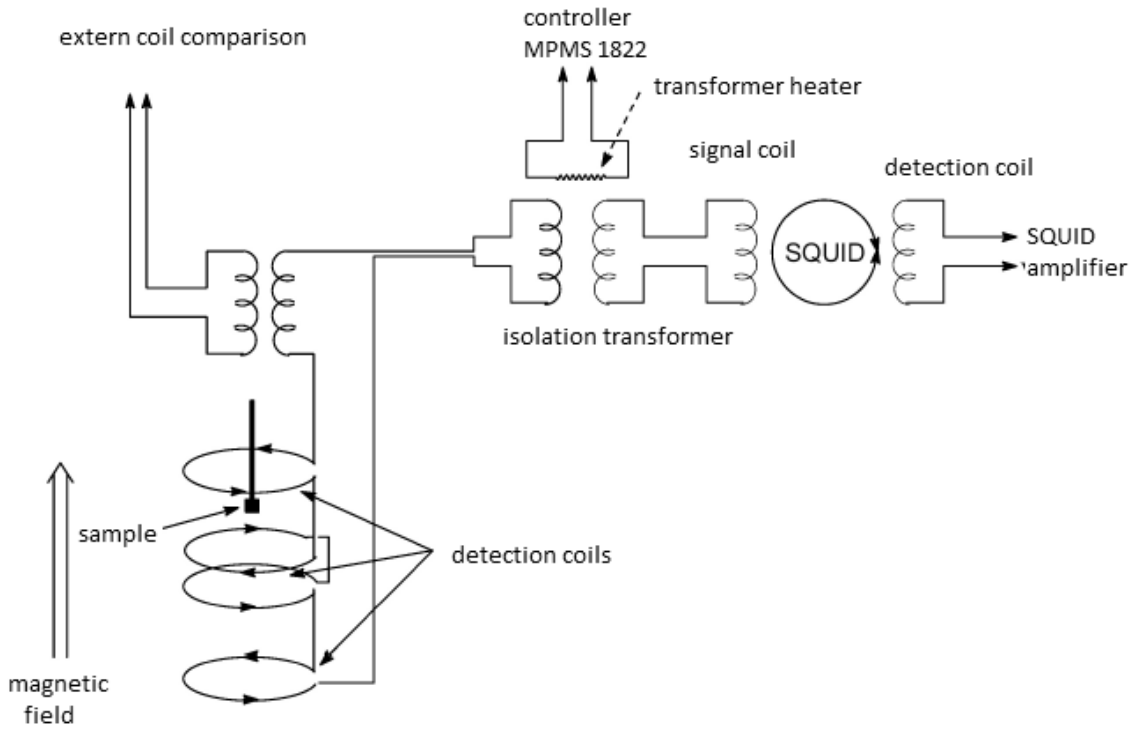

Figure 3.4. Schematic construction of the superconducting detector coils, sensors and signal transmitting elements of SQUID magnetometer [58].

The isolation transformer allows a separation between the tapped voltage signal inside the detector coils and electric circuit inside the actual SQUID. After each measuring process new zero adjustment proceeds due to the increase of the temperature above the critical temperature T_c of the superconductor. The measured voltage is a measure of the field change inside the flux transformer and is transfered to a signal coil of the SQUID sensor. This sensor is built from a superconducting ring (see Fig 3.5) with a "*weak link*" region. The ring is realised by two parallel JOSEPHSON junctions [58].

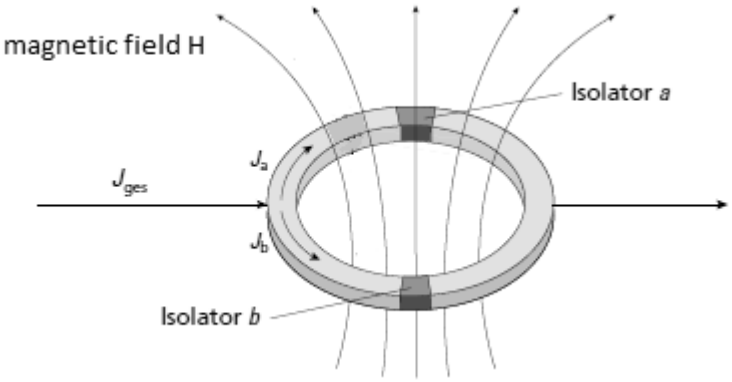

Figure 3.5. Schematic construction of the SQUID sensor.

4 The Computer Program BonnMag

In master thesis [59] preceding the work for this dissertation the computer program BonnMag was developed. This program is based on the program SURGEV which was developed by W. URLAND during the 1970s [60]. Eigenvalues, eigenvectors and magnetic susceptibilities of f^1 to f^3 and f^{11} to f^{13}-systems were calculated with SURGEV within the angular overlap model [61, 62, 63]. At that time very good matches of the experimental excited state energies and magnetic properties compared to other model calculations [64, 65, 66] were obtained.

SURGEV was used as a starting point for the development of BonnMag. BonnMag contains an import routine for the NIELSON AND KOSTER coefficients [67]. With this extension and extended delimiters for all matrix dimensions all f^n-systems can be calculated by BonnMag. The input file was restructured to make it similar to the input used by CAMMAG [68, 69, 70]. This relation to CAMMAG was intended to simplify the use of BonnMag and to allow users of CAMMAG easy and fast access to BonnMag.

BonnMag calculates the orbital energies of the free ions using the Slater-Condon-Shortley parameters F_2, F_4, F_6 and the spin orbital coupling constant ζ (Figure 4.1). These energy levels are compiled from spectroscopical data of different lanthanide compounds. This data set is known as DIEKE diagram [71].

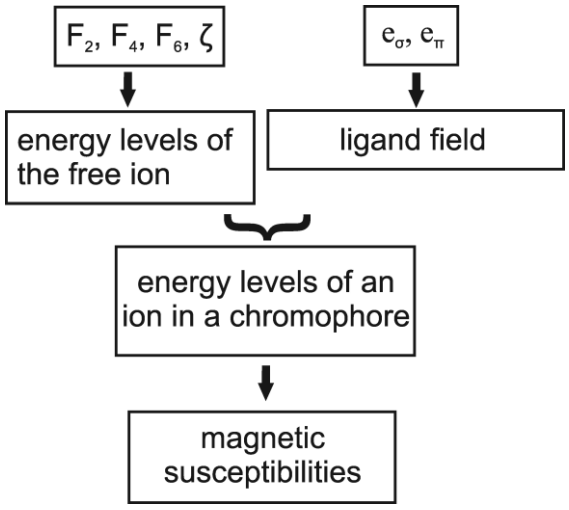

Figure 4.1. Relation between parameters and calculated values.

In the next step the full configuration interaction matrix using reduced matrix elements [87] is calculated. The corresponding eigenvalues are the f^n state-energy levels. The ligands are taken into account through interaction parameters e_σ and e_π. In this way energy levels are

obtained that include ligand field splitting. The energy states are used for the calculation of magnetic moments in the VAN VLECK formalism[12] (Figure 4.1).

In this thesis BonnMag has been further developed by implementing a symmetry analysis of the eigenvectors for all thirty-two lattice point groups (see chapter 4.1), estimation of intensities for electric dipole transitions using Judd-Ofelt theory (see chapter 4.4), and calculation of the tensor of inertia of the chromophore (see chapter 4.2) for checking of the given *z*-axis (necessary for symmetry analysis) and applied to different examples.

4.1 Symmetry analysis

For the implementation of the symmetry analysis [72] split terms knowledge of group theory and its relation to the calculated eigenvectors is necessary. The irreducible representation of every f^n state is calculated by analysing the corresponding eigenvector. In this case the global *z*-axis has to be choosen in accordance with the point group of the chromophore.

At first *J* projections (the sum of all non-zero contributions with the same *J* value in an eigenvector) are performed for every electronic state in order to determine the term with the largest contribution to the split term. This is achieved by summation of the squares of the individual contributions in each eigenvector for every *J* term. For example the ground state of praseodymium (f^2) is $^3H_4$. By projecting the *J* parts the contribution with the largest contribution appears for $J = 4$. If different states mix with each other, then contributions of these states with various *J* are calculated and given for the concerned energy state (Table 4.1).

Table 4.1 Splitting of ^3H due to the spin-orbit-coupling and the ligand-field for the octahedral $[Pr^{III}L_6]$ chromophore with *J* projections.

State (number of split tems)	$J = 1$	$J = 2$	$J = 3$	$J = 4$	$J = 5$	$J = 6$
$^3H_4$ (9)	0	0	0	1.0	0	0
$^3H_5$ (11)	0	0	0	0	1.0	0
$^3H_6$ (13)	0	0	0	0	0	1.0

For the correct assignment of transitions detailed analysis respectively the group theory is required. Every state is assigned an irreducible representation dependent on the point or double group of the complex.

As example the analysis of an erbium(III) in the chromophore $[Er^{III}O_4P_4]$ with D_4 symmetry is performed which was already considered before (section 2.5). The ground state of erbium(III) (f^{11}) is $^4I_{15/2}$, the $16|J,M_j>$ functions of this ground state can be linearly combined. These

linear combinations will have Γ_6 or Γ_7 symmetry in case of half-integer J value for the D_4 double group. Detailed account on the double groups and its properties is given in section 4.1.1.

Table 4.2 Character table for the point group D_4 [74].

	E	**2C$_4$ (z)**	**C$_2$ (z)**	**2C'$_2$**	**2C''$_2$**	**linear functions, rotations**	**quadratic functions**
A$_1$	1	1	1	1	1		x^2+y^2, z^2
A$_2$	1	1	1	-1	-1	z, R_z	
B$_1$	1	-1	1	1	-1		x^2-y^2
B$_2$	1	-1	1	-1	1		xy
E	2	0	-2	0	0	(x, y) (R_x, R_y)	(xz, yz)

The eigenvectors obtained for the from a D_4-symmetric ligand field calculation in the $^4I_{15/2}$ basis belong to these irreducible representations. The symmetry analysis of an eigenvector **V** is performed by applying all symmetry operations R of the point group and the transpose of **V** to get the character $\chi(R)$:

$$\chi(R) = V^t R V \qquad \text{Equation 4.1}$$

For doubly degenerated states **V** has two columns, the diagonals of the transformation 2x2 matrix that results from equation 4.1 are summed. If the basis is size n, then R is represented by a n x n matrix.

At first R has to be determined. Each symmetry operation in a group can be expressed as a rotation or rotation plus inversion. These rotations can be expressed in terms of the three Euler angles φ, θ and χ [72]. The largest R matrix for an f^n system is for n = 7 of order 3432x3432.

For our example it turns out that for $^4I_{15/2}$ in D_4 symmetry the 16|J,M_j> states can be separated into two sets that belong to Γ_6 and Γ_7, respectively. Those M_j that differ by ΔM_j = +/- 4 will be in the same set. In order to assign M_j the proper set those symmetry operations are considered where Γ_6 or Γ_7 have different characters, here C_4 (see table 4.3). Applying this symmetry operation on the 16|15/2,M_j> functions of $^4I_{15/2}$ is the same as multiplying the sixteen element |J,M_j> column vector by a 16x16 matrix $R(\varphi = \pi/2, \theta = 0, \chi = 0)$ which corresponds to $\chi(R) = e^{i \cdot \varphi \cdot Mj}$. This gives complex characters for each M_j state which can be transformed to real numbers by linear combinations of the |+/-M_j> states such as

|15/2+>=1/√2 (|+15/2> + |-15/2>), |15/2->=1/√2 (|+15/2> - |-15/2>) etc.

Applying this for all M_j values (M_j = -J...+J) the following result given in table 4.3 is obtained (only non-zero diagonal elements). According to the character table of the D_4 double group (see table 4.3) $|M_j>$ states +/-15/2, +/-9/2, +/-7/2, +/-1/2 belong to Γ_6 and +/-13/2, +/-11/2, +/-5/2, +/-3/2 to Γ_7. Corresponding calculations can be performed for integral values of J (even electron number). Analysis of M_j states of the point group D_4 using a general rotation axis C_4 leads to an inconclusive assignment of the irreducible representations to each M_j value (see table 4.4) [72].

Table 4.3 Characters for each M_j state for the $^4I_{15/2}$ state in a D_4 ligand field.

M_j	C_4 rotation	Result	M_j	C_4 rotation	Result
15/2	$e^{-i\pi/4}$	$\sqrt{2}$	-1/2	$e^{-i\pi/4}$	$\sqrt{2}$
13/2	$e^{-i3\pi/4}$	$-\sqrt{2}$	-3/2	$e^{-i3\pi/4}$	$-\sqrt{2}$
11/2	$e^{i3\pi/4}$	$-\sqrt{2}$	-5/2	$e^{i3\pi/4}$	$-\sqrt{2}$
9/2	$e^{i\pi/4}$	$\sqrt{2}$	-7/2	$e^{i\pi/4}$	$\sqrt{2}$
7/2	$e^{-i\pi/4}$	$\sqrt{2}$	-9/2	$e^{-i\pi/4}$	$\sqrt{2}$
5/2	$e^{-i3\pi/4}$	$-\sqrt{2}$	-11/2	$e^{-i3\pi/4}$	$-\sqrt{2}$
3/2	$e^{i3\pi/4}$	$-\sqrt{2}$	-13/2	$e^{i3\pi/4}$	$-\sqrt{2}$
1/2	$e^{i\pi/4}$	$\sqrt{2}$	-15/2	$e^{i\pi/4}$	$\sqrt{2}$

Table 4.4 Characters for each integral M_j state for the $^3H_4$ state in a D_4 ligand field with assignment of irreducible representations.

M_j	C_4 rotation	Result	Irreducible representation	M_j	C_4 rotation	Result	Irreducible representation
10	$e^{i\pi}$	-1	Γ_3/Γ_4	-1	$e^{-i\pi/2}$	0	Γ_5
9	$e^{i\pi/2}$	0	Γ_5	-2	$e^{i\pi}$	-1	Γ_3/Γ_4
8	e^{0}	1	Γ_1/Γ_2	-3	$e^{i\pi/2}$	0	Γ_5
7	$e^{-i\pi/2}$	0	Γ_5	-4	e^{0}	1	Γ_1/Γ_2
6	$e^{i\pi}$	-1	Γ_3/Γ_4	-5	$e^{-i\pi/2}$	0	Γ_5
5	$e^{i\pi/2}$	0	Γ_5	-6	$e^{i\pi}$	-1	Γ_3/Γ_4
4	e^{0}	1	Γ_1/Γ_2	-7	$e^{i\pi/2}$	0	Γ_5
3	$e^{-i\pi/2}$	0	Γ_5	-8	e^{0}	1	Γ_1/Γ_2
2	$e^{i\pi}$	-1	Γ_3/Γ_4	-9	$e^{-i\pi/2}$	0	Γ_5
1	$e^{i\pi/2}$	0	Γ_5	-10	$e^{i\pi}$	-1	Γ_3/Γ_4
0	e^{0}	1	Γ_1/Γ_2				

If only $R = C_4$ is considered Γ_1/Γ_2 and Γ_3/Γ_4 can not be distinguished. For that reason an additional symmetry operation has to be applied, where these pairs of irreducible representations have different characters. Inspection of the character table of D_4 shows that the C_2(x) operation has to different characters for Γ_1/Γ_2 and Γ_3/Γ_4. In case of point groups with σ_v mirror plane this operation is replaced by a C_2(x) rotation multiplied with inversion operation. Thus, for our example follows, that if the sign of the eigenvector components for M_j and $-M_j$ are equal, then these M_j values lead to the irreducible representation Γ_1 or Γ_3 with 1 as a character for the C_2(x) operation. If the vector elements for M_j and $-M_j$ have opposite signs this leads to Γ_2 or Γ_4 dependent on the M_j value (see table 4.4) because these representations have -1 as a character for C_2(x). In this way symmetry analysis for all thirty-two point groups have been implemented in BonnMag.

4.1.1 Double groups

For the symmetry analysis of transition metal or rare earth metal complexes with the half-integral value for the total spin or the total momentum quantum number J the point groups were extended by the additional symmetry operation and irreducible representations. In this section a detailed account on this extension is given.

The character of a wave function with quantum number J is defined as

$$\chi(\alpha) = \frac{\sin(J+\frac{1}{2})\alpha}{\sin(\frac{\alpha}{2})} \qquad \text{Equation 4.2}$$

under rotation by an angle α. For rare earth elements the total angular momentum quantum number is used because the spin-orbit coupling can not be neglected. In case of even numbers of f electrons $J = L + S$ becomes an integer. In case of an odd number of electrons and half-integral J numbers the calculation becomes different because the rotation by 2π introduced by Bethe is not an identity operation anymore, which is mathematically but not physically possible. For these cases the characters of the represention must be defined differently [73].

$$\chi(\alpha) = \chi(\alpha + 2\pi) \text{ for } J \text{ is an integer} \qquad \text{Equation 4.3}$$

$$\chi(\alpha+2\pi) = \frac{\sin\left((J+\frac{1}{2})(\alpha+2\pi)\right)}{\sin(\frac{\alpha+2\pi}{2})} = \frac{\sin[(J+\frac{1}{2})\alpha+2\pi]}{\sin(\frac{\alpha}{2}+\pi)} = \frac{\sin(J+\frac{1}{2})\alpha}{-\sin(\frac{\alpha}{2})} = -\chi(\alpha) \qquad \text{Equation 4.4}$$

The general point group operations must be multiplied with the new operation called *R* (rotation). Thus, new operations are obtained and the new group becomes larger. This group is called *double group*.

Multiplication from fight-hand and left-hand side, $C_n^m R$ and RC_n^m, have to be considered which describe the same operation. The rotation by an angle π (C_2 axis) corresponds to the special $\chi(\pi) = \chi(3\pi) = 0$. For any other angle $m2\pi/n$ the equation is $\chi(m2\pi / n + 2\pi) = \chi[(n - \mathrm{m})2\pi / n]$.

For evaluation of the characters for the identity operation *E* and rotation *R* rule by l'Hôspital must be used because $\frac{\sin(J+\frac{1}{2})\alpha}{\sin(\frac{\alpha}{2})} = \frac{0}{0}$ for χ(0) and χ(2π). The results are

$\chi(0) = 2J + 1$

$\chi(2\pi) = 2J + 1$ when *J* is an integer and $-(2J + 1)$ when *J* is a half-integer.

The characters of the new operations are summed in the same classes as the characters of point groups. The number and dimensions of the irreducible representations are also obtained by using the same rules as for point groups. The number of the classes corresponds to the number of irreducible representations and the sum of the squares of dimensions to the group order. We consider here the same example as already described, point and double group D_4. Point group D_4 contains eight operations whereby double group D_4 comprises sixteen operations which belong to seven classes: E, R, C_4 and $C_4^3 R$, C_4^3 and $C_4 R$, C_2 and $C_2 R$, $2C_2^{'}$ and $2C_2^{'}R$, $2C_2^{''}$ and $2C_2^{''}R$ (see table 4.5).

For the labeling of irreducible representations of point groups two different systems are used, Mulliken and Bethe's notation, which uses Γ_i, whereby the double group extension is normally noted only with Bethe's notation [74].

In case of half- integral *J* all wave functions must be two-fold degenerated according to Kramers' theorem [75].The spin degeneracy of a system with an odd number of electrons persists even in absence of an external magnetic field if an environment with the low symmetry lifts other degeneracies.

The direct products of double groups can be calculated and reduced to sums of irreducible representations in the same way as for point groups.

Table 4.5. Character table of double group D_4.

D_4	E	R	C_4/C_4^3R	C_4^3/C_4R	C_2/C_2R	$2C_2'/2C_2'R$	$2C_2''/2C_2''R$
Γ_1 A_1'	1	1	1	1	1	1	1
Γ_2 A_2'	1	1	1	1	1	-1	-1
Γ_3 B_1'	1	1	-1	-1	1	1	-1
Γ_4 B_2	1	1	-1	-1	1	-1	1
Γ_5 E_1'	2	2	0	0	-2	0	0
Γ_6 E_2'	2	-2	$\sqrt{2}$	$-\sqrt{2}$	0	0	0
Γ_7 E_3'	2	-2	$-\sqrt{2}$	$\sqrt{2}$	0	0	0

4.1.2 Full rotation groups

The rotation groups are subgroups of the so called full rotation groups. The set of represention matrices for the rotation group with elements called *R* can be formed by using the (2*J*+1)-fold function space. A full rotation group contains *J* irreducible representations. These matrices are labeled with $D^J(R)$. So that it follows

$$D^J(R) = \sum_\Gamma a_\Gamma D^\Gamma(R) \qquad \text{Equation 4.5}$$

The a_Γ coefficients can be obtained from equation 4.6.

$$\chi^J(R) = \sum_\Gamma a_\Gamma \chi^\Gamma(R) \qquad \text{Equation 4.6}$$

The characters $\chi^J(R)$ are obtained from the equation 4.6 and $\chi^\Gamma(R)$ from the character table of the considered group. D_4 group is taken here as example and the decompositions of D^J representations into the irreducible representations are given in Table 4.6.

Table 4.6. Decomposition of D^J representations for the double group D_4.

	Irreducible representations after decomposition		Irreducible representations after decomposition
D^0	Γ_1	$D^{7/2}$	$2\Gamma_6 + 2\Gamma_7$
$D^{1/2}$	Γ_6	D^4	$2\Gamma_1 + \Gamma_2 + \Gamma_3 + \Gamma_4 + 2\Gamma_5$
D^1	$\Gamma_2 + \Gamma_5$	$D^{9/2}$	$3\Gamma_6 + 2\Gamma_7$
$D^{3/2}$	$\Gamma_6 + \Gamma_7$	D^5	$\Gamma_1 + 2\Gamma_2 + \Gamma_3 + \Gamma_4 + 3\Gamma_5$
D^2	$\Gamma_1 + \Gamma_3 + \Gamma_4 + \Gamma_5$	$D^{11/2}$	$3\Gamma_6 + 3\Gamma_7$
$D^{5/2}$	$\Gamma_6 + 2\Gamma_7$	D^6	$2\Gamma_1 + \Gamma_2 + 2\Gamma_3 + 2\Gamma_4 + 3\Gamma_5$
D^3	$\Gamma_2 + \Gamma_3 + \Gamma_4 + 2\Gamma_5$	$D^{13/2}$	$3\Gamma_6 + 4\Gamma_7$

This decomposition can be applied by the analysing the splitting of the energy levels of rare earth ion in different crystal fields. If the crystal field influence is neglected then the energy levels of the rare earth ions are those of the free ion levels characterized by their *J* values. The crystal field reduces the symmetry dependent on the structure of the complex (here D_4). Free ion eigenstates are the basis functions for a representation of the given point or double group. The free ion levels, which are (2*J*+1) degenerated, split into several levels. The number of these levels is given by the number of the irreducible representations of the considered group into which *J* decomposes (see table 4.5). This description of the split terms does not give the magnitude of the splitting or say which level is higher than another one [76].
As example we consider here praseodymium in D_4 symmetry. The ground state is $^3H_4$, so that it splits into nine states (but seven different energy states) due to the (2*J*+1) degeneracy. By comparison with table 4.2 the following sum of the irreducible representations belongs to these nine states: $2\Gamma_1 + \Gamma_2 + \Gamma_3 + \Gamma_4 + 2\Gamma_5$, whereby the representation Γ_5 is two-fold degenerated, so that the sum is nine.

4.1.3 Implementation

For realization of the symmetry analysis the right point or double group must be given in the input. In BonnMag this is specified with a keyword SYML followed by the number of the point group in the RUN input data. The symmetry analysis is performed by the subroutine *symmetry*. The following coding describes all 32 crystal point groups given with Schoenflies or Hermann-Manguin symbols [77]

1 C_1 (1)	9 C_4 (4)	17 C_{3i} / S_6 ($\bar{3}$)	25 C_{6v} (6*mm*)
2 C_i ($\bar{1}$)	10 S_4 ($\bar{4}$)	18 D_3 (32)	26 D_{3h} ($\bar{6}m2$)
3 C_2 (2)	11 C_{4h} (4/*m*)	19 C_{3v} (3*m*)	27 D_{6h} (6/*m2/m2/m*)
4 C_s (*m*)	12 D_4 (422)	20 D_{3d} ($\bar{3}2/m$)	28 T (23)
5 C_{2h} (2/*m*)	13 C_{4v} (4*mm*)	21 C_6 (6)	29 T_h (2/m$\bar{3}$)
6 D_2 (222)	14 D_{2d} ($\bar{4}2m$)	22 C_{3h} ($\bar{6}$)	30 O (432)
7 C_{2v} (*mm*2)	15 D_{4h} (4/*mmm*)	23 C_{6h} (6/*m*)	31 T_d ($\bar{4}3m$)
8 D_{2h} (2/*m2/m2/m*)	16 C_3 (3)	24 D_6 (622)	32 O_h (4/m$\bar{3}$2/*m*)

Except for T_d, *O* and *T* each group is programmed as a DATA block as follows

POINT GROUP 4: $\boldsymbol{C_s}$

```
DATA CHARACTER(4, -20:20, 1)/ 'G1','G3','G2','G4','G1','G3',
                              'G2','G4','G1','G3','G2','G4','G1','G3','G2','G4','G1','G3',
                              'G2','G4','G1','G3','G2','G4','G1','G3','G2','G4','G1','G3',
                              'G2','G4','G1','G3','G2','G4','G1','G3','G2','G4','G1'/
```

The first integer in the brackets is the point group number. Then the interval from $-2M_j$ to $2M_j$ is given. The last integer is the global number of data blocks. For each group this number could be maximally 4. Since each group can be represented by up to four data blocks. Following the process described in section 4.1.1 each M_j quantum number is assigned an irreducible representation allocated by the data block.

The next step is the analysis of the eigenvectors. At first the largest component in the eigenvector is identified. After the determination of corresponding M_j quantum number the irreducible representation can be matched due to the data block of the considered point group. In case of symmetry groups where the explicit assignment of the irreducible representations to the M_j values based on the rotation is possible all data blocks are equal. Wherever this is not the case the data blocks are different. These differ from each other in the irreducible representations which correspond to the same M_j quantum number under the selected symmetry operation. In this case the signs of eigenvalues for M_j and $-M_j$ are compared and the obtained sign combination is analysed (see paragraph 4.1).

This process works for all symmetry groups except T_d, O, T and all groups that include the horizontal mirror plane σ_h or inversion i. These groups have no data blocks with a set of M_j quantum numbers and corresponding irreducible representations. In this case the match of the representations is directly obtained by analysis of the vector components and the degeneracy of the energy states. At first the eigenvectors of degenerated states are summed and then this sum is analysed. For example if all non-zero values in the sum eigenvector correspond to odd M_j quantum numbers and $M_j = 4$, Γ_4 is the irreducible representation of the point groups O and T_d. The non-degenerated eigenvectors can be clearly differentiated by their vector components.

The symmetry analysis implemented in BonnMag assigns irreducible representations to each transition. In case of mixed states only the largest contribution is analysed and dependent on the corresponding M_j values the irreducible representation is obtained by the symmetry analysis.

If the input setting of the point group is incorrect so that no irreducible representation can be matched to the eigenvectors an error message is given, so that the point group should be corrected.

The obtained irreducible representations can be checked by the reducible representations described in paragraph 4.1.2. All D^J representations decompose into the sum of irreducible representations. These theoretical sum has to be equal with the sum of obtained irreducible representations.

4.2 Calculation of the moment of inertia tensor

4.2.1 Theoretical Background

The calculation of the moment of inertia tensor is necessary for for performing of the symmetry analysis. For a symmetry analysis the global *z*-axis of the chomophore (given by the command XREF) has to be parallel to the standard rotation axis of the given point group. Otherwise calculated eigenvector components could not be given correctly so that the symmetry analysis can not be performed. Therefore by calculating the moment of inertia tensor it is checked whether the calculated *z*-axis corresponds to the given one.

$\vec{I} = m\vec{r}$ (m: mass, $\vec{r}$: radius) Equation 4.7

The moment of inertia tensor is symmetric [78, 79]. The eigenvalues of the eigenvectors are compared to each other using the definition of the symmetrical with at least two identical moments of inertia ($I_1 = I_2$) and asymmetrical gyro with three different moments. Three different possibilities for the symmetrical gyro are implemented in BonnMag. The completely symmetrical gyro is defined by three identical moments of inertia ($I_1 = I_2 = I_3$). For the extended (prolate) gyro the condition is $I_1 = I_2 > I_3$ and for the oblate gyro $I_1 = I_2 < I_3$.

4.2.2 Implementation

Within the framework of subroutine TINERT the inertia tensor of the given chromophore is calculated. This part is activated if symmetry analysis is requested and the keyword SYML is present in the input RUN. In this case the subroutine TINERT reads the atomic coordinates and symbols given in SETUP. The element symbols must be given for the chromophore because they are read by TINERT and assigned to the corresponding atomic masses. Dummy atoms (if requiered) must be labeled as X. With this input data the inertia tensor of the

investigated system can be calculated. The calculated axes will be compared to the axes given in the input file SETUP. If both axes sets are identical th DIRPRO(12,1,1:7,1)=(/1,2,3,4,5,6,7/) calculation continues. Otherwise the input axes should be corrected. The error report contains the correct direction of the global *z*-axis. The subroutine TINERT uses different gyro variations for the check of the axes. The four conditions (see below) are checked by TINERT to find the right global *z*-axis.

4.3 Selection rules

4.3.1 Theoretical Background

For the determination of the allowed and forbidden transitions the analysis of the magnetic and electric dipole mechanisms is required. For the first order magnetic dipole transitions the seletion rules are: $\Delta J = 0, \pm 1$ ($0 \leftrightarrow 0$ is forbidden), $\Delta M_J = 0, \pm 1$, $\Delta S = 0$, $\Delta L = 0$, and no parity change. For the electric dipole mechanism the selection rules are similar, except $\Delta L = 0, \pm 1$ and parity change. BonnMag contains the analysis of the electric dipole transitions.

The direct product provides a way of extending the number of basis functions in a group. It is used in several contexts, for example in case of coupling of degrees of freedom of a spin-orbit interaction. In those cases the direct product is required to determine the appropriate irreducibe representations of the resulting eigenstates. In our case direct products can be applied to selection rules.

By considering the transformation properties of a product of two eigenfunctions the notation of a direct product can be applied in quantum mechanics. If two eigenfunctions φ_i and $\varphi_{i'}$ of a Hamiltonian H are given and H is invariant under symmetry operations the following is obtained for the action of these operations on the eigenfunctions (A = transformation matrix of R)

$$R\varphi_i = \sum_{j=1}^{l} \varphi_j A_{ji}(R) \qquad \text{Equation 4.20a}$$

$$R\varphi_{i'} = \sum_{j'=1}^{l'} \varphi_{j'} A_{j'i'}(R) \qquad \text{Equation 4.20b}$$

By considering the transformation properties of φ_i and $\varphi_{i'}$ it is observed that

$$R(\varphi_i \varphi_{i'}) = R(\varphi_i) R(\varphi_{i'}) \qquad \text{Equation 4.21}$$

So $\varphi_i \cdot \varphi_{i'}$ transforms as a direct product of the irreducible representations associated with φ_i and $\varphi_{i'}$.

From the basis principles of group theory it follows that the matrix element $(i \mid H' \mid f) = \int \varphi_i(x)^* H' \varphi_f(x) dx$ vanishes if the irreducible representation $\Gamma^{(i)}$ corresponding to φ_i is not included in the direct product $\Gamma' \cdot \Gamma^{(f)}$.

The determination of selection rules for a direct electromagnetic transition is given by the transformation properties of the dipole vector p = (x, y, z). If the polarizability tensor is involved or two subsequent excitation and de-excitation processes are considered, e.g. in the Judd-Ofelt model, the dipole vector is p = (x^2, y^2, z^2, xy, yz, xz). The matrix elements M_{if} can be written as $M_{if} \sim (i \mid p \mid f) \cdot A$ (A = electromagnetic potential) [80, 81, 82].

4.3.2 Implementation

The transitions are classified as allowed or forbidden following the symmetry analysis. For each point group direct products between all available irreducible representations have been calculated in advance. The results of these products are programmed as DATA blocks as given subsequuently for e.g. for point group D_4.

POINT GROUP 12: D_4

```
DIRPRO(12,1,1:7,1)=(/1,2,3,4,5,6,7/)
DIRPRO(12,2,1:7,1)=(/2,1,4,3,5,6,7/)
DIRPRO(12,3,1:7,1)=(/3,4,1,2,5,7,6/)
DIRPRO(12,4,1:7,1)=(/4,3,2,1,5,7,6/)
DIRPRO(12,5,1:7,1)=(/5,5,5,5,1,6,6/)
DIRPRO(12,5,1:7,2)=(/0,0,0,0,2,7,7/)
DIRPRO(12,5,1:7,3)=(/0,0,0,0,3,0,0/)
DIRPRO(12,5,1:7,4)=(/0,0,0,0,4,0,0/)
DIRPRO(12,6,1:7,1)=(/6,6,7,7,6,1,3/)
DIRPRO(12,6,1:7,2)=(/0,0,0,0,7,2,4/)
DIRPRO(12,6,1:7,3)=(/0,0,0,0,0,5,5/)
DIRPRO(12,7,1:7,1)=(/7,7,6,6,6,3,1/)
DIRPRO(12,7,1:7,2)=(/0,0,0,0,7,4,2/)
DIRPRO(12,7,1:7,3)=(/0,0,0,0,0,5,5/)
SELRULE(12,1:7)=(/.FALSE.,.TRUE.,.FALSE.,.FALSE.,.TRUE.,
                 FALSE.,.FALSE./)
```

The DIRPRO (direct product) field has four dimensions. The first is the number of the point group. The second and third is the dimension of the point group. The last integer is used for direct products which produce more then one representation as a result of the multiplication of two irreducible representations. The DIRPRO field contains as a data block results of direct products between all given representations in form of their Bethe indices. All possible direct products from Γ_1 x Γ_1 to Γ_7 x Γ_7 are considered. For the point groups containing a horizontal mirror plane σ_h or inversion *i* the numbering for direct products of two irreducible representations is different from other point groups. In the data field DIRPRO all representations with "+" are given at first by consecutive numbering and subsequent by those with "-".

The logical field SELRULE (selection rule) contains the statement if a transition is dipole allowed or not due to the allocation TRUE or FALSE. The order of these logical contributions is adapted to the given point group. Irreducible representations with x^2, y^2, z^2, xz, yz, xy (see section 4.4 , Judd-Ofelt theory) as basis for the optical transitions in the character tables get TRUE in the logical field SELRULE and others get FALSE. In the output this statement is given for every energy level by the letters "F" or "T". The symmetry analysis can only give a qualitative classification as allowed of forbidden. For the simulation of absorption spectra quantitative values for the oscillator strengths must be provided.

4.4 Additional features implemented in BonnMag

The program BonnMag allows the user to select the amount of particular output ("level"). With the keyword PRTL (print level) in the input SETUP the user can decide which information should be printed in the output data file. Zero is used as a default value in the program. The overview of the output data corresponding to the different print levels is given in table 4.7.

Table 4.7 Print levels and corresponding output data for BonnMag.

Print level	Output content
0	Coordinates of all atoms; distances between each ligand to the metal atom; Slater-Condon-Shortley, spin-orbit and all angular overlap parameters, angular part of the overlap integral, overlap integral, energy levels with electric dipole intensities and *J* projections; symmetry analysis, magnetic and crystal susceptibilities, *g*-tensors (if calculated)
1	Direction cosines for all atoms; crystal field parameters (Wybourne)
2	Nielson-Koster reduced matrix elements; basis set, electrostatic matrices

4.5 Estimation of intensities of *f-f*-transitions according to Judd-Ofelt theory

4.4.1 Theoretical Background

For the detailed ligand field analysis the assignment of the calculated energies to the measured absorption bands more information apart from the energy values is required. From that reason the estimation of the absorption coefficients for *f-f* transitions becomes important. Nevertheless, this analysis should be done with care since the calculation of the oscillator strengths according to Judd-Ofelt theory considers only transitions caused by the electric dipole mechanism.

The oscillator strength *P* corresponding to the electric dipole transition from the ground state *i* of an ion to the excited state *f* is described by the following formula

$$P = \chi\left[8\pi^2 m\nu / h\right] |(i \mid D_2^{(1)} \mid f)|^2 \qquad \text{Equation 4.27}$$

m mass of the electron

h Planck's constant

v frequency of the band

χ term containing the refractive index of the medium in which the ion is embedded.

i ground state

f excited state

D_q can be given in terms of the polar coordinates according to equation 4.28.

$$D_q^{(k)} = \sum_j r_j^k C_q^{(k)}(\theta_j, \varphi_j) \qquad \text{Equation 4.28}$$

with

$$C_q^{(k)}(\theta_j,\varphi_j) = \left[4\pi/(2k+1)\right]^{1/2} Y_{kq}(\theta_j,\varphi_j) \qquad \text{Equation 4.29}$$

where Y_{kq} is a spherical harmonic.

Descriptions of the states *i* and *f* are necessary for the evaluation of the matrix elements used in equation 4.27. Due to the small splittings caused by the crystal field the total angular momentum quantum number *J* remains a good choice. Corresponding to the ground level *i* of the configuration l^N a linear combination exists

$$\left\langle i \right| \equiv \sum_M \left\langle l^N \psi J M \right| a_M \qquad \text{Equation 4.30}$$

where *M* is the quantum number of the projection J_z of *J*. ψ stands for additional quantum numbers, that can be used to define the level uniquely. Using the equation 4.30 the approximation for the excited state can be made

$$\left| f \right\rangle \equiv \sum_{M'} a'_{M'} \left| l^N \psi' J' M' \right\rangle . \qquad \text{Equation 4.31}$$

The states (A| and |A') posses the same parity due to the construction from the same configuration l^N. Under the replacement of r_j by - r_j $D^{(1)}$ leads to -$D^{(1)}$.

$$\left\langle i \right| D_q^{(1)} \left| f \right\rangle = 0 \qquad \text{Equation 4.32}$$

As a consequence the first approximation says, that no direct *f*-*f*' dipole transition occurs, which is given by the Laporte rule. It is necessary to admix into (i| and |f) states from configurations of opposite parity to l^N to obtain nonvanishing matrix elements of $D^{(1)}$. The most important configurations in that case would be configurations of the type $l^{N-1}l'$.

The admixture of configurations of opposite parity is possible if the contribution *V* to the Hamiltonian arising from the interaction of the electrons of the ion with the electric field of the lattice which contains terms of odd parity.

$$V = \sum_{t,p} A_{tp} D_p^{(t)} \qquad \text{Equation 4.33}$$

The states from equations 4.30 and 4.31 are replaced by

$$(B| \equiv \sum_M \left\langle l^N \psi J M \right| a_M + \sum_k \left\langle l^{N-1}(n'l')\psi'' J'' M'' \right| b(n'l', \psi'' J'' M'') \qquad \text{Equation 4.34}$$

and

$$\left| B' \right\rangle \equiv \sum_{M'} a'_{M'} \left| l^N \psi' J' M' \right\rangle + \sum_k \left| b'(n'l', \psi'' J'' M'') \right| l^{N-1}(n'l')\psi'' J'' M'' \right\rangle \qquad \text{Equation 4.35}$$

with

$$b(n'l', \psi'' J'' M'') = \sum_M a_M (l^N \psi J M | V | l^{N-1}(n'l')\psi'' J'' M'') \times$$

$$[\mathrm{E}(\psi J) - \mathrm{E}(n'l', \psi'' J'' M'')]^{-1} \qquad \text{Equation 4.36}$$

and

$$b'(n'l',\psi''J''M'') = \sum_{M'} a_{M'}(l^{N-1}(n'l')\psi''J''M''|V|l^N\psi'J'M')\times$$

$$[\mathrm{E}(\psi'J') - \mathrm{E}(n'l',\psi''J''M'')]^{-1} \quad \text{Equation 4.37}$$

$E(\psi J)$ and $E(\psi'J')$ denote energies of the levels ψJ and $\psi'J'$ of l^N. $E(n'l', \psi''J'')$ corresponds to the energy of the level $\psi''J''$ of $l^{N-1}(n'l')$.

$$(B|D_q^{(1)}|B') =$$

$$\sum a_M a_{M'} A_{tp}\{\left\langle l^N\psi JM|\mathrm{D}_q^{(1)}|l^{N-1}(n'l')\psi''J''M''\right\rangle$$

$$\times\left\langle|l^{N-1}(n'l')\psi''J''M''|\mathrm{D}_p^{(t)}|l^N\psi JM\right\rangle\times[\mathrm{E}(\psi'J') - \mathrm{E}(n'l',\psi''J''M'')]^{-1}$$

$$+\left\langle l^N\psi JM|\mathrm{D}_p^{(t)}|l^{N-1}(n'l')\psi''J''M''\right\rangle$$

$$\times\left\langle|l^{N-1}(n'l')\psi''J''M''|\mathrm{D}_q^{(1)}|l^N\psi JM\right\rangle\times[\mathrm{E}(\psi J) - \mathrm{E}(n'l',\psi''J''M'')]^{-1}\}$$

Equation 4.38

This sum is running over M, M', t, p and quantum numbers n, l.

Some approximations must be introduced to simplify equation 4.38. The first approximation is that the splittings within the multiplets of the excited states are assumed to be rather small and negligible. E(n'l', ψ"J") is then independent of J". The sums over J" and M" in equation 4.38 can be performed as follows due to the expansion of states of l^N as linear combinations of perfectly Russel-Saunders coupled states

$$\sum_{J'',M''}(l^N\gamma SLJM|D_q^{(1)}|l^{N-1}l'\gamma''SL''J''M'')(l^{N-1}l'\gamma''SL''J''M|D_p^{(t)}|l^N\gamma'SL'J'M')$$

$$=\sum_\lambda(-1)^{p+q+L+L'}(2\lambda+1)\begin{pmatrix}1 & \lambda & t\\ q & -q-p & p\end{pmatrix}\begin{Bmatrix}1 & \lambda & t\\ L' & L'' & L\end{Bmatrix}(l^N\gamma SLJM|T_{p+q}^{(\lambda)}|l^{N-1}\gamma'SL'J'M')$$

Equation 4.39

$\mathrm{T}^{(\lambda)}$ is a tensor with an amplitude

$$(\mathrm{L}\|\mathrm{T}^{(\lambda)}\|\mathrm{L}') = (\mathrm{L}\|\mathrm{D}^{(1)}\|\mathrm{L}'')(\mathrm{L}''\|\mathrm{D}^{(t)}\|\mathrm{L}')\,. \quad \text{Equation 4.40}$$

All matrix elements in equation 4.39 are expressed in terms of reduced matrix elements. At first it is necessary to suppose that $E(n'l', \psi''J'')$ is invariant with respect to ψ" as well as in case of J". In other words all excited configuration $l^{N-1}(n'l')$ are assumed to be degenerated. This approximation leads to the following simplification

$$\sum_{J'',M'',\psi''}\left\langle l^N\psi JM|D_q^{(1)}|l^{N-1}(\mathrm{n'l'})\psi''J''M''\right\rangle\left\langle l^{N-1}(\mathrm{n'l'})\psi''J''M''|D_p^{(t)}|l^N\psi'J'M'\right\rangle$$

$$=\sum_\lambda(-1)^{p+q}(2\lambda+1)\begin{pmatrix}1 & \lambda & t\\ q & -q-p & p\end{pmatrix}\begin{Bmatrix}1 & \lambda & t\\ l' & l'' & l\end{Bmatrix}(nl|\mathrm{r}|n'l')(nl|\mathrm{r}^t|n'l')(l\|C^{(1)}\|l')$$

$$\times(l'\|C^{(t)}\|l)(l^N\psi JM|U_{p+q}^{(\lambda)}|l^N\psi'J'M') \quad \text{Equation 4.41}$$

$U^{(\lambda)}$ is the sum over all electrons of the single-electron tensor $u^{(\lambda)}$ with $(l \| u^{(\lambda)} \| l') = 1$.

$$(nl \| r^k \| n'l') = \int_0^\infty R(nl) r^k R(n'l') dr \qquad \text{Equation 4.42}$$

R/r is the radial part of the single-electron eigenfunction.

The next assumption is that $E(n'l',\psi''J'')$ is invariant with respect to n', and if the full description of the ground state configuration contains no electron with azimuthal quantum number l' then the radial functions $R(n'l')$ for all n' form a complete set as followed

$$\sum_{n'} (nl \| r \| n'l')(nl \| r^t \| n'l') = (nl \| r^{t+1} \| nl) \qquad \text{Equation 4.43}$$

so that the calculation of interconfiguration radial integrals is simplified. Equation 4.41 can be used for simplification of the first product in equation 4.38. A similar procedure is applied for the second product. Due to the following relation

$$\begin{pmatrix} 1 & \lambda & t \\ q & -q-p & p \end{pmatrix} = (-1)^{1+t+\lambda} \begin{pmatrix} t & \lambda & 1 \\ p & -q-p & q \end{pmatrix}$$

the two parts cancel to a large extent if $1+\lambda+t$ is odd. t and λ must be odd, otherwise the right-hand side of equation 4.41 would vanish. The next assumption is that the energy denominators $E(\psi J)$ - $E(n'l',\psi''J'')$ and $E(\psi'J')$ - $E(n'l',\psi''J'')$ are equal.

This approximation is valid if the configurations $l^{N-1}(n'l')$ lie far above the states involved in the optical transitions. Both energy differences can now be replaced by an expression $\Delta(n'l')$, so that equation 4.38 is simplified to

$$(B \| D_q^{(1)} \| B') =$$

$$\sum_{p,t,\lambda} (-1)^{p+q} (2\lambda+1) A_{tp} \begin{pmatrix} 1 & \lambda & t \\ q & -q-p & p \end{pmatrix} (A \| U_{p+q}^{(\lambda)} \| A') \Xi(t,\lambda) \qquad \text{Equation 4.44}$$

with odd λ and

$$\Xi(t,\lambda) = 2 \sum (2l+1)(2l'+1)(-1)^{l+l'} \times \begin{Bmatrix} 1 & \lambda & t \\ l & l' & l \end{Bmatrix} \begin{pmatrix} l & 1 & l' \\ 0 & 0 & 0 \end{pmatrix} \begin{pmatrix} l' & t & l \\ 0 & 0 & 0 \end{pmatrix}$$

$$\times (nl \| r \| n'l')(nl \| r^t \| n'l') / \Delta(n'l') \qquad \text{Equation 4.45}$$

The summation in equation 4.45 runs over all values n' and l' for excited configurations $l^{N-1}(n'l')$. The operator U can be calculated as a normal tensor-operator.

The calculation of the oscillator strength of the transition from <i| to |f> requires the radial integrals and the crystal field parameters A_{tp} so that the resulting matrix elements $(B \| D_q^{(1)} \| B')$ can substitute $(i \| D_q^{(1)} \| f)$ (s. first part of this chapter).

Equation 4.27 is replaced by its rotationally invariant form due to the arbitrary orientation of the rare-earth ions

$$P = \chi\left[8\pi^2 m\nu / 3h(2J+1)\right]\sum|(i|D_2^{(1)}|f)|^2 \qquad \text{Equation 4.46}$$

where the sum runs over *q* and all components i and of the ground and excited state.

Using the equations 4.44 and 4.46 and the statement, that all quantum numbers and suffixes that depend on a fixed direction in space disappear, the following formula is obtained [83, 84, 85, 86].

$$P = \sum_\lambda T_{\lambda\nu}(l^N\psi J \| U^{(\lambda)} \| l^N\psi' J')^2 \qquad \text{Equation 4.47}$$

where λ is even and

$$T_\lambda = \chi\left[8\pi^2 m\nu / 3h\right](2\lambda+1)\times\sum_t (2t+1)B_t\Xi^2(t,\lambda)/(2J+1) \qquad \text{Equation 4.48}$$

$$B_t = \sum_p |A_{tp}|^2/(2t+1)^2. \qquad \text{Equation 4.49}$$

The matrix elements $U^{(\lambda)}$ are the doubly reduced matrix elements of the spherical tensor operators, which have been tabulated by Nielson and Koster [87, 88].

Two new terms are introduced for simplification of equation 4.47.

$$\Omega_\lambda = (2\lambda+1)\times\sum_{t,p}(2t+1)^{-1}|A_{tp}|^2\Xi^2(t,\lambda) \qquad \text{Equation 4.50}$$

and

$$\Omega_\lambda' = (2\lambda+1)\times\sum_{t,p,\eta,\eta'}(2t+1)^{-1}\langle\eta|Q_i|\eta'\rangle^2\times\rho(\eta)\left|\frac{\partial A_{tp}}{\partial Q_i}\right|^2\Xi^2(t,\lambda) \qquad \text{Equation 4.51}$$

The A_{tp} with odd values for t are the odd-parity terms in the static crystal field expansion. Q_i denotes the normal coordinate of the complex, η and η' represent the vibrational quantum numbers of the initial and final states and $\rho(\eta)$ is the density of states. $\Xi(t,\lambda)$ is defined by equation 4.45.

For interpretation of the experimental data, the following approximation is usually applied. Three parameters $\overline{\Omega}_\lambda$ are called Judd-Ofelt parameters. They can be varied for minimization of the deviations between measured and calculated values of so called transition line-strength *S* given by equation 4.52

$$S = \sum_{\lambda=2,4,6}\overline{\Omega}_\lambda\langle l^N\psi J \| U^{(\lambda)} \| l^N\psi' J'\rangle^2. \qquad \text{Equation 4.52}$$

Intensities are given in terms of the oscillator strength or *P* number as given below, which is dimensionless and is simply related to the line-strength by the following relationship

$$P = \frac{8\pi^2 mc}{3h\bar{\lambda}(2J+1)}\left[\frac{(n^2+2)^2}{9n}\right]S \qquad \text{Equation 4.53}$$

where n is the refractive index of the medium, $\bar{\lambda}$ is the mean wave length of the transition [89, 90].

Due to the assumed excitation mechanism that involves two transitions from the ground state *f* into the virtual state *d* and then to the excited state *f'* the basis that should be used for selection rules is the same polarisability tensor as used e.g. for Raman transitions.

4.4.2 Implementation

The eigenvectors and the orbital-unit tensor operator $U^{(\lambda)}$ are used for the calculation of the intensities of the electric dipole transitions. The elements of $U^{(\lambda)}$ are already present in the program because these matrices are used for the calculation of the energy levels. At first the subroutine MPROG calculates the integrals $\left\langle l^N \psi J \| U^{(\lambda)} \| l^N \psi' J' \right\rangle^2$ for λ = 2 ,4 and 6. The coefficients from the eigenvector of the ground state are multiplied with the matrix $U^{(\lambda)}$ and coefficients from the eigenvector of the excited state.

$$\left\langle l^N \psi J \| U^{(\lambda)} \| l^N \psi' J' \right\rangle = \left\langle \Psi_i \| U^{(\lambda)} \| \Psi_j \right\rangle = \left\langle c_i \varphi_i \| U^{(\lambda)} \| c_j \varphi_j \right\rangle = \sum_i \sum_j c_i c_j \left\langle \varphi_i | U^{(\lambda)} | \varphi_j \right\rangle$$

Equation 4.54

After squaring of the integrals the three results for λ =2 ,4 and 6 are summed and multiplied with Judd-Ofelt parameters to obtain line strength. BonnMag contains Judd-Ofelt parameters for all three-valent rare-earth ions doped into LaF_3 (Table 4.8) as default values. These values are used for the calculation of line strengths, if no parameters are given in the input RUN. Due to the given number of *f* electrons the subroutine MPROG determines which rare-earth ion is given and uses Judd-Ofelt parameters from the internal data block. If other parameters should be used for these calculations they have to be given in RUN and introduced by the keyword JOPS (Judd-Ofelt parameters).

Oscillator strengths are calculated according to equation 4.53 from the line strengths, *J* values and energies of the states. In the output datafile the oscillator strengths are written in the column after energies. This calculation is independent from the symmetry analysis, so that the oscillator strengths are calculated in any case (see chapter Application) [91, 92, 93].

Table 4.8 Judd-Ofelt parameters for rare-earth ions in LaF_3.

Ion	Ω_2 **(10^{-24} m^2)**	Ω_4 **(10^{-24} m^2)**	Ω_6 **(10^{-24} m^2)**
Ce^{3+}	1.686	3.996	10.61
Pr^{3+}	1.078	2.014	4.529
Nd^{3+}	0.944	1.322	2.486
Pm^{3+}	0.632	1.012	1.910
Sm^{3+}	0.561	0.867	1.580
Eu^{3+}	0.444	0.651	1.119
Gd^{3+}	0.346	0.480	0.774
Tb^{3+}	0.660	1.020	1.865
Dy^{3+}	0.477	0.686	1.159
Ho^{3+}	0.387	0.530	0.846
Er^{3+}	0.375	0.506	0.798
Tm^{3+}	0.368	0.493	0.771
Yb^{3+}	0.309	0.397	0.587

Examples for the application of BonnMag

In this chapter applications for BonnMag are introduced. The potential and limitations of the program BonnMag are shown by analysing the ligand-field influences of different rare-earth compounds. The quality of BonnMag compared to the ab initio methods was checked by calculations of the excited state energies of free Ln^{3+} ions and ligand-field splitting for the $[Ln^{III}Cl_6]$ chromophores in elpasolites $Cs_2NaLnCl_6$. Then it was possible to fit the UV/vis/NIR spectra and magnetical moments (effective Bohr magneton number) of $Nd_2Hf_2O_7$. The europium-oxygen interaction in nine different europium(III) oxo-compounds (including *C*-type Eu_2O_3) has been investigated on the basis of powder reflectance spectra (NIR/vis/UV) and temperature dependent magnetic measurements. As least the good transferability of AOM parameters as well as influence of all parameters on excited state energies, ligand-field splitting and magnetic moments was investigated for U^{4+} in UPO_4Cl, UP_2O_7, and $(U_2O)(PO_4)_2$.

5 Calculation of the excited state energies of free Ln^{3+} ions using BonnMag and ab intio methodes

For the comparison between *ab initio* methods and BonnMag the energies for the free Ln^{3+} ions were calculated. Using the program ORCA (Version 4.0) [94] the excited state energies for all Ln^{3+} ions were calculated using CASSCF (complete active space self-consistent field) and NEV-PT2 (second-order N-electron perturbation theory) considering all states. The lanthanide atoms were described with the recently developed SARC2-QZVP-DKH basis sets [95] effects, most importantly spin-orbit coupling were taken into account within the Douglas-Kroll-Hess formalism. The active space consisted of all possible configurations of *n* electrons in the 14 f spin orbitals. It has to be noted that similar calculations have been performed before (Ref.96) with an earlier ORCA version. Details of the computational setup can be found therein. The present results differ from those in Ref. 96 because in the present work all configurations were taken into account which improves comparability with the BonnMag results. In the previous ORCA version only high-spin configurations were taken into account except for Tm^{3+}. Slater-Condon-Shortley parameters F_2, F_4, F_6 were extracted from the obtained energies from both methods. The spin-orbit coupling constant ζ was obtained by a fit to the CASSCF excitation energies. The parameters fitted to the present CASSCF and NEV-PT2 calculations as well as values reported in literature for several free

trivalent lanthanide ions (Ce and Yb [96], Pr [97], Eu [98], Pm and Ho [99]) are composed in Table 5.1. Parameters from NEV-PT2 are rather similar to those obtained from the experiment, whereas the CASSCF values for F_2, F_4, F_6 are much larger and show larger deviations from experimental data compared to NEV-PT2. Using NEV-PT2 the energy states of all free Ln^{3+} ions can be calculated in rather good approximation.

For comparison of ab initio methods and calculations within the framework of computer program BonnMag F_2, F_4, F_6 and the spin-orbit coupling constant ζ from NEV-PT2 and CASSCF were used.

Table 5.1. Free ion SCS and spin-orbit coupling parameters obtained from NEV-PT2 (F_2, F_4, F_6) and CASSCF (ζ) calculations in cm^{-1} (see text).

Ln^{3+}	F_2	F_4	F_6	ζ	Ln^{3+}	F_2	F_4	F_6	ζ
Ce	0.0	0.0	0.00	685.4	Gd	399.1	58.4	6.52	1576.0
Ce[a)]	0.0	0.0	0.00	643.7	Tb	414.2	59.4	6.69	1761.7
Pr	324.2	52.1	5.25	802.2	Dy	427.6	61.5	6.93	1964.3
Pr[a)]	325.4	51.7	5.23	764.0	Ho	440.8	64.1	7.08	2182.5
Nd	342.7	49.9	5.60	936.2	Ho[a)]	414.6	68.8	7.27	2163.0
Pm	356.6	52.1	5.83	1075.9	Er	454.2	65.7	7.37	2417.5
Pm[a)]	346.2	47.7	5.23	1070.0	Tm	467.4	69.9	7.60	2671.3
Sm	371.8	53.9	6.07	1231.3	Yb	0.0	0.0	0.00	2935.6
Eu	386.1	55.6	6.26	1395.4	Yb[a)]	0.0	0.0	0.00	2918.3
Eu[a)]	401.0	55.4	6.06	1320.0					

a) Experimental data for F_2, F_4, F_6 and ζ from literature for the free Ln^{3+} ions

As expected calculations within the framework of AOM (by BonnMag) using parameters from CASSCF lead to energies, that are indistinguishable from those obtained with CASSCF due to the same assumptions included in BonnMag. This shows foremost that the code of BonnMag is correct. In contrast, the introduction of F_2, F_4, F_6 and ζ from NEV-PT2 into calculations with BonnMag produces energies, which show deviations from the states calculated with NEV-PT2 (Table 5.2, Figure 5.2). These deviations are mainly caused by the dynamical correlation effects included individually for each excited state in NEV-PT2 but only in an effective way in BonnMag by adjusting the Slater-Condon-Shortley (SCS) and spin-orbit coupling parameters.

Excited state energies of the free Ln^{3+} ions calculated with both NEV-PT2 and AOM (with F_2, F_4, F_6 from NEV-PT2 and ζ from NEV-PT2) show a fairly good match with the experimental data. For better comparison of both calculations the mean absolute deviations between NEV-PT2 results and experimental data as well as between BonnMag (with SCS from NEV-PT2) and experiment were calculated for those states where the energies are defined only by ζ (Figure 5.1 left) and for the states mainly resulting from F_2, F_4, F_6 (Figure 5.1 right).

As expected the mean absolute deviation (MAD) for the states defined by spin-orbit coupling is nearly the same for both calculations (Figure 5.1 left). Although the energies of states which are dominated by the Slater-Condon-Shortley parameters F_2, F_4, F_6 were reproduced with acceptable accuracy by BonnMag, in most cases NEV-PT2 leads to slightly better results (Figure 5.1 right). Both methods systematically overestimate the transition energies. The largest absolute deviation is obtained for Gd^{3+}. Here it has to be taken into account that the excitation energies of Gd^{3+} are larger than for the other ions. The relative deviation is, however, comparable. Additionally, BonnMag calculations were performed for Ce^{3+}, Pr^{3+}, Pm^{3+}, Eu^{3+}, Ho^{3+} and Yb^{3+} using F_2, F_4, F_6 and ζ parameters reported in the literature. The results show a slightly better match with the observed transition energies compared to those obtained by application of F_2, F_4, F_6 and ζ from NEV-PT2/CASSCF calculations. Nevertheless, the *ab initio* calculated Slater-Condon-Shortley parameters F_2, F_4, F_6 and spin-orbit coupling constant ζ are well determined by the NEV-PT2 method and can be used as benchmarks, in particular for those systems where no parameters derived from experiment are available.

An even better fit of observed excited state energies is possible with a more elaborate model for the description of the free ions electronic states as it was described for $Cs_2NaLnCl_6$ and Cs_2NaYCl_6: Ln^{3+} containing the $[Ln^{III}Cl_6]$ chromophore [108] At present we refrain from this procedure for two reasons. In particular for low-symmetry chromophores the fitting of a large parameter set (including SCS, ς, E_{ave}, α, β, γ, T^i (i = 2,3,4,6,7,8), M^k (k = 0,2,4), and P^k (k = 2,4,6) is quite challenging. These parameters are defined according to the conventions used in references [134-138]. Reasonably well it can be assumed that the AOM (LF) parameters and the parameters for the free ion are independent of each other.

To obtain an improved fit of the free ion states in BonnMag, the parameters F_2 and ζ from NEV-PT2 calculations were varied, whereby the ratios F_2/F_4 and F_2/F_6 were kept constant as obtained from the NEV-PT2. Table 5.3 shows the re-optimized F_2 and ζ values, as well as calculated energies and MAD for Pr^{3+}, Eu^{3+} and Gd^{3+} from our fitting procedure.

The fitting procedure of F_2 and ζ leads to rather small MAD compared to those using F_2 and ζ from NEV-PT2 (see Table 5.3, Figure 5.1).

If highly accurate fitting of the free ion states is required, the more complex fitting of all four parameters (F_2, F_4, F_6 and ζ) should be considered. For the calculation of the free Ln^{3+} ion excited state energies using BonnMag various degrees of sophistication are currently possible, as the following sequence shows.

- F_2, F_4, F_6 and ζ from NEV-PT2
- Fitting F_2 and ζ
- Fitting all four parameters F_2, F_4, F_6 and ζ
- Taking F_2, F_4, F_6 and ζ from literature (if the reference has fitted these four parameters without the higher order parameters)

Note: Currently a least-squares fitting routine in BonnMag for the SCS is under development.

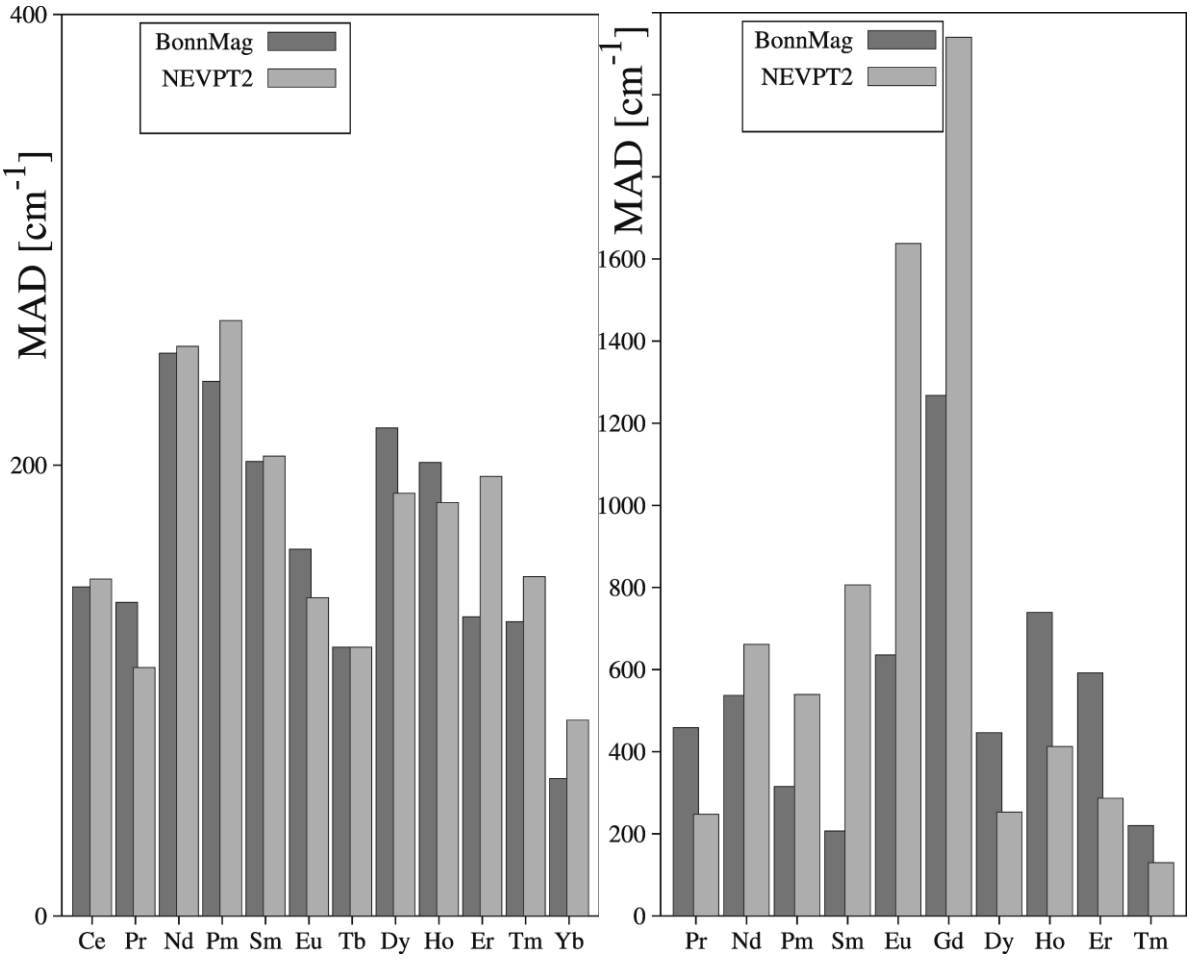

Figure 5.1. Mean absolute deviation Exp./BonnMag and Exp./NEV-PT2 for states resulting from ζ (left) and for the states resulting from F_2, F_4, F_6 (right).

Table 5.2. Comparison between the experimental energies (in cm^{-1}) for the free Ln^{3+} ions and those calculated using BonnMag and NEV-PT2.

Ln^{3+}	$E_{exp.}$ [a]	$E_{BonnMag}$ [b]	$E_{BonnMag}$ [c]	E_{NEVPT2}	Ln^{3+}	$E_{exp.}$ [a]	$E_{BonnMag}$ [b]	$E_{BonnMag}$ [c]	E_{NEVPT2}
Ce	2253.0	2253.0	2399.0	2402.5	Eu	370.0	373.0	400.0	389.9
Pr	2152.1	2132.0	2246.0	2250.8		1040.0	1031.0	1101.0	1079.2
	4389.1	4375.0	4597.0	4603.4		1890.0	1883.0	2003.0	1974.3
	4996.6	5099.0	5112.0	4978.9		2860.0	2861.0	3035.0	3004.7
	6415.2	6516.0	6613.0	6495.7		3910.0	3915.0	4146.0	4120.9
	6854.7	7080.0	7201.0	7103.3		4940.0	5014.0	5301.0	5288.0
	9912.2	10202.0	10471.0	10411.2		17270.0	17505.0	17910.0	18850.3
	17334.4	17950.0	18005.0	17664.2		19030.0	19152.0	19673.0	20643.8
	21389.8	21976.0	21971.0	21463.7		21510.0	21569.0	22133.0	23228.3
	22007.4	22590.0	22627.0	22126.3	Gd	32120		33342.0	34228.9
	22211.5	22009.0	22112.0	22532.5		32720		33960.0	34836.2
	23160.6	23833.0	23955.0	23469.3		33290		34667.0	35484.8
Nd	1880.0		1992.0	1990.4	Tb	2051.6		2093.0	2081.9
	3860.0		4107.0	4107.6		3314.2		3389.0	3399.0
	5910.0		6300.0	6310.1		4292.3		4403.0	4410.2
	11290.0		11727.0	11672.5		4977.9		5121.0	5123.9
	12320.0		12835.0	12759.4		5431.8		5598.0	5595.3
	12470.0		12996.0	13343.1		5653.8		5833.0	5826.5
	13280.0		13717.0	13827.3	Dy	3460.0		3531.0	3514.5
	13370.0		13887.0	13920.1		5780.0		5935.0	5905.6
	14570.0		15257.0	15305.9		8950.0		9299.0	9267.2
	16980.0		16525.0	16918.2		9060.0		9356.0	9169.8
	17100.0		17732.0	17663.5		10100.0		10391.0	10352.6
	18890.0		19636.0	19892.0		10870.0		11342.0	11133.9
	19290.0		20121.0	20240.5		12270.0		12777.0	12574.4
	19440.0		19565.0	20610.4		13060.0		13569.0	13392.6
Pm	1490.0	1586.0	1576.0	1579.4	Ho	5050.0	5087.0	5159.0	5137.6
	3110.0	3305.0	3298.0	3304.8		8550.0	8648.0	8742.0	8714.2
	4820.0	5101.0	5113.0	5158.9		11110.0	11255.0	11348.0	11332.6
	6580.0	6934.0	6983.0	7013.6		13180.0	13350.0	13446.0	13439.3
	12230.0	12292.0	12486.0	12667.6		15370.0	15403.0	16146.0	15692.8
	12670.0	12735.0	12957.0	13340.5		18320.0	18233.0	18876.0	18656.6
	13520.0	13654.0	13860.0	14026.4		18450.0	18480.0	19366.0	18797.5
	14100.0	14373.0	14591.0	14477.0		20510.0	20568.0	21417.0	20882.0
	14470.0	14606.0	14876.0	15059.0		20960.0	21137.0	21793.0	21363.8
	15800.0	15916.0	16262.0	16454.3		21240.0	21317.0	20950.0	21899.0
Sm	1080.0		1099.0	1094.1		22180.0	22366.1	23075.0	22626.5
	2290.0		2384.0	2377.6	Er	6480.0		6612.0	6616.6
	3610.0		3800.0	3797.0		10110.0		10270.0	10334.1
	4990.0		5304.0	5310.1		12350.0		12456.0	12574.2
	6290.0		6352.0	6430.8		15180.0		15595.0	15472.1
	6470.0		6861.0	6881.3		18290.0		18980.0	18446.3
	6540.0		6610.0	6701.9		20400.0		20991.0	20729.8
	7050.0		7135.0	7238.9		22070.0		22731.0	22439.4
	7910.0		8046.0	8147.4		22410.0		23012.0	22696.3
	9080.0		9288.0	9379.2	Tm	5640.0		5668.0	5584.2
	10470.0		10756.0	10836.2		8090.0		8323.0	8335.3
	17860.0		18607.0	19414.9		12500.0		12708.0	12679.0
	18860.0		19208.0	20281.5		14350.0		14516.0	14383.2
	20010.0		20065.0	21593.7		14850.0		15198.0	15008.1
	20560.0		20756.0	21990.4		21320.0		21478.0	21467.7
	20980.0		21056.0	22463.8	Yb	10214.0	10214.0	10275.0	10275.9

a) Some of these experimental energy levels are taken as averages from the ions doped into $LaCl_3$ ignoring ligand field splitting of the multiplets [100].

b) Using F_2, F_4, F_6 and ζ from literature for the free Ln^{3+} ions (Table 5.1, set a)

c) Using F_2, F_4, F_6 and ζ from ab initio calculations for the free Ln^{3+} ions (Table 5.1)

Table 5.3. Parameters used for the calculations of the transitions energies for free *Ln* ions obtained from fitting procedure . F_2, F_4, F_6, ζ, energies and MAD in cm^{-1}.

Ln^{3+}	F_2, F_4, F_6, ζ	$E_{BonnMag}$	*MAD*	Ln^{3+}	F_2, F_4, F_6, ζ	$E_{BonnMag}$	*MAD*
Pr	317.0	2153.0	155.8	Eu	373.0	373.0	32.9
	50.9	4411.0			53.7	1030.0	
	5.13	4987.0			6.04	1880.0	
	770.0	6423.0			1320.0	2854.0	
		6996.0				3907.0	
		10147.0				5006.0	
		17562.0				17360.0	
		21457.0				19011.0	
		22083.0				21421.0	
		21566.0					
		23449.0					
Gd	385.0	32118.0	64.0				
	56.4	32757.0					
	6.28	33443.0					
	1520.0						

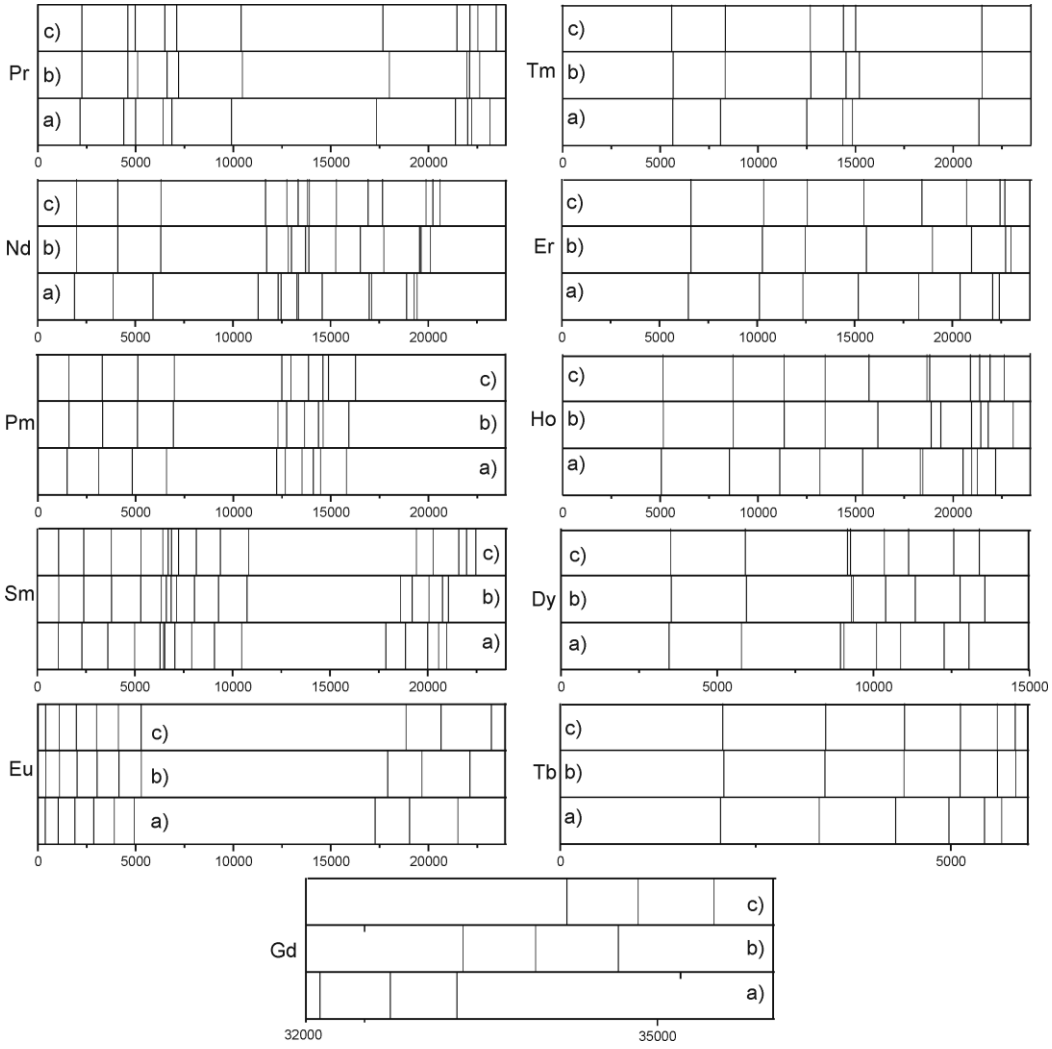

Figure 5.2. Energies of the free Ln^{3+} (Pr-Tm) ions. a) from experiment; b) calculated using BonnMag and F_2, F_4, F_6 and ζ from NEV-PT2; c) energies from NEV-PT2.

6 Calculation of the transition energies and ligand field splitting of $Cs_2NaLnCl_6$

Absorption spectra of elpasolite-type chlorides $Cs_2NaLnCl_6$ (except Pm and Gd) were used as benchmarks to evaluate the quality of the calculations using BonnMag especially for the magnitude of the splitting due to the ligand field.

The Slater-Condon-Shortley parameters F_2, F_4, F_6, the spin-orbit coupling constant ζ as well as AOM parameters e_σ(*Ln*-Cl) and $e_{\pi,iso}$(*Ln*-Cl) obtained by fitting the observed transition energies using the Wybourne parameters [35] were taken from references 101 and 102 for $Cs_2NaLnCl_6$ except for Promethium(III) and Gadolinium(III). The used values are given in Table 6.1. Figure 5.1. Mean absolute deviation Exp./BonnMag and Exp./NEV-PT2 for the states resulting from F_2, F_4, F_6.

Table 6.1. Parameters taken from literature and used in the BonnMag calculations of the transitions energies for *Ln* in $Cs_2NaLnCl_6$. F_2, F_4, F_6 , ζ, e_σ, e_π in cm^{-1}.

Ln^{3+}	F_2	F_4	F_6	ζ	e_σ	e_π	e_π/e_σ
Ce	0	0	0	623	419.0	156.0	0.37
Pr	299.2	45.5	4.4	756	447.4	184.8	0.41
Nd	315.1	48.6	4.8	872	391.1	137.2	0.35
Sm	344.5	51.7	5.5	1167	326.5	100.0	0.31
Eu	372.8	55.1	5.6	1324	384.2	136.4	0.36
Tb	398.1	58.8	5.8	1694	315.3	139.6	0.44
Dy	412.1	60.9	6.3	1920	300.5	138.0	0.46
Ho	420.0	62.9	6.3	2129	325.1	143.2	0.44
Er	431.4	63.8	6.5	2356	292.0	120.0	0.41
Tm	449.4	65.7	7.0	2624	305.3	119.6	0.39
Yb	0	0	0	2897	236.0	114.0	0.48

The AOM parameters e_σ(*Ln*-Cl) from Ref. 44 show no clear trend with atomic number. The ratio e_π/e_σ varies from 0.31 to 0.48 over the whole series of chlorides $Cs_2NaLnCl_6$ The excited state energies as well as the splitting due to the ligand-field were additionally calculated using the parameters F_2, F_4, F_6 and ζ obtained from NEV-PT2/CASSCF and e_σ(*Ln*-Cl) derived by a fitting procedure with respect to the nearly pure *J* states with the ratio e_π/e_σ = 1/3 (Table 5.1 and A6). which is in the range of literature values shown in Table 4. The derived AOM parameters e_σ are comparable to those from literature. The parameter e_σ(*Ln*-Cl) derived by our fitting procedure decreases with atomic number except Eu^{3+} and Tm^{3+}. Figure 6.1 shows the correlation between e_σ(*Ln*-Cl) and ionic radii of Ln^{3+}. The comparison of the excited-state energies calculated with BonnMag (lit: using F_2, F_4, F_6, ζ, e_σ(*Ln*-Cl), and e_π(*Ln*-Cl) from Ref.

[108]; fit1: using F_2, F_4, F_6, ζ, from NEV-PT2/CASSCF and fit value for e_σ(*Ln*-Cl), e_π/e_σ = 1/3; fit2: using F_2 and ζ given in Table 5.3 and fit the value for e_σ(*Ln*-Cl), e_π/e_σ = 1/3) and experimental energies (exp.) as well as splittings due to the ligand field are given in Figure 6.2. Since the free ion parameters F_2, F_4, F_6, ζ are overestimated by NEV-PT2/CASSCF the energies of the free Ln^{3+} ions can be better reproduced using the parameters from Table 5.3.

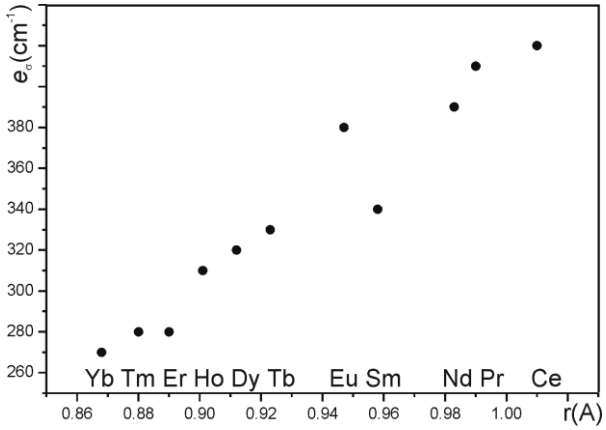

Figure 6.1. e_σ(*Ln*-Cl) obtained from the fitting procedure vs. ionic radii of Ln^{3+}.

The calculated transition energies show good match with the experimental data for both parameter sets, so that the AOM parameters are reasonable (Figure 6.1a). As already discussed, the simple parametrization of the free ion using only four parameters F_2, F_4, F_6 and ζ (compared to the parametrization reported in Ref. 44) leads to larger deviations of the free ion states. Since our investigation focused on the ligand-field effects and not on the perfect match of the free ion energies only F_2, F_4, F_6 and ζ are used for the parametrization of the free ion states to keep the model as simple as possible. Considering the higher order parameters [108] for the free ion would lead to a very difficult parametrization procedure. The calculated ligand field splittings are in good agreement with the observed values, which are empharized in Figure 6.1b for one selected transition for each Ln^{3+} ion. Thus, e_σ(*Ln*-Cl) and $e_{\pi,iso}$(*Ln*-Cl) used in these calculations describe rather well the magnitude of the ligand field influence. The parameters F_2, F_4, F_6 and ζ obtained from NEV-PT2 as well as the fitting procedure of e_σ(*Ln*-*L*) can be applied by considering new systems.

The proper description of the ligand-field splitting of the ground state is crucial for the calculation of the magnetic susceptibilities and the temperature dependency of the magnetic moments. Furthermore, the splitting of the excited states can be used to study the chemical bonding between the rare earth elements and the ligands in different compounds.

In Reference 103 the e_σ(*Ln*-Cl) and $e_{\pi,iso}$(*Ln*-Cl) values for the whole series of $Cs_2NaLnCl_6$ (except Pm and Gd) are reported using AILFT [104]. These values are significantly lower

than the parameters obtained by fitting the absorption spectra. The ligand field splittings calculated with parameters obtained from AILFT are smaller than the observed ones. This indicates that an extension of the active space in ab initio calculations is necessary for a better description of the ligand field influence.

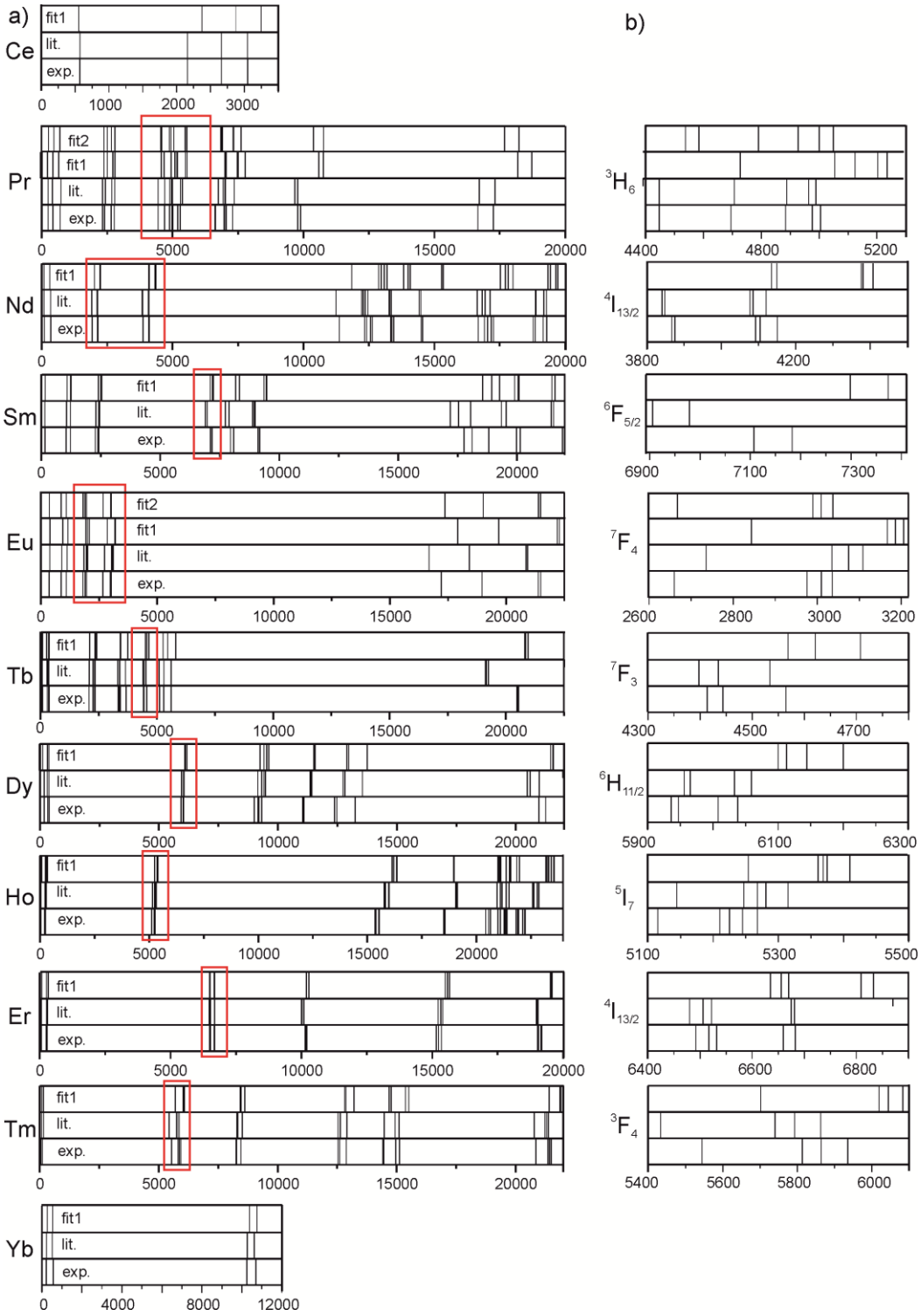

Figure 6.2. Calculated and experimental transition energies for $[Ln^{III}Cl_6]$ in $Cs_2NaLnCl_6$. Calculated energies obtained using F_2, F_4, F_6, ζ and e_σ(*Ln*-Cl) from literature (lit.) vs. F_2, F_4, F_6, ζ from NEV-PT2 with fitted e_σ(*Ln*-Cl) (fit). a) excited state energies in IR/vis range, b) splitting pattern for the various excited states to visualize the ligand field effect.

7 Neodymium hafnate $Nd_2Hf_2O_7$

$Nd_2Hf_2O_7$ was chosen as a test system due to the simple electronic configuration of the metal ion (Nd^{3+}: f^3) and rather high symmetry of the chromophore.

Pyrochlores are compounds with the general sum formula $A_2B_2O_7$. Ideally it crystallizes in the cubic space group $Fd\bar{3}m$. The pyrochlore structure is related to the fluorite structure [105] with oxygen deficiency. Compounds of the pyrochlore family show disordering effects on the metal as well as on oxygen sites. In fluorite the oxide ions fully occupy the tetrahedral interstices between the cations. In contrast only 87.5 % of the available oxide sites are occupied in the pyrochlore structure. The cation sites A and B have 3*m* symmetry whereas the cation site in fluorite has *m*3*m* symmetry [106].

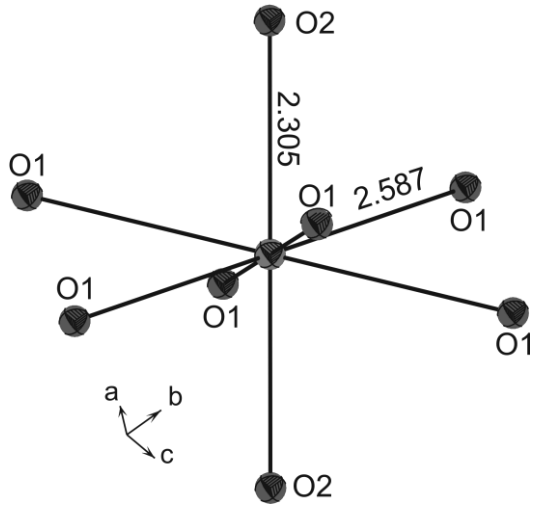

Figure 7.1. ORTEP style representation of [NdO_8] polyhedra in $Nd_2Hf_2O_7$.

Single crystals of $Nd_2Hf_2O_7$ were synthesized [107] and UV/vis spectra (University of Bonn) as well as magnetic susceptibilities (MPI Stuttgart) were measured. Using programm BonnMag transition energies, magnetic susceptibilities and moments were calculated and compared to the experimental data. Due to the missing interelectronic repulsion parameters for the free Nd^{3+} ion the values reported for the neodymium elpasolite with the formula $Cs_2NaNdCl_6$ [108] were used. Slater- Condon-Shortley parameters F_2, F_4, F_6 and spin-orbit coupling constant ζ are given in Table 7.1. The AOM parameters e_σ(Nd-O) and $e_{\pi,iso}$(Nd-O), for a given distance d(Nd-O) were obtained by matching the calculated magnetic susceptibilities and excited state energies against the observed data. The $e_{\pi,iso}$ were taken as one third of the corresponding e_σ. The different distances d(Nd-O) in $Nd_2Hf_2O_7$ were

accounted for by relation (9.1). This procedure leads to $e_{\sigma,norm}$(Nd-O) = 560 cm^{-1} for d(Nd-O) = 2.3 Å. Judd-Ofelt parameters were transfered from Nd^{3+} doped in $LaCl_3$ [90].

Table 7.1. "Best-fit parameters" [a] for the angular overlap modeling of the $[Nd^{III}O_8]$ chromophore in $Nd_2Hf_2O_7$.

Slater-Condon-Shortley parameters (cm^{-1})				
F_2 = 315.1	F_4 = 48.6	F_6 = 4.807		
Spin-orbit coupling constant (cm^{-1})				
ζ = 872				
Stevens-orbital reduction factor [29]				
k = 0.965				
Interaction parameters e_m(Nd-O), (m: σ, π)				
Ligand	**Distance (Å)**	**e_σ (cm^{-1})**	**$e_{\pi,iso}$ (cm^{-1})**	**e_π / e_σ**
O1	2.305	551.5	183.8	0.33
O2	2.587	245.9	61.3	0.33
Judd-Ofelt parameters (10^{-24} m^2) [90]				
Ω_2 = 0.944	Ω_4 = 1.322	Ω_6 = 2.486		

a) From visual comparison of observed and calculated transition energies, line strengths, and the dependence of magnetic moment on temperature.

The comparison of the calculated and experimental data are shown in Figure 7.2 and 7.3. Using parameters given below calculations of transition energies and magnetic moments lead to the rather good match between the experiment and modelling. It also shows good agreement between observed and calculated line strengths using Judd-Ofelt parameters from literature. At first the ratio e_π/e_σ was set to 0.25 and led to the worse fit of the magnetic moments as shown in Figure 7.3 especially for the low temperature range till 50 K. Increase of this value up to 0.33 provides better match between calculated and measured magnetic moments. Stevens-orbital reduction factor k is 0.965 for the "best fit" calculation. The nephelauxetic ratio β can not be determined, because the Slater-Condon-Shortley parameters reported in literature are for Nd^{3+} in $Cs_2NaNdCl_6$ and not for the free ion.

The ground state $^4I_{9/2}$ splits ligand-field for the $[Nd^{III}O_8]$ chromophore in five double degenerated states (2J+1 rule): 0 cm^{-1}, 158 cm^{-1}, 221 cm^{-1}, 242 cm^{-1}, and 574 cm^{-1}.

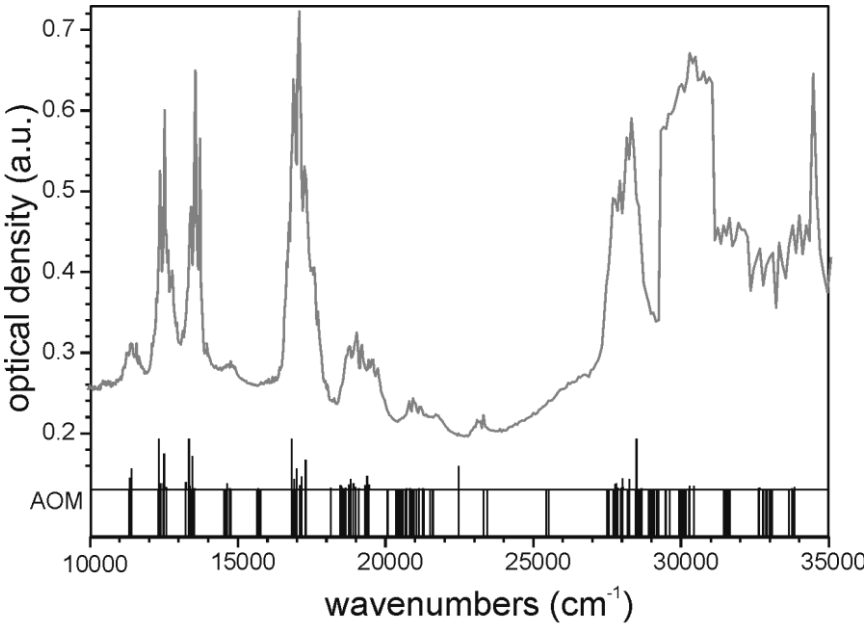

Figure 7.2. Single-crystal UV/vis spectrum of $Nd_2Hf_2O_7$. Results from AOM (zero-phonon lines) with estimated intensities (Judd-Ofelt theory).

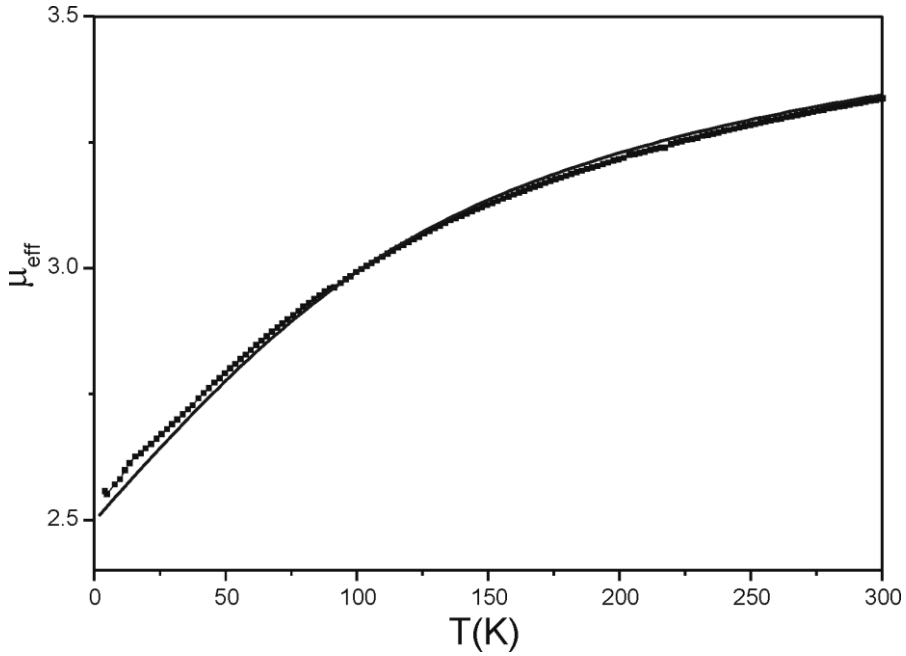

Figure 7.3. Graphical representation of the measured effective Bohr magneton number μ_{eff}/μ_B vs. T (K) for $Nd_2Hf_2O_7$ and comparison to the calculated μ_{eff} (solid line) [107].

8 Europium(III) compounds

Computation of the transition energies and of the effective Bohr magneton numbers for Eu^{3+} in the different ligand fields is performed within the framework of AOM. These calculations show that all electronic transition energies in the optical spectra, the magnetic susceptibilities as well as their temperature dependence are very well accounted for by AOM.

The electronic structure of Eu^{3+} (f^6 system) is somewhat special in the series of RE^{3+} cations since the ground state $^7F_0$ is "unmagnetic" ($\mu_{eff}/\mu_B = 0$) despite the six unpaired electrons. This behavior follows from strong spin-orbit coupling and is described by the Landé formula [109, 110]. Experimentally, μ_{eff}/μ_B = 3.4 to 3.6 is observed at room temperature with a strong decrease to $\mu_{eff}/\mu_B \approx 0.3$ upon cooling to 2 K [111]. In principle this temperature dependence can be understood by thermal population at $T > 0$ K of the first excited electronic state $^7F_1$ with $\mu_{eff}/\mu_B = 4.24$. The energy difference between the "unmagnetic" ground state and the first excited state is reduced due to the splitting of the $^7F_1$ state by the ligand-field (Figure 8.1). Splitting between $^7F_0$ and $^7F_1$ in the free ion is $\Delta\tilde{\nu} \sim 370$ cm^{-1} and is a function of the spin-orbit-coupling constant. The $^7F_1$ state splits due to the ligand field in three states, with a separation between the highest and the lowest state of $\Delta\tilde{\nu} \sim 80$ cm^{-1}. Thus, the magnetic moment of europium(III) compounds at room temperature can qualitatively correlated to the ligand-field splitting of the $^7F_1$ state. Higher splitting leads to lowering of one or two $^7F_1$ split state and therefore to a higher thermal population and a higher magnetic moment. For the free Eu^{3+} ion (no LF!) one would obtain for room temperature $\mu_{calc}/\mu_B \approx 3.20$.

The optical properties of Eu^{3+} ions in various types of compounds and host lattices have been reviewed only recently by BINNEMANS [112].

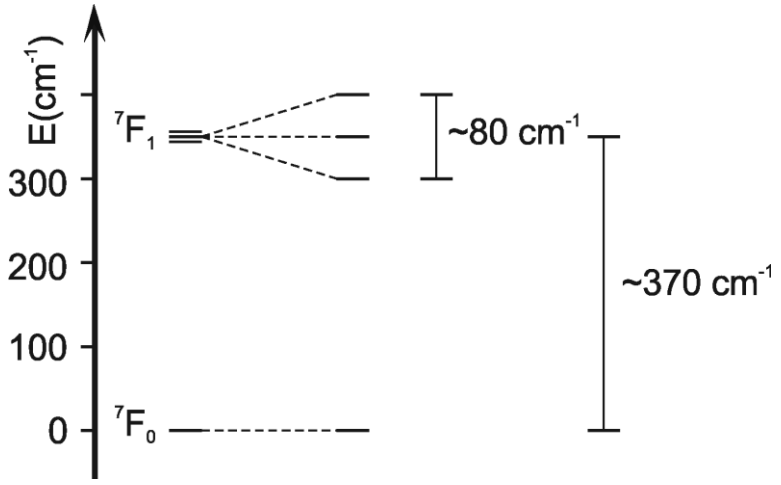

Figure 8.1. Splitting of the ^7F state by spin-orbit coupling and ligand-field. μ_{eff}/μ_B ($^7F_0$) = 0, μ_{eff}/μ_B ($^7F_1$) = 4.24. The higher states $^7F_2$ to $^7F_6$ are omitted.

A quantitative description of the temperature dependence of $\mu_{eff}(Eu^{3+})$ requires obviously a thorough description of the ligand-field splitting of the $^7F_1$ state. BonnMag allows description of the ligand-field effects on Eu^{3+} (f^n) within the AOM framework. The lack of such a program prevented for a long time detailed ligand-field analysis for the more complicated f^n electronic systems (Sm^{3+} and Eu^{3+}) despite a considerable amount of experimental data (see for example references on Eu*X*O_4 (*X*: P, As, Sb, V) [111], Eu_2O_3 [113, 114], EuOCl [115], EuP [116].

In this thesis results of temperature dependent magnetic measurements for nine europium(III) oxo-compounds (see Table 8.1) are reported. In addition, powder reflectance UV/vis/NIR spectra for these compounds have been recorded [117]. To provide detailed experimental evidence for the prevailing ligand-field splittings, the electronic excitation $^7F_0 \rightarrow {}^5D_2$ has been measured with high resolution in the powder reflectance spectra. By matching the AOM calculations to the experimental data, eventually AOM parameters $e_\sigma(Eu^{3+}\text{-}O^{2-})$ are obtained for the first time that allow rationalization of the ligand-field splitting within a chemically meaningful model.

Table 8.1. Europium(III) oxo-compounds investigated in this paper with the chromophores used for the AOM calculations.

Compound	Space group	Chromophore [a)]	Point group	Ref.
$EuPO_4$	$P2_1/n$	$[EuO_9]$	C_1	118
$EuAsO_4$	$I4_1/amd$	$[EuO_8]$	D_{2d}	119
$EuVO_4$	$I4_1/amd$	$[EuO_8]$	D_{2d}	120
EuOCl	$P4/nmm$	$[EuO_4Cl_5]$	C_{4v}	121
$EuNbO_4$	$I2/a$	$[EuO_8]$	C_2	122
$EuTaO_4$	$I2/a$	$[EuO_8]$	C_2	122
$Eu_2Ti_2O_7$	$Fd\bar{3}m$	$[EuO_8]$	D_{3d}	123
$EuSbO_4$	$P2_1/c$	$[EuO_8]$	C_1	124
Eu_2O_3 [b)]	$Ia\bar{3}$	$[Eu1O_6]$ $[Eu2O_6]$	S_6 C_2	125

a) All ligands closer to Eu^{3+} than the next cation have been included.
b) *C*-Type

The energies of the free ion electronic states are introduced into the AOM calculations via the Slater-Condon-Shortley parameters F_2, F_4, F_6, [30] and the spin-orbit coupling constant ζ [40]. Throughout this thesis for the free Eu^{3+} ion F_2 = 401 cm^{-1}, F_4 = 55.38 cm^{-1}, F_6 = 6.06 cm^{-1}, and the spin-orbit-coupling constant ζ = 1320 cm^{-1} have been assumed according to literature [126]. These numbers were not reduced (nephelauxetic ratio β = 1.0) and the Stevens orbital reduction factor [29] k = 1.0 was maintained in all calculations. Extensive adjustment could lead to a better fit of the transition energies and magnetic moments. Nevertheless, description of the free ion with a large number of parameters was avoided in our modelling, to keep the parametrization as simple as possible.

AOM parameters are assumed to depend on the metal-ligand distances (eq. 9.1) [26]. Furthermore, throughout this thesis isotropic π-interactions ($e_{\pi,x} = e_{\pi,y}$) with $e_{\pi,iso}$ = ¼ e_σ have been assumed. In effect, these assumptions leave just one parameter, e. g. $e_{\sigma,max}$(Eu-O) of the nearest ligand in each chromophore, for matching calculated against observed transition energies and magnetic susceptibilities.

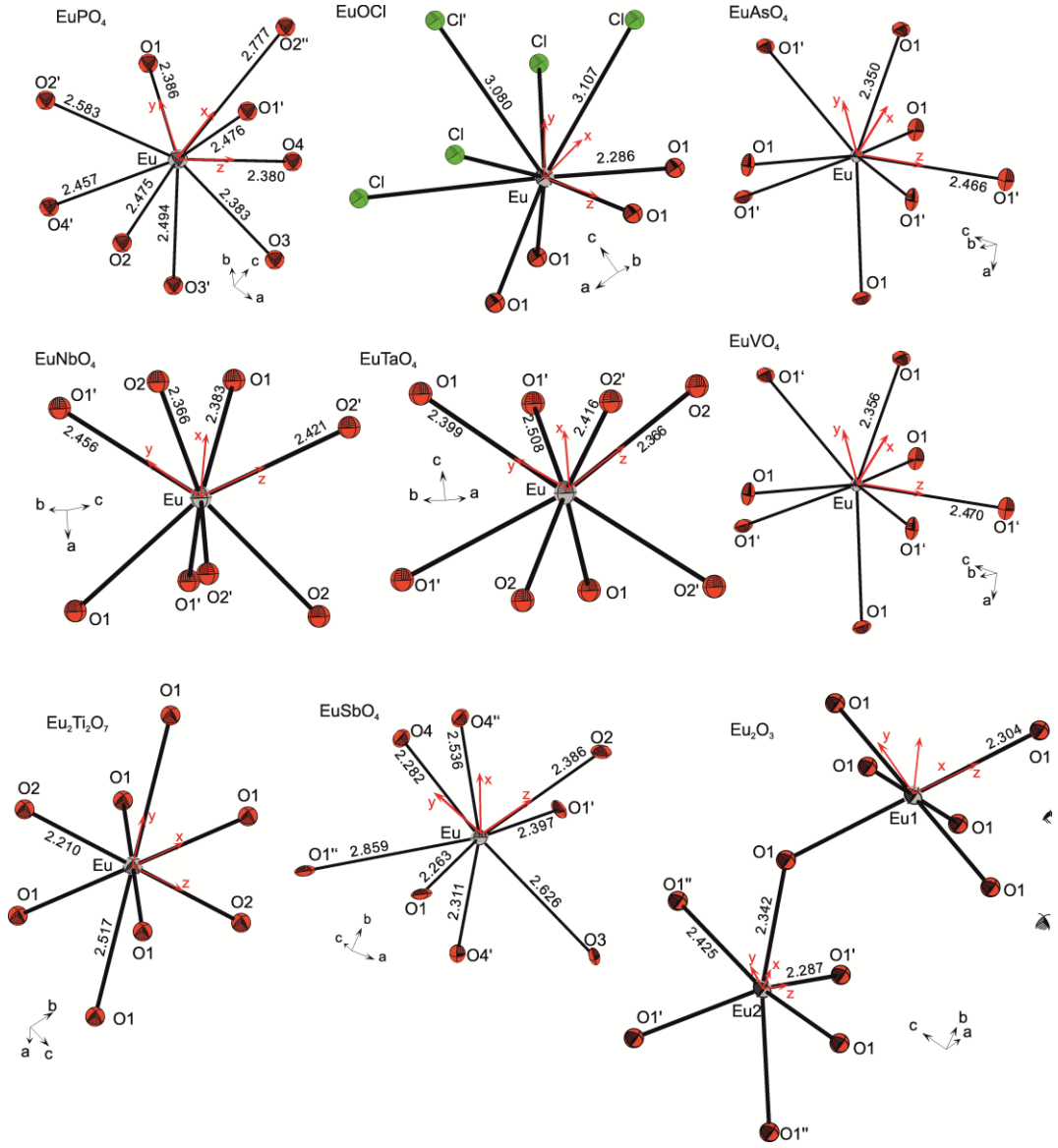

Figure 8.2. ORTEP representation of the chromophores [$Eu^{III}O_n$] and [$Eu^{III}O_4Cl_5$] used for the AOM calculations. In red, the global orthogonal coordinate systems with the central atom as origin are indicated. References for the various structures are given in Table 8.1.

The europium(III) oxo-compounds under consideration in this thesis crystallize in different structure types and show a wide variety of mostly low-symmetry chromophores [$Eu^{III}O_n$] ($6 \leq n \leq 9$). Table 8.1 gives a summary of the chromophores and their point groups. Distances d(Eu-L) (L: O, Cl) as well as the orientation of the global (or "molecular") coordinate systems are shown in Figure 8.2. In these compounds, the Eu^{3+} ions are coordinated only by oxygen or by oxygen and chlorine with a total coordination number of eight or nine except for Eu_2O_3. The *C*-type structure of Eu_2O_3 shows two different europium sites with $c.n.(Eu^{3+}) = 6$ [113, 114].

In AOM the orientation of the *f*-orbitals relative to the ligands is defined by the global coordinate system, which is shown for each chromophore in Figure 8.2. In the calculations for

convenience, the global *z*-axis has always been set along to the shortest europium-oxygen bond in a given chromophore.

8.1 Matching procedure

In the first step of ligand-field analysis for the europium(III) compounds in Table 8.1 validity of the aforementioned assumptions (β = 1.0, k = 1.0, $e_\sigma \sim d(\text{Eu-O})^{-7.0}$, e_π = 1/4 e_σ) was checked for $EuPO_4$ and Eu_2O_3. The powder reflectance spectra for the two compounds are given in Figures 8.3 and 8.4, respectively. Introducing Slater-Condon-Shortley parameters F_2, F_4, F_6, and the spin-orbit coupling constant ζ for the free Eu^{3+} ion from ab initio calculations reported in the literature [98] into BonnMag allows a generally good match of the calculated excited state energies to the observed spectra for $EuPO_4$ and Eu_2O_3. The match to those observed for the free Eu^{3+} ion [98] and the very similar data compiled in Diekes diagram [71] is equally good. Typically deviations of $\Delta\tilde{\nu} = \pm 300$ cm^{-1} are found. The observed and calculated energies of the $^7F_0 \rightarrow {}^5D_2$ transition of Eu^{3+} in $EuPO_4$ and Eu_2O_3 have been chosen to visualize the influence of β on the calculated energies (Figure 8.5). For $EuPO_4$ $\beta \approx 1.002$ and for Eu_2O_3 reduction of β to about 0.996 would allow a slightly better match to the experimental energies. These variations are, however, that small that based on currently available data we refrain from discussing them.

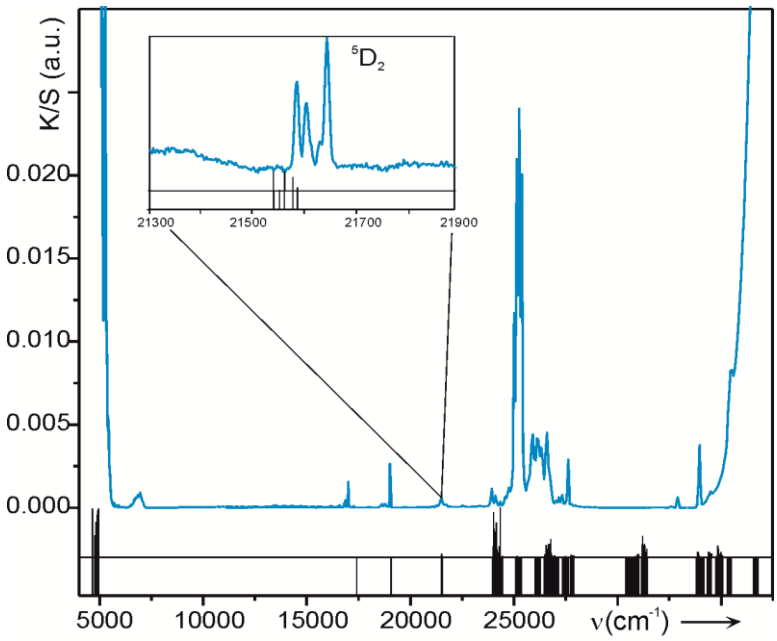

Figure 8.3. UV/vis/NIR spectra of $EuPO_4$ (blue curves). Comparison of results from AOM (zero-phonon lines, black ticks at the bottom) and estimated intensities (Judd-Ofelt theory, height of black ticks) with experimental spectra. Inset: Transition $^7F_0 \rightarrow {}^5D_2$ measured separately with higher resolution (0.05 nm steps, slit 0.015 mm).

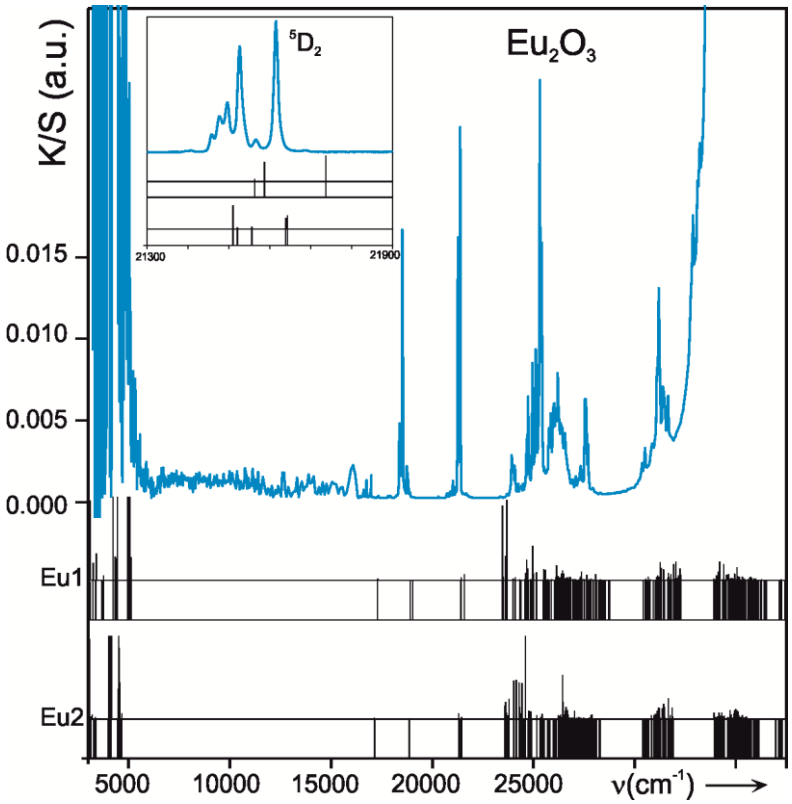

Figure 8.4. UV/vis/NIR spectra of Eu_2O_3(blue curves). Comparison of results from AOM (zero-phonon lines, black ticks at the bottom) and estimated intensities (Judd-Ofelt theory, height of black ticks) for the two crystallographically independent chromophores with experimental spectra. Inset: Transition $^7F_0 \rightarrow {}^5D_2$ measured separately with higher resolution (0.05 nm steps, slit 0.015 mm).

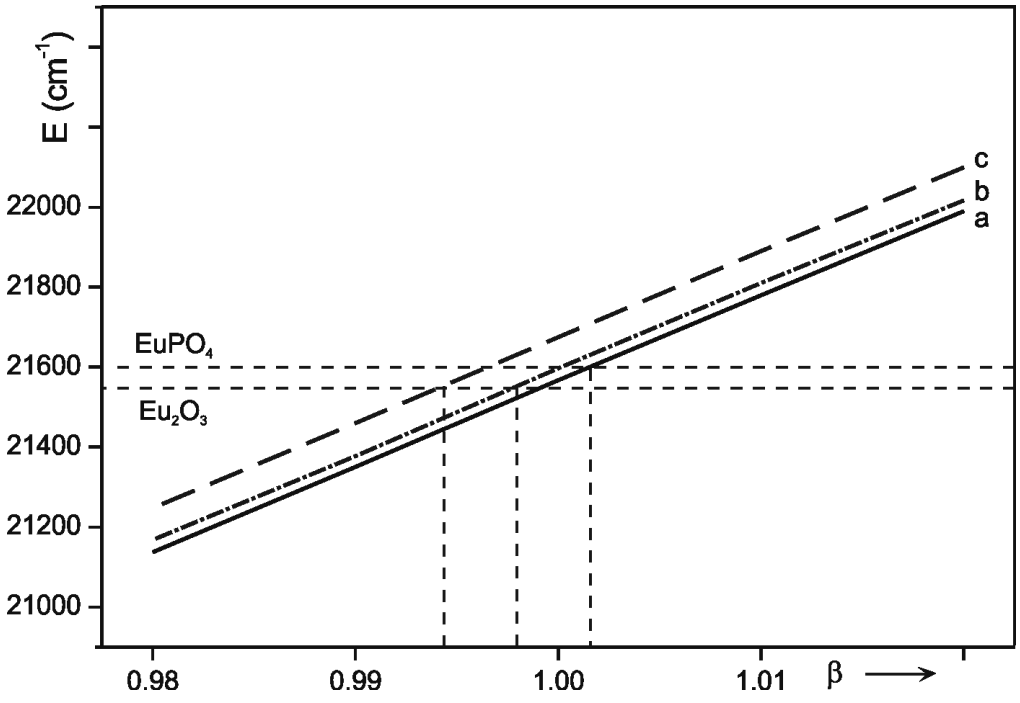

Figure 8.5. Energies for the transition $^7F_0 \rightarrow {}^5D_2$ at $\tilde{\nu} \sim 21500$ cm^{-1}. Horizontal dashed lines indicate experimental energies. Energies calculated with variable β for $EuPO_4$ (a) and Eu_2O_3 with chromophores [$Eu1O_6$] (b) and [$Eu2O_6$] (c).

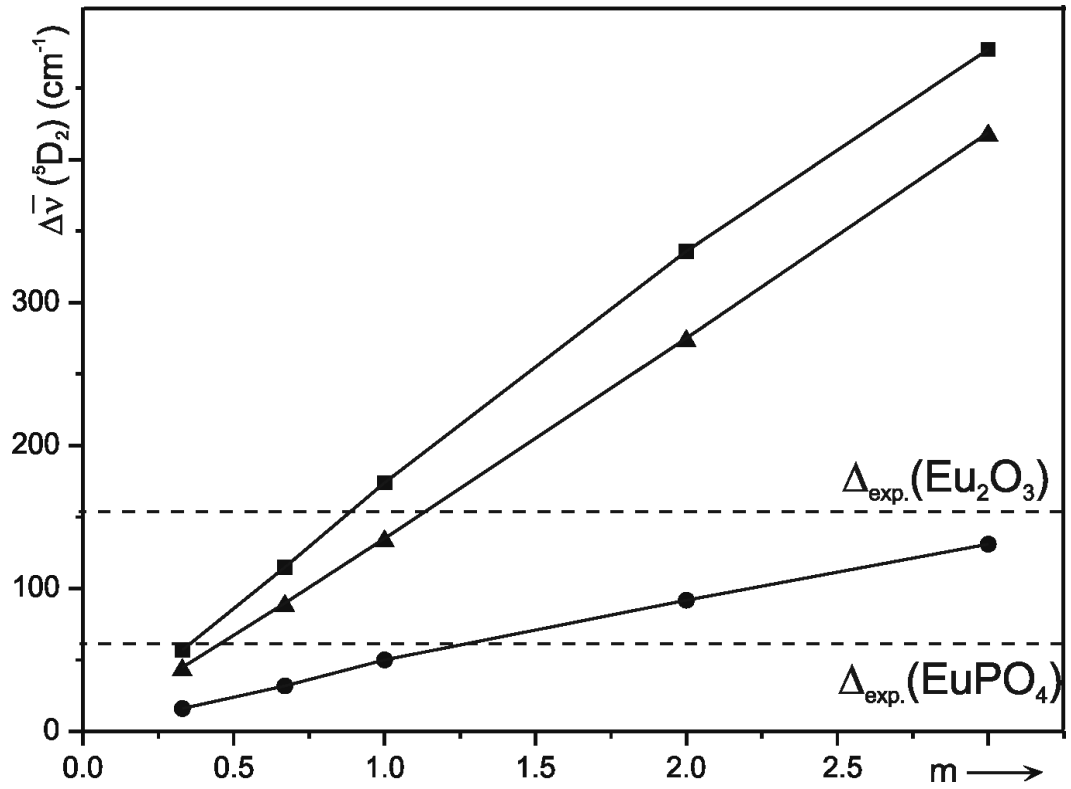

Figure 8.6. Variation of the calculated splittings $\Delta\tilde{\nu}(^5D_2)_{calc.}$ with $m \cdot e_{\sigma,max}$ for $EuPO_4$ (●) and Eu_2O_3 (Eu1:■, Eu2:▲) in comparison to the observed splittings (dashed horizontal lines).

The influence of the ligand-field on the spectra of $EuPO_4$ and *C*-type Eu_2O_3 is shown by the splitting of the $^5D_2$ state (Figures 8.3 and 8.4). For $EuPO_4$ the splitting $\Delta\tilde{\nu}(^5D_2)_{calc.} = 57$ cm^{-1} is observed, for Eu_2O_3 we find $\Delta\tilde{\nu}(^5D_2)_{calc.} = 157$ cm^{-1}. Variation of $e_{\sigma,max}(EuPO_4)$, which is e_σ(Eu-O) for d_{min}(Eu-O) = 2.380 Å in the chromophore [$Eu^{III}O_9$], in the range of 1/3 to three times that of the "best fit" value leads to a significant variation of the calculated splitting of the $^5D_2$ state (Figure 8.6). Obviously, $\Delta\tilde{\nu}(^5D_2)_{calc.}$ increases with $e_{\sigma,max}$(Eu-O). As expected, the calculated magnetic moments (Figure 8.7a-e) depend in the same way on $e_{\sigma,max}$(Eu-O). The splitting of the $^5D_2$ state as well as the observed temperature dependence are nicely accounted for by the "best fit" AOM parameters $e_{\sigma,max}(EuPO_4) = 404$ cm^{-1} and the corresponding $e_{\pi,iso}$(Eu-O) = 101 cm^{-1}. Variation of n in the relation $e_\sigma \sim d(\text{Eu-O})^{-n}$ in the range $3 \le n \le 9$ (with best fit e_σ) for $EuPO_4$ shows no significant influence on the splitting of the $^5D_2$ state ($47 \le \Delta\tilde{\nu}(^5D_2)_{calc.} \le 50$ cm^{-1} for $3 \le n \le 9$). Neither are the temperature dependent magnetic moments (Figures 8.6) significantly affected. Variation of the ratio e_π / e_σ in the range 0.1 to 0.5 (with best fit e_σ) for $EuPO_4$ shows also no influence (Figure 8.7f).

The same variations of $e_{\sigma,max}$ and n (in the relation $e_\sigma \sim d(\text{Eu-O})^{-n}$) for Eu_2O_3 lead to same results as for $EuPO_4$ (Figure 8.8).

As expected from theory, variation of β has a negligible influence on the magnetic moment of Eu^{3+} and its temperature dependence. On the contrary, the influence of k on $\mu/\ \mu_B$ vs. T is high (see Figure A1 in Supplementary Information). Significant reduction of k without reduction of β appears, however, unreasonable [14].

For AOM of EuOCl the parameters e_σ(Eu-Cl) with $e_{\pi,iso}$(Eu-Cl) = 1/4 e_σ(Eu-Cl) were taken from $Cs_2NaEuCl_6$ [127]. The differences in distances d(Eu-Cl) in EuOCl and $Cs_2NaEuCl_6$ were accounted for by relation (9.1).

Matching the calculated optical transition energies and temperature dependent magnetic moments of the remaining compounds ($EuVO_4$, $EuAsO_4$, EuOCl, $Eu_2Ti_2O_7$, $EuNbO_4$, $EuTaO_4$, $EuSbO_4$) to the experimental data was achieved just by variation of $e_{\sigma,\,max}$(Eu-O) for each compound. Table 8.2 provides a summary of the AOM parameterization used in these calculations. Table A5 (Appendix) provides a summary of all AOM parameters for the investigated europium compounds. In Figures 8.9 and 8.10 calculated and observed spectra and magnetic moments are compared.

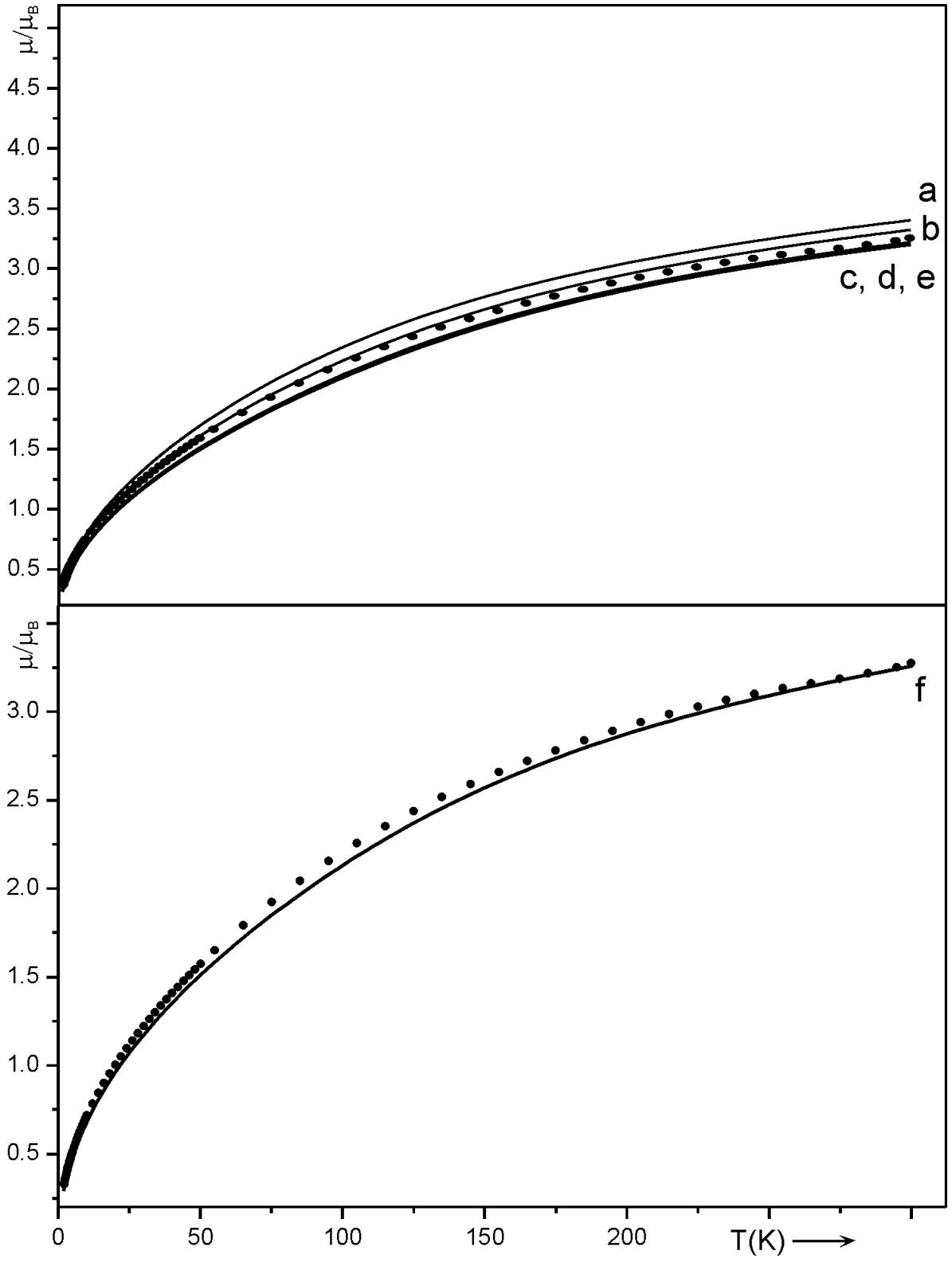

Figure 8.7. Variation of μ/μ_B vs. T for $EuPO_4$ with $e_{\sigma,max}$ and with the exponent n in the relation $e_\sigma \sim d(\text{Eu-O})^{-n}$ (solid lines) in comparison to the observed temperature dependence. a) $3e_{\sigma,max.}$, b) $2e_{\sigma,max.}$, c) "best fit" $e_{\sigma,max.}$, d) $2/3e_{\sigma,max.}$, e) $1/3e_{\sigma,max.}$, f) $3 \leq n \leq 9$.

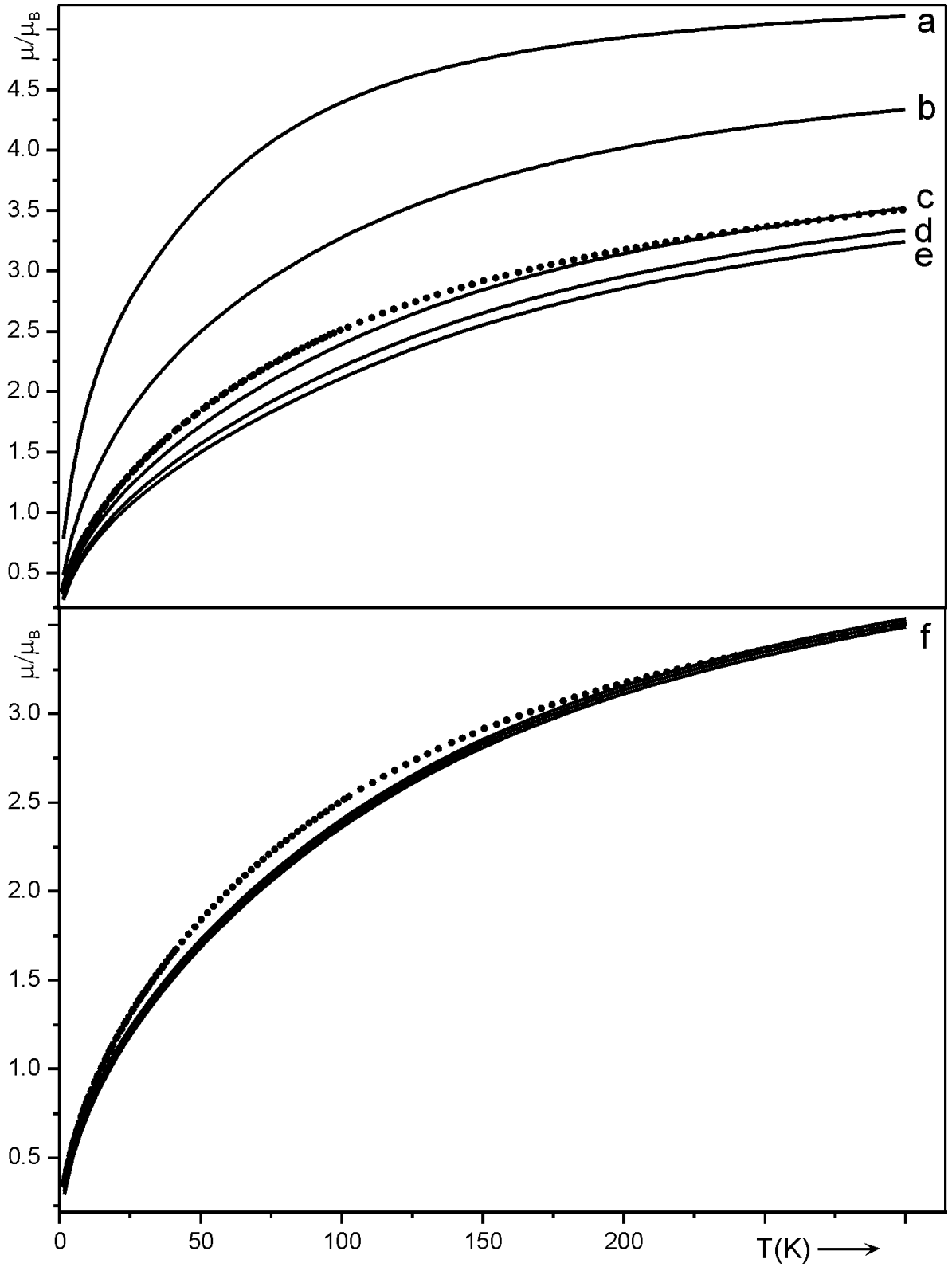

Figure 8.8. Variation of μ/μ_B vs. T for Eu_2O_3 (C-type) with $e_{\sigma,max}$ and with the exponent n in the relation $e_\sigma \sim d(\text{Eu-O})^{-n}$ (solid lines) in comparison to the observed temperature dependence. Note that the experimental as well as the calculated values for μ/μ_B vs. T are the weighted average for the two crystallographically independent chromophores [Eu1O_6] and [Eu2O_6]. a) $3e_{\sigma,max.}$, b) $2e_{\sigma,max.}$, c) "best fit" $e_{\sigma,max.}$, d) $2/3e_{\sigma,max.}$, e) $1/3e_{\sigma,max.}$, f) $3 \leq n \leq 9$.

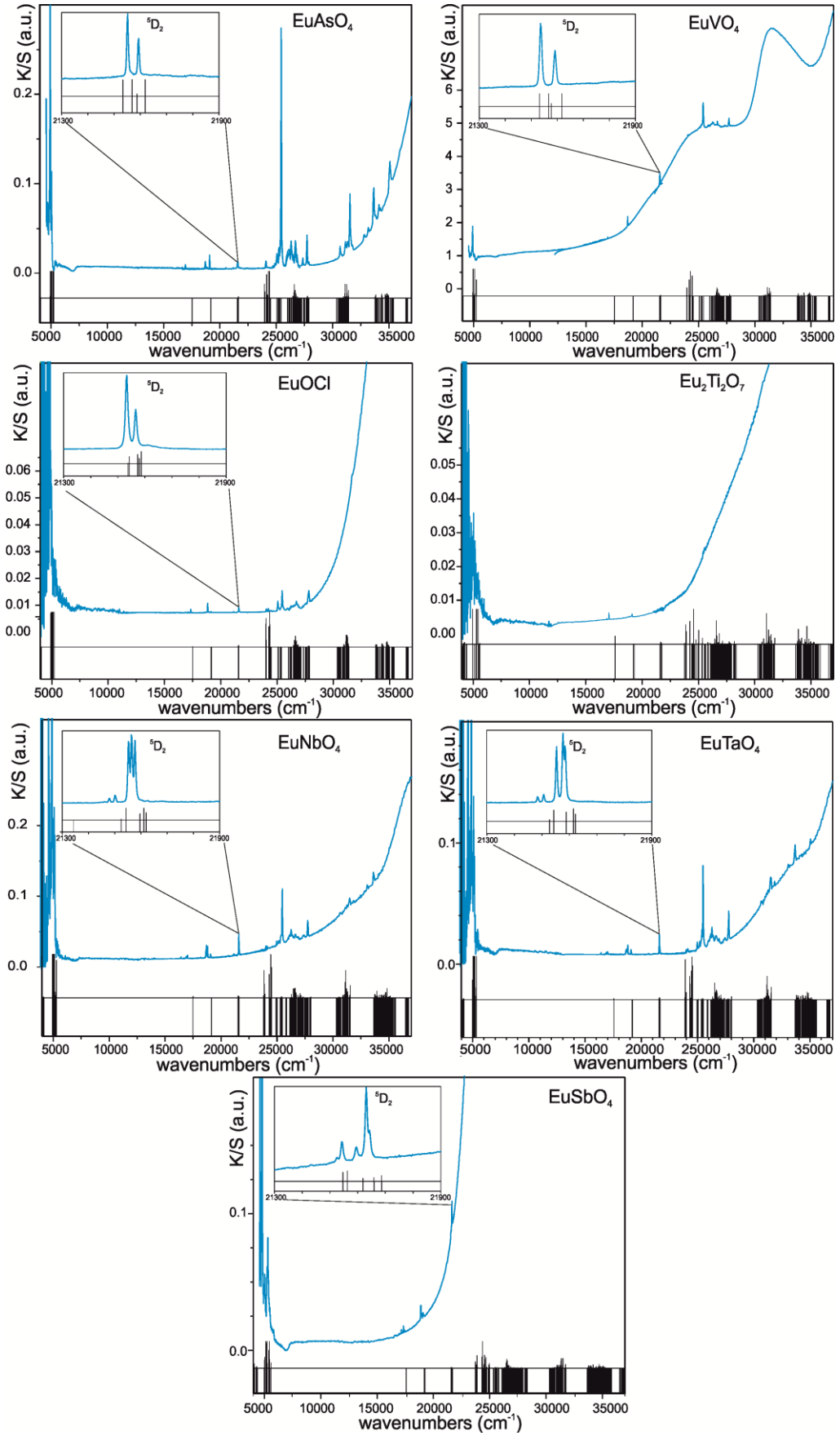

Figure 8.9. UV/vis/NIR spectra (ambient temperature) of europium(III) oxo-compounds (blue curves). Comparison of results from AOM (zero-phonon lines, black ticks at the bottom) and estimated intensities (Judd-Ofelt theory, height of black ticks).

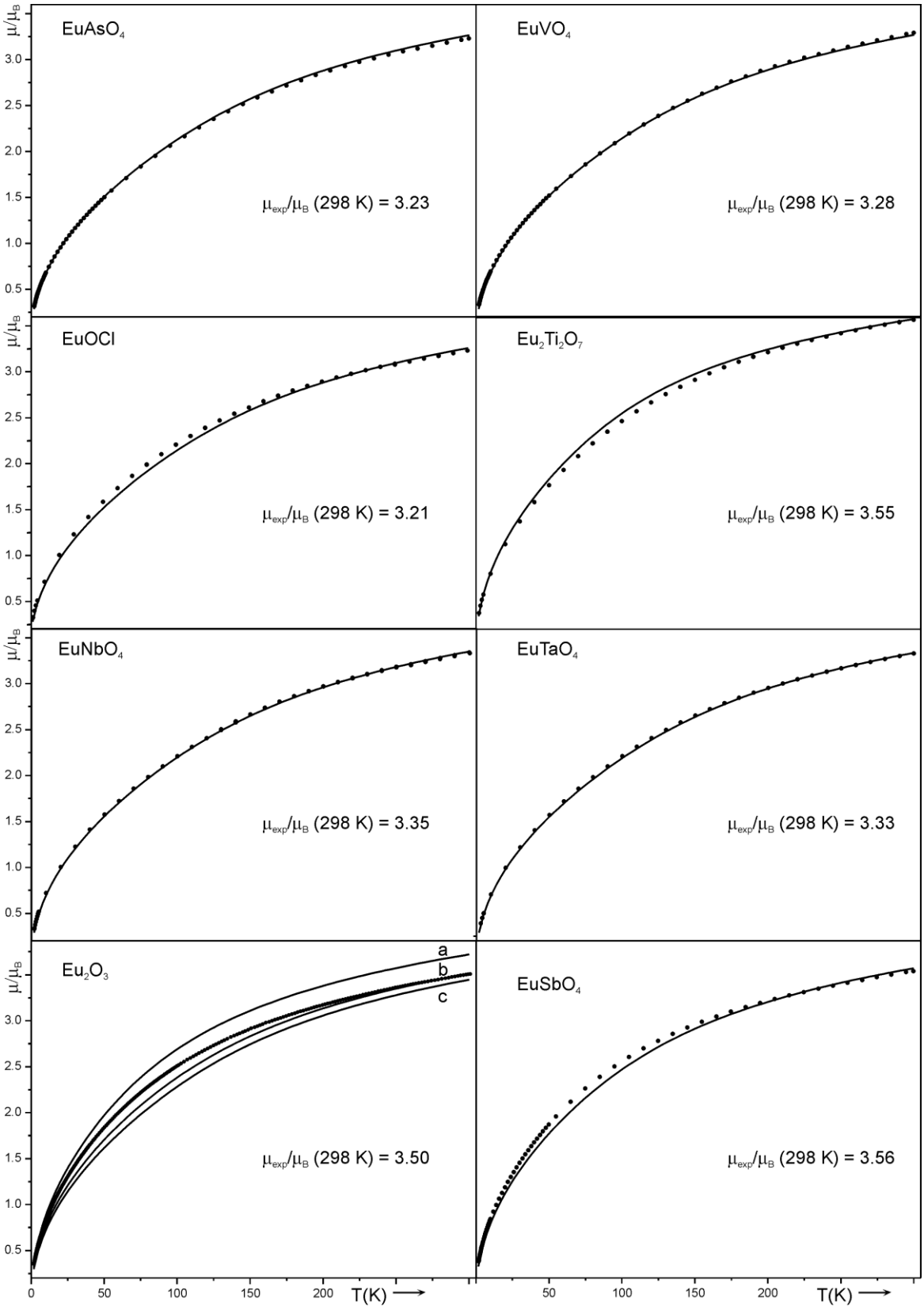

Figure 8.10. Graphical representation of the experimental Bohr magneton numbers μ_{exp}/μ_B vs. T and comparison to the calculated numbers (solid lines). For Eu_2O_3 the weighted average for the two crystallographically independent chromophores [$Eu1O_6$] and [$Eu2O_6$] (b) as well as the individual contributions of Eu1 (a) Eu2 (c) are shown.

Table 8.2. Summary of AOM parametrization for all europium(III) oxo-compounds under consideration.

Slater-Condon-Shortley parameters for Eu^{3+} (cm^{-1}) [98]

F_2 = 401.0 F_4 = 55.38 F_6 = 6.06 ($\beta = F_2 / F_{2,\,f.i.} = 1.0$)

Spin-orbit coupling constant ζ = 1320.0 cm^{-1} [98]

Stevens orbital reduction factor k = 1.0

AOM parameters (all cm^{-1}); $e_{\pi,iso}$(Eu-O) = 1/4 e_{σ}(Eu-O)

compound	d_{min}(Eu-O)	$e_{\sigma,max}$(Eu-O)	$e_{\sigma,norm}$(Eu-O)$_{2.38Å}$
$EuPO_4$	2.380	404	404
$EuAsO_4$	2.350	441.5	404
$EuVO_4$	2.321	481.6	404
EuOCl	2.286	535.7	404
$EuNbO_4$	2.366	589.5	525
$EuTaO_4$	2.366	589.5	525
$Eu_2Ti_2O_7$	2.210	882.4	525
$EuSbO_4$	2.263	977.47	687
Eu_2O_3	Eu1: 2.304	Eu1: 862.0	687
(*C*-type)	Eu2: 2.287	Eu2: 907.9	

8.2 Experimental results

The **optical transitions** in the UV/vis/NIR spectra of the europium(III) oxo-compounds reported here (Figures 8.3, 8.4 and 8.9) are in broad agreement with those summarized for Eu^{3+} ions (neglecting ligand-field splitting) in Diekes diagram [71]. For $EuPO_4$, $EuAsO_4$, $EuSbO_4$, $EuVO_4$, Eu_2O_3, EuOCl electronic absorption spectra with *f-f* intra-shell transitions have been reported before. [111, 128, 129]. Our spectra are in good agreement with these reports.

The influence of the ligand-field on the excited states of Eu^{3+} is shown by our high-resolution powder reflectance measurements of the transition $^7F_0 \rightarrow {}^5D_2$ (Figures 8.3, 8.4 and 8.9) , which have not been measured before. Quite variable splitting patterns are observed and will be discussed subsequently. The number of electronic transitions to the sublevels of $^5D_2$ (Figure 8.3) *C*-type Eu_2O_3 is in nice agreement with the presence of the two crystallographically independent chromophores [$Eu1O_6$] and [$Eu2O_6$] in. The intensities for these transitions are quite different and rather strong in the sesquioxide and undetectable in $Eu_2Ti_2O_7$ (Figures 8.3, 8.4 and 8.9).

Eventually, the spectra provide some hints on electronic excitation in addition to the *f-f* transitions centered on Eu^{3+}. In case of $EuVO_4$ two broad, prominent bands at $\tilde{\nu} \sim 25000$ cm^{-1} and $\tilde{\nu} \sim 32500$ cm^{-1} are observed, which are likely to originate from the transition from the Eu^{3+} ground state $^7F_0$ to the empty *d*-orbitals of V^{5+} in the tetrahedral vanadate(V) group. UV/vis spectra of $Ca_3(VO_4)_2$ show two broad bands caused by LMCT $O^{2-} \rightarrow V^{5+}$ [130]. The energy difference between these two bands for $Ca_3(VO_4)_2$ is $\Delta\tilde{\nu} \sim 7500$ cm^{-1} as found here for $EuVO_4$. We believe that the steep rise in the reflectance spectrum of $EuSbO_4$ at $\tilde{\nu} = 20000$ cm^{-1} is also caused by LMCT, in that case $O^{2-} \rightarrow Sb^{5+}$. In the same way LMCT from O^{2-} to empty *d*-orbitals of Ti^{4+}, Nb^{5+}, and Ta^{5+} may explain the rising "background" at higher wavenumbers in the corresponding compounds.

The estimation of line strengths for the *f-f* transitions according to Judd-Ofelt theory [83, 84] as implemented in BonnMag is in rough agreement with the observations on europium(III) oxo-compounds. The generally very strong absorption related to the transition $^7F_0 \rightarrow {}^7F_6$ is always calculated to be the strongest. The spectra measured at ambient temperature show no hints on "hot bands" (excitation from the thermally populated $^7F_1$ state). On closer inspection, the limits of Judd-Ofelt theory become apparent, as can be seen for the transitions $^7F_0 \rightarrow {}^5D_1$ and $^7F_0 \rightarrow {}^5D_2$ at $\tilde{\nu} \sim 19000$ cm^{-1} and $\tilde{\nu} \sim 21500$ cm^{-1}, respectively. As explained in literature [112] the former are caused by a magnetic dipole mechanism while the latter are described as hypersensitive with respect to the excitation mechanism. Both effects are not covered by the Judd-Ofelt theory.

Rather surprisingly Bohr magneton numbers μ_{exp}/μ_B at 298 K of the oxo-compounds from EuOCl to $EuSbO_4$ cover the unexpectedly wide range from 3.21 to 3.56 (see Table 8.3). Based on various considerations and observations we estimate the accuracy of our μ_{exp}/μ_B to be better than ±0.03. This estimation is supported by comparison of our data for $EuPO_4$, $EuAsO_4$, $EuSbO_4$, $EuVO_4$, EuOCl and $Eu_2Ti_2O_7$ to magnetic measurements reported in literature [111, 115, 131, 132]. Several reports are published in literature on the magnetic behavior of *C*-type Eu_2O_3 [113, 114, 133]. These data are in good agreement with our measurements. For none of the oxo-compounds reported here hints on magnetic ordering were found.

8.3 Ligand-field effects and Angular Overlap Modeling

The ticks representing the calculated excited state energies for the various europium(III) oxo-compounds ("zero-phonon lines", Figures 8.3, 8.4 and 8.9) match nicely the observed

splitting of the $^5D_2$ level of the Eu^{3+} ions by the various ligand-fields. Absolute deviations (as a consequence of slightly deviating free ion parameters F_2, F_4, F_6, and ζ) are generally smaller than 300 cm^{-1}. The magnitude of the LF-splitting $\Delta\tilde{\nu}(^5D_2)_{calc.}$ is generally reproduced by AOM with deviations less than 20 cm^{-1} (Table 8.3). Furthermore, the temperature dependence of the Bohr magneton numbers μ_{exp}/μ_B which is related to the LF splitting of the $^7F_1$ level are, too, very well accounted for by AOM (Figures 8.7, 8.8, and 8.10). The deviations of $\mu/\mu_B = \pm 0.12$ are found. The match between observed and calculated data μ/μ_B vs. T is slightly less good for Eu_2O_3, $EuSbO_4$ and $Eu_2Ti_2O_7$ which show the highest Bohr magneton numbers at 298 K (the highest contribution of thermally populated $^7F_1$ sublevels). Nevertheless, our AOM treatment provides the first ligand-field analysis of *C*-type Eu_2O_3 (Figures 8.4, 8.8, 8.10) allowing for the two quite different chromophores in contrast to work reported in literature [113, 114]. Overall, AOM describes the effects related to the splitting of the free ion levels under the ligand-field with good accuracy.

Obviously, the electronic states of Eu^{3+} in the europium(III) oxo-compounds considered here are well described by using the Slater-Condon-Shortley parameters for the free Eu^{3+} ion from literature [98], the AOM parameters e_σ and e_π reported in this thesis (see Tables 8.2 and A5 in Appendix) and the angular dependent overlap integrals derived from the geometric structure of the chromophores. The radial part of the overlap integral is well accounted for by the dependence of $e_\sigma(Eu^{3+}\text{-}O^{2-})$ on $d(Eu^{3+}\text{-}O^{2-})^{-7}$ (Eq. 9.1). An even better fit of calculated to observed excited state energies should be possible in allowing for a more elaborate model for the description of the free ions electronic states as it was described for $Cs_2NaEuCl_6$ containing the $[Eu^{III}Cl_6]$ chromophore [101]. At the current state we refrain from this procedure for two reasons. In particular for low-symmetry chromophores the fitting of a large parameter set (including SCS, ς, E_{ave}, α, β, γ, T^i (i = 2,3,4,6,7,8), M^k (k = 0,2,4), and P^k (k = 2,4,6) is quite challenging. These parameters are defined according to the conventions used in references [134, 135, 136, 137, 138]. Secondly, it is resonably safe to assume that the AOM (LF) parameters and the parameters for the free ion are independent of each other. Since our investigation focuses on the ligand-field effects and not on the perfect match of the free ion energies only F_2, F_4, F_6 and ζ are used for the parametrization of the free ion states to keep the model as simple as possible. Considering the higher order parameters [101] for the free ion would lead to a rather difficult parametrization procedure. Furthermore, simultaneous least-squares fitting of ligand-field and free ion parameters would not be possible by any means.

Table 8.3. Comparison of observed and calculated splittings $\Delta\tilde{\nu}(^5D_2)_{calc.}$ and of the Bohr magneton numbers μ/μ_B (at 298 K) to the Wybourne ligand-field splitting Δ for the europium(III) oxo-compounds under consideration.

Compound	$\Delta\tilde{\nu}(^5D_2)_{calc.}$ (cm^{-1})	$\Delta\tilde{\nu}(^5D_2)_{exp.}$ (cm^{-1})	μ_{exp}/μ_B (at 298 K)	μ_{calc}/μ_B (at 298 K)	Δ[c)] (cm^{-1})
$EuPO_4$	57	48	3.25	3.23	606
$EuAsO_4$	(50)[b)]	85 (50)	3.23	3.24	663
$EuVO_4$	(57)[b)]	84 (50)	3.27	3.24	656
EuOCl	40	49	3.21	3.24	550
$EuNbO_4$	101	96	3.35	3.36	1138
$EuTaO_4$	102	96	3.33	3.34	1102
$Eu_2Ti_2O_7$	---[d)]	146	3.55	3.56	1157
$EuSbO_4$	120	139	3.56	3.55	1440
C-type Eu_2O_3	157[a)]	Eu1: 174 Eu2: 133	3.50	3.51[e)]	2061 1611

a) Energy difference between the highest and the lowest transition (see Figures 8.3, 8.4, and 8.9). b) Based on the assumption that only four out of five transitions are observed. c) Calculated using definition by Wybourne d) Not observed e) Weighted average of μ_{calc}/μ_B(Eu1) = 3.73 and μ_{calc}/μ_B(Eu2) = 3.43.

As already mentioned the $e_{\sigma,norm}$(Eu-O) value derived here (for d(Eu-O) = 2.38 Å was found by matching the calculated excited state energies and **(!)** magnetic moments against the observed data for $EuPO_4$. For a more precise estimate of the AOM parameter e_σ the splitting of the transition $^7F_0 \rightarrow {}^5D_2$ for $EuPO_4$ at $\tilde{\nu}$ ~21500 cm^{-1} was also considered. This splitting $\Delta\tilde{\nu}(^5D_2)_{calc.}$ = 57 cm^{-1} deviates by only 8 cm^{-1} from the calculated value (Table 8.3). Our $e_{\sigma,norm}$(Eu-O) derived for $EuPO_4$ agrees well with the AOM parameter $e_\sigma(Eu^{3+}\text{-}O^{2-})$ = 549 cm^{-1} which has been reported for Eu^{3+} doped in YOCl [139] for d(Eu-O) = 2.278 Å. This is the average of the distance values for EuOCl (d(Eu-O) = 2.286 Å) and YOCl (d(Y-O) = 2.27 Å). The $e_{\sigma,norm}$(Eu-O) value for the doped compound converted to d(Eu-O) = 2.38 Å is 399 cm^{-1}. The assumed d(Eu-O) for Eu^{3+} doped in YOCl appears to be reasonable. For Eu^{3+} doped in Y_2O_3 [139] for d(Eu-O) = 2.250 Å and d(Eu-O) = 2.330 Å the values $e_\sigma(Eu^{3+}\text{-}O^{2-})$ = 881 cm^{-1} and $e_\sigma(Eu^{3+}\text{-}O^{2-})$ = 391 cm^{-1}, respectively have been reported in literature. The values for e_σ(Eu-O) derived for $EuPO_4$ range from 160 cm^{-1} to 404 cm^{-1}. For other lanthanide oxo-compounds the values e_σ(*Ln*-O) = 475 cm^{-1} (d(Nd-O) = 2.386 Å in $NdAlO_3$ [140]), 450 cm^{-1}

(d(Nd-O) = 2.4 Å in Nd_2O_3[140]), 318 cm^{-1} (d(Er-O) = 2.402 Å in $Er(OH)_3$ [140]), and 360 cm^{-1} (d(Yb-O) = 2.19 Å in $CsYbO_2$[141]]).

In case of EuOCl the variation of the e_σ(Eu-Cl) obtained from the scaling of the value reported for $Cs_2NaEuCl_6$ shows only a rather small influence on the calculated transition energies and magnetic moments.

The fitting procedure for the whole set of experimental data shows clearly, that $e_{\sigma,max}$(Eu-O) does not only depend on the distance d(Eu-O) but also on some additional effect. Thus, for matching the observed data for all oxo-compounds the AOM parameter $e_{\sigma,max}$(Eu-O) (normalized to d(Eu-O) = 2.38 Å) had to be increased significantly in the series $EuPO_4$ ($EuVO_4$, $EuAsO_4$, EuOCl) → $Eu_2Ti_2O_7$ → $EuNbO_4$ ($EuTaO_4$) → Eu_2O_3 ($EuSbO_4$) from 404 cm^{-1} to 687 cm^{-1}. Our data suggest an increase of e_σ(Eu-O) not only with decreasing distance d(Eu-O) but also with the basicity of oxygen in the various compounds. Using the optical basicity Λ [142, 143, 144, 145] with Λ($EuPO_4$) = 0.62, Λ($EuNbO_4$) = 0.79, and Λ(Eu_2O_3) = 1.10, a roughly linear increase of e_σ(Eu-O) on Λ is found. The dependence of e_σ(Eu-O) on d(Eu-O) and Λ is visualized in Figure 8.11.

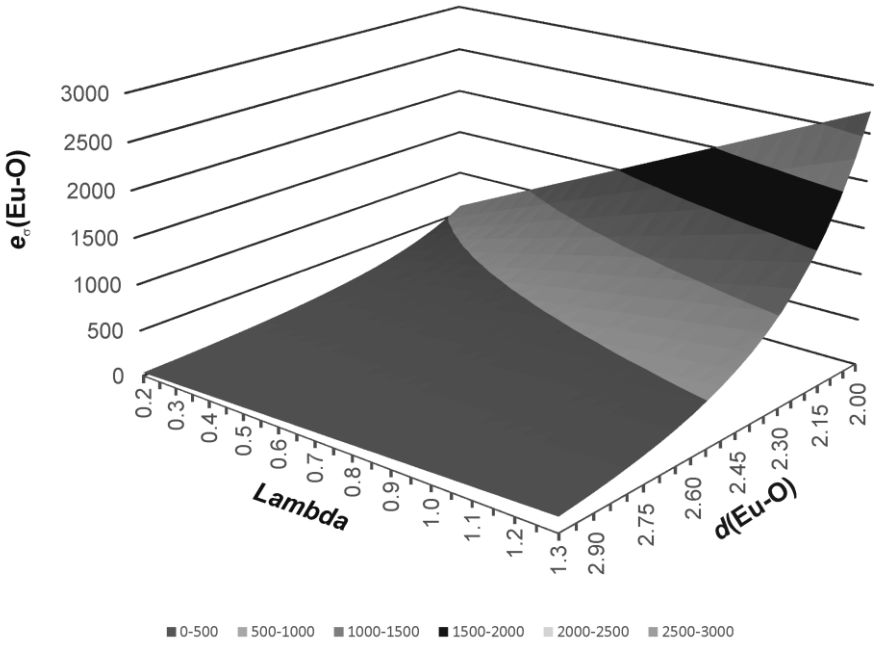

Figure 8.11. Dependence of e_σ(Eu-O) on d(Eu-O) and optical basicity Λ.

In literature [146] occasionally an "effective ligand-field splitting" (better splitting of the $^7F_1$ state by the ligand-field) has been considered as a parameter in van Vlecks equation to describe empirically the contribution of the first excited state to the overall Bohr magneton number and thus the temperature dependence of μ/μ_B. Comparison of the various ligand-field

splittings Δ (Table 8.3) as derived from the AOM parameters e_σ and e_π and the splitting patterns calculated by AOM for the $^7F_1$ states in the various chromophores (Figure 8.12) regarded here provides a much more detailed picture.

By using the definition given by Wybourne [35] (Eq. 9.2) the ligand field strength Δ was calculated for all europium(III) compounds from the obtained "best-fit" AOM parameters e_σ and e_π. These calculations were performed within BonnMag. Note: While Δ is directly related to the AOM parameters deduction of e_σ and e_π from the Wybourne parameters is only possible by an indirect iteration procedure [35].

Clearly, the Bohr magneton number is correlated to the splitting of the $^7F_1$ state. In a first approximation larger splitting of the $^7F_1$ state leads to higher values $\mu_{exp.}/\mu_B$ at 298 K with $\mu_{calc.}/\mu_B$ (298 K) = 3.20 for the free Eu^{3+} ion as lower limit. A detailed comparison (Table 8.3 and Figure 8.11) of μ/μ_B(298 K) with Δ shows however clear deviations from this simple relation. The calculated splitting of the $^7F_1$ state for $EuAsO_4$ and $EuVO_4$, for example, is very small (ca. 1 cm^{-1}). The calculated magnetic moment at 298 K and its temperature dependence (which matches the experimental data perfectly) are, however, almost the same as for $EuPO_4$ with a calculated splitting of the $^7F_1$ state of 77 cm^{-1}. In contrast, the Wybourne ligand-field strengths Δ for $EuAsO_4$ and $EuVO_4$ (Table 8.3) are about 10% higher than $\Delta(EuPO_4)$.

The calculated splitting of the $^7F_1$ state for the chromophore $[Eu^{III}O_8]$ in $Eu_2Ti_2O_7$ is huge (ca. 350 cm^{-1}; Figure 8.12). Yet, the magnetic behavior of the titanate is very similar to that of $EuSbO_4$ and Eu_2O_3 (*C*-type) for which much smaller splittings of the $^7F_1$ state are calculated (Figure 8.10 and 8.12). In the context of this discussion it appears also quite interesting that the ligand-field splitting Δ as well as the calculated magnitude of splitting of the $^7F_1$ state for presumably rather similar chromophores like $[Eu1O_6]$ and $[Eu2O_6]$ in Eu_2O_3 can be quite different. It appears therefore even more remarkable that AOM of the two chromophores leads to a good match between calculated and experimental μ/μ_B vs. *T*.

Inspection of the splittings calculated for the $^7F_1$ states (Figure 8.12) in the various chromophores reveals further effects that will have some impact on μ/μ_B vs. *T*. a) The three sublevels resulting from interaction of the $^7F_1$ state with the ligand-field follow roughly three different splitting patterns. These might be described as "2 above 1" (as for chromophore $[Eu1O_6]$ in Eu_2O_3), "three well resolved sublevels" (as for e.g. $EuPO_4$, $EuTaO_4$, and $EuSbO_4$), and "1 above 2" (as for chromophores $[Eu2O_6]$ in Eu_2O_3 and $[EuO_8]$ in $Eu_2Ti_2O_7$). These splitting patterns are a direct consequence of the chromophores (ligand-fields) symmetry and, not surprisingly, both, symmetry and ligand-field strength Δ, will affect the magnetic behavior.

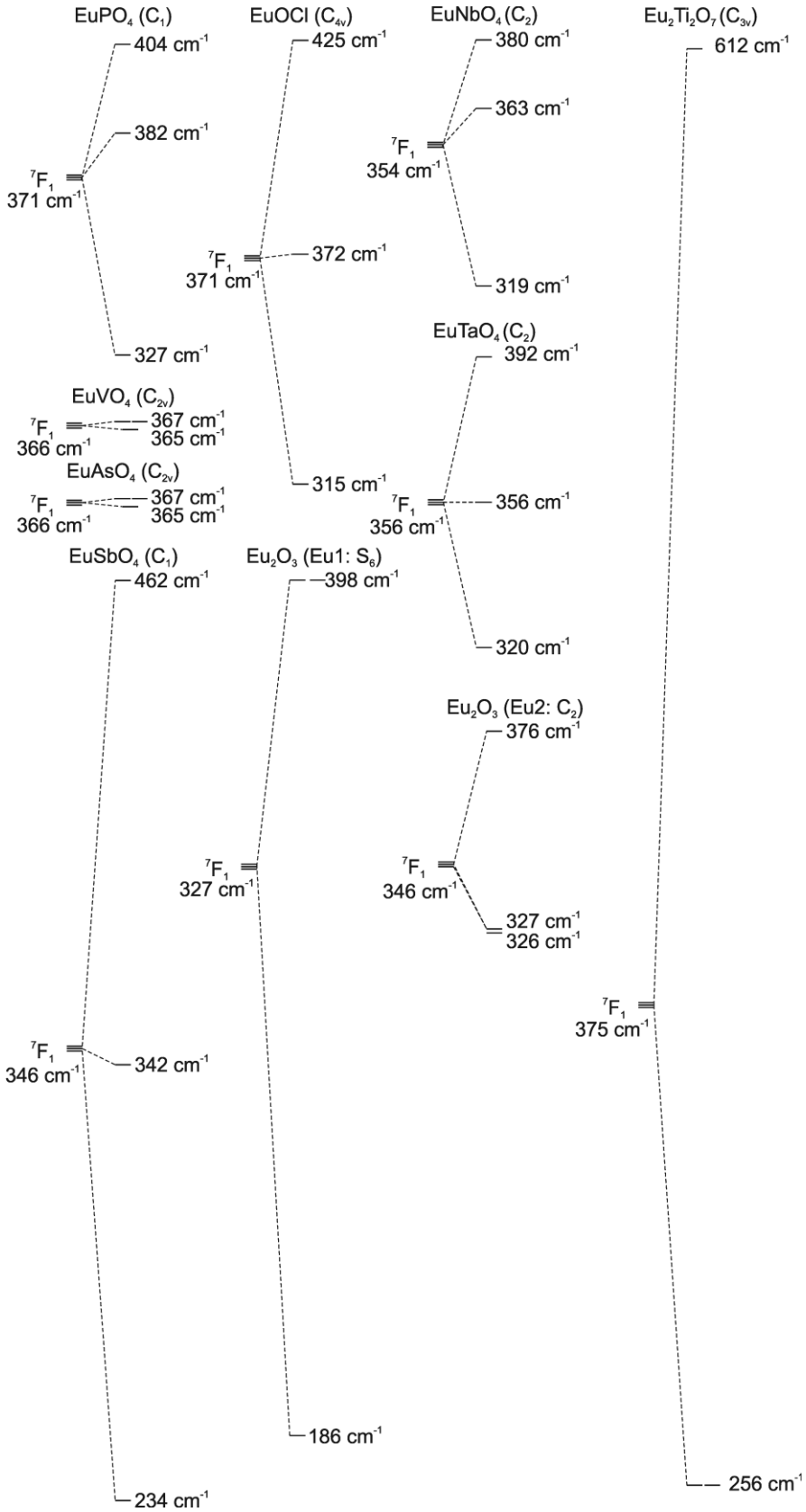

Figure 8.12. Calculated (AOM, parameters in Table 8.2) splitting of the first magnetic state $^7F_1$ of Eu^{3+} in the chromophores $[Eu^{III}O_n]$ and $[Eu^{III}O_4Cl_5]$. The energy (above the ground state $^7F_0$) assigned to the parental term $^7F_1$ represents the center of gravity of the energies of the LF split terms. With the same SCS parameters (see Table 8.2) for the free Eu^{3+} ion $E(^7F_1)$ = 373 cm^{-1} is obtained.

Figure 8.12 shows also nicely that configuration interaction between the $^7F_1$ sublevels and the sublevels of appropriate symmetry of higher states can take on significant values. Without configuration interaction the center of gravity of the sublevels should be the same for the free Eu^{3+} ion, where the $^7F_1$ state is 373 cm^{-1} above the $^7F_0$ ground state, and for all chromophores. The fact that this is obviously not the case points to significant contributions of configuration interaction that will lower the $^7F_1$ sublevels with respect to the ground state and will also lead to admixture of contributions from levels with even higher magnetic moment than $^7F_1$. AOM points for the $[EuO_8]$ chromophore in $Eu_2Ti_2O_7$ to a possible crossing in energy of the highest sublevel of $^7F_1$ and the lowest of $^7F_2$ on slight variation of $e_{\sigma,\,max.}$ and of the ratio e_π/e_σ. In particular for the oxo-compounds with the highest values $\mu_{exp.}/\mu_B$(298 K), namely $EuSbO_4$, Eu_2O_3, and $Eu_2Ti_2O_7$ such effects might be responsible for the slightly less good match of calculated and observed data (Figure 8.10). To settle this question future measurement of emission spectra of the oxo-compounds considered here is planned. Via such measurements direct characterization of the splitting of $^7F_1$ and $^7F_2$ states would be possible.

9 Uranium(IV) phosphate chloride

UPO_4Cl [147] was used as a test compound for the calculations of energy levels and magnetic susceptibilities. As basis for our detailed treatment of metal-ligand interactions and of the ligand-field influence highly resolved, polarized single-crystal absorption spectra and temperature dependent magnetic susceptibilities of UPO_4Cl are used [148, 149]. Our AOM calculations using BonnMag allow separation of the effects of ligand field splitting and spin-orbit coupling on the energy of the observed electronic states. Due to the simple and fast procedure a large number of calculations with variation of parameters are possible. Thus, assessment of the "best fit AOM parameters" is for UPO_4Cl accomplished.

In UPO_4Cl uranium (Wyckoff position 4*c*, site symmetry C_{2v}) is coordinated by six oxygen and two chlorine atoms (see Figure 9.1). There are four different distances *d*(*M*-*L*) with *d*(U-O1) = 2.207 Å, *d*(U-O2) = 2.296 Å, *d*(U-O2') = 2.579 Å and *d*(U-Cl) = 2.804 Å [149].

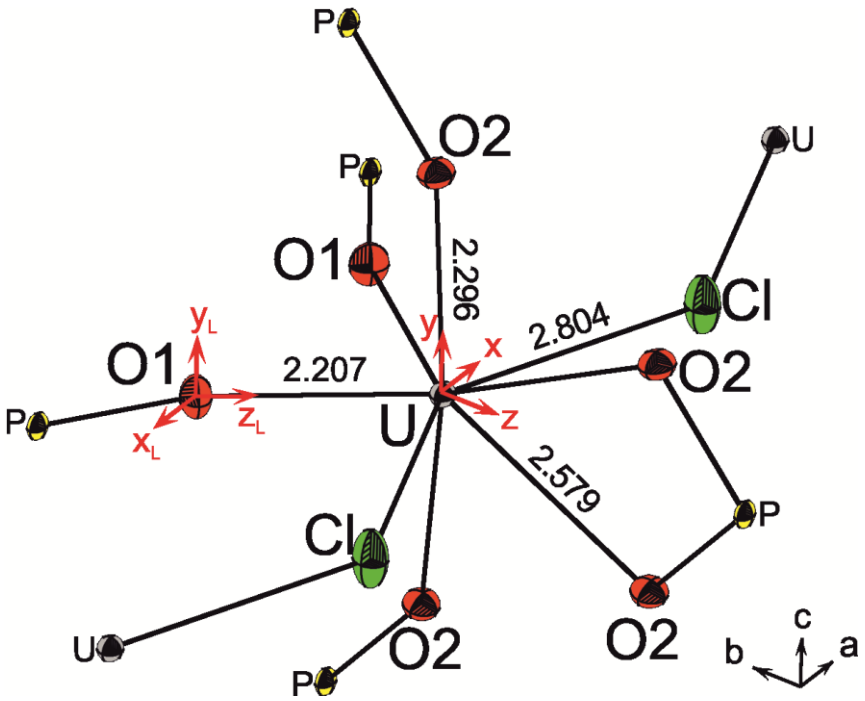

Figure 9.1 ORTEP representation of the $[U^{IV}O_6Cl_2]$ chromophore in UPO_4Cl given with the second coordination sphere and coordinate systems for the central atom (global coordinate system) and one ligand as example (index *L*) [149].

The Slater-Condon-Shortley parameters F_2, F_4, F_6 and the spin-orbit coupling constant ζ for the U^{4+} ion were taken from the analysis of the UV/vis spectrum of the $[U^{IV}Cl_6]$ chromophore in $Cs_2U^{IV}Cl_6$ [150].The AOM parameters e_σ(U-O) and $e_{\pi,iso}$(U-O), for a given distance *d*(U-O)

were obtained by matching the calculated magnetic susceptibilities and excited state energies against the observed data. The $e_{\pi,iso}$ were taken as one quarter of the corresponding e_{σ}. The parameters e_{σ}(U-Cl) = 1270cm^{-1} and $e_{\pi,iso}$(U-Cl) = 318 cm^{-1} were transferred from $Cs_2U^{IV}Cl_6$. The different distances d(U-Cl) in UPO_4Cl and Cs_2UCl_6 were accounted for by relation (5.1). "Best fit" parameters (Table 9.1) were derived by visual comparison of calculated and observed data. This procedure leads to e_{σ}(U-O) = 2052 cm^{-1} and $e_{\pi,iso}$(U-O) = 513 cm^{-1} for $d(\text{U-O})_{min}$ = 2.207 Å. In order to account for the different interatomic distances d(U-O) in UPO_4Cl $e_{\sigma}(d)$ and $e_{\pi,iso}(d)$ are scaled in the following way [26].

$$e_m(d) = e_m(d(U-L)_{min}) \cdot \left(\frac{d(U-L)_{min}}{d(U-L)} \right)^7 \text{, } (m\text{: } \sigma, \pi; L\text{: O, Cl}) \qquad \text{Equation 9.1}$$

Second sphere ligand effects [34] were neglected in our modelling, to keep the parametrization as simple as possible. With the same reasoning, only isotropic π-interactions have been considered.

For the AOM calculations on the chromophores $[U^{IV}O_6]$ (octahedral with slight angular distortion in UP_2O_7), and $[U^{IV}O_7]$ in $U_2O(PO_4)_2$ (see Figure 9.6) the parameters were directly transferred from UPO_4Cl (same F_2, F_4, F_6, and ζ; e_{σ} adjusted to distance U-O). Details on these chromophores and the AOM parameters are given in Figures A1 and A2 and in Tables A1 and A2.

For the calculation of absorption coefficients (line strength) the well-established Judd-Ofelt parameters Ω_n (n = 2, 4, 6) of Pr^{3+} (f^2) [90-93] were taken as initial values. The good fit between calculated and observed line strengths for the U^{4+} ion in UPO_4Cl (Figure 9.2) and further uranium(IV) phosphates (Figure 9.6) was eventually obtained by reducing the third parameter Ω_6 from $4.529 \cdot 10^{-24}$ m^2 to $0.4529 \cdot 10^{-24}$ m^2. Table 9.1 gives a summary of all parameters.

Table 9.1. "Best-fit parameters" [a] for the angular overlap modeling of the $[U^{IV}O_6Cl_2]$ chromophore in UPO_4Cl.

Slater-Condon-Shortley parameters (cm^{-1})

F_2 = 190.9 F_4 = 33.74 F_6 = 3.99675 ($\beta = F_2 / F_{2,\,f.i.}$ = 0.82)

Slater-Condon-Shortley parameters of the free U^{4+} ion (cm^{-1}) [151]

$F_{2,\,f.i.}$ = 234.73 $F_{4,\,f.i.}$ = 41.35 $F_{6,\,f.i.}$ = 4.10

Spin-orbit coupling constant (cm^{-1})

ζ = 1797.02

Stevens-orbital reduction factor [152**]**

k = 0.95

Interaction parameters e_m(U-O), e_m(U-Cl) (m: σ, π)

Ligand	Distance (Å)	e_σ (cm^{-1})	$e_{\pi,iso}$ (cm^{-1})	e_π / e_σ
O1	2.207	2052	513	0.25
O2	2.296	1556	389	0.25
O2	2.579	690	173	0.25
Cl	2.804	1270	318	0.25

Judd-Ofelt parameters (10^{-24} m^2)

Ω_2 = 1.078 Ω_4 = 2.014 Ω_6 = 0.4529

a) From visual comparison of observed and calculated transition energies, line strengths, and the dependence of magnetic moment on temperature.

9.1 Summary of the experimental data

Figure 9.2 shows the good match between observed and calculated electronic transition energies (zero-phonon lines). It also shows good agreement between observed and calculated line strengths. This confirms that the electronic states of U^{4+} can be described well by using Slater-Condon-Shortley parameters and the AOM parameters e_σ and e_π given in Table 9.1. Due to the good compliance between observed spectra and the results from modeling a safe assignment of the observed electronic transitions is achieved (Figure 9.2, Table A4). Deviations between observed and calculated electronic transition energies are generally small (< 500 cm^{-1}). It appears that the generally good match between observed and calculated absorption coefficients is less good at higher wavenumbers, above 20000 cm^{-1}. Effective Bohr magneton numbers [13] μ_{eff} calculated using the same parameters show a very good match with the experimental data (Figure 9.7*b*).

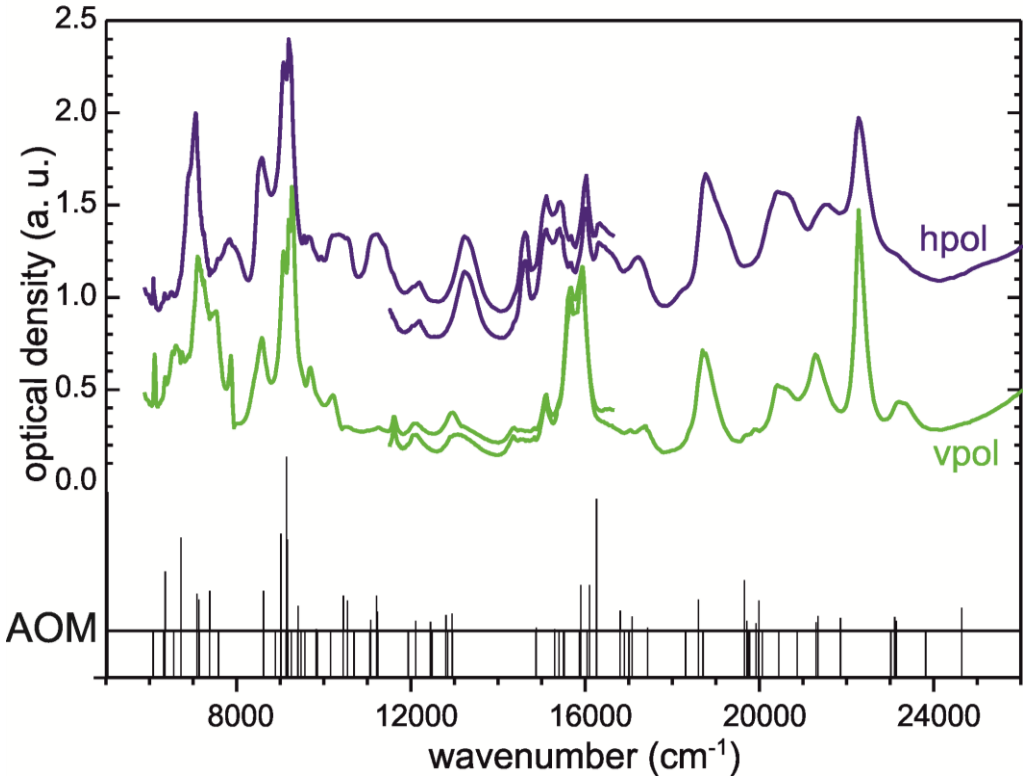

Figure 9.2. Polarized electronic absorption spectra of a (010) crystal face of $U(PO_4)Cl$. "hpol" and "vpol" denote perpendicular polarisation directions of the incident light beam. Angular overlap results (zero-phonon lines) (AOM) with estimated intensities (Judd-Ofelt theory) [149].

9.2 Variation of parameters

In order to check the dependence of the theoretical results on the parameters the Slater-Condon-Shortley parameter F_2 was varied and the calculated optical transition energies were compared to those from the "best fit" calculation. The ratios F_2 / F_4 and F_2 / F_6 were kept constant in these calculations. Varying F_2 by ±5% leads to a shift (up to ~1500 cm^{-1}) of the calculated transition energies to lower and higher values, respectively (s. Figure 9.3). The good match between calculated and experimental energies is lost. As expected the calculated effective Bohr magneton number μ_{eff} does not show a significant dependence on F_2 (Figure 9.7*d*/*f*).

The Slater-Condon-Shortley parameters available in literature for the free U^{4+} ion (see Table 9.1) were determined from the measured emission spectrum of gas phase U^{4+} for the high energy region 43000-165000 cm^{-1}. The energies calculated in our investigation with "best fit" Slater-Condon-Shortley parameters are at much lower wave numbers (see Figure 9.3). Nevertheless, the nephelauxetic ratio (β = F_2 / $F_{2,\ f.i.}$ = 0.82) is, as expected, considerably smaller than values for β observed for lanthanide ions.

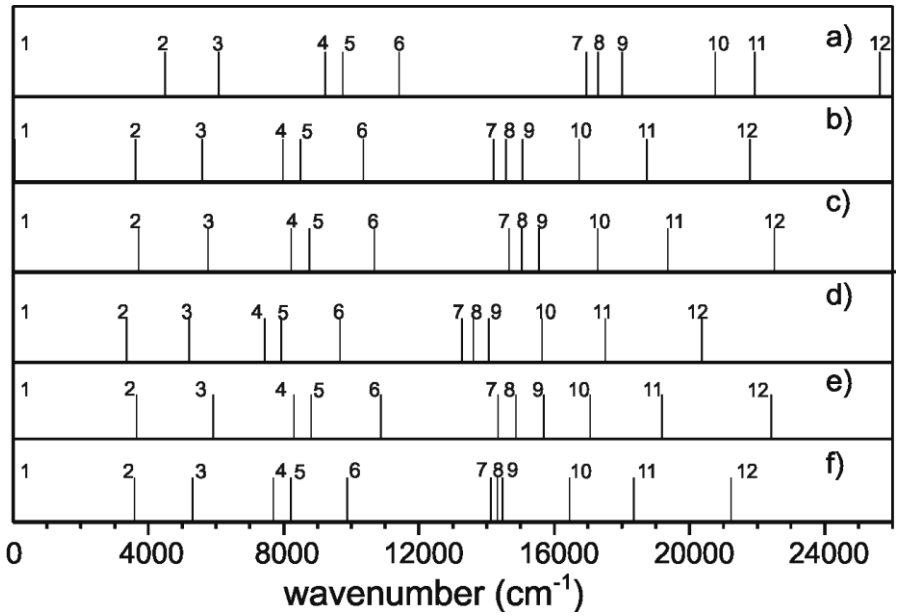

Figure 9.3 Transition energies for the free ion U^{4+} ($e_\sigma = e_\pi = 0$ cm^{-1}) calculated with different sets F_2, F_4, F_6 and ζ. Condon-Shortley parameters and spin-orbit coupling for the free U^{4+} ion derived from arc spectra, $\zeta_{free\ ion}$ = 1969 cm^{-1} (a), "best fit" SCS parameters for U^{4+} used in present AO modeling {derived for the chromophore $[U^{IV}Cl_6]$, ζ = 1797.02 cm^{-1} [22] (b)}, "best fit" parameters increased by 5% (F_2 and ζ) (c), "best fit" parameters decreased by 5% (F_2 and ζ) (d), "best fit" SCS parameters with ζ = 1886.87 cm^{-1}, (e), "best fit" SCS parameters with ζ = 1707.17 cm^{-1} (f). Sequence of the free ion states 1 to 12: $^3H_4$, $^3F_2$, $^3H_5$, $^3F_3$, $^3F_4$, $^3H_6$, $^3P_0$, $^1D_2$, $^1G_4$, $^3P_1$, $^1I_6$, $^3P_2$.

By variation of the interaction parameters e_σ and e_π and therefore of the strength of the ligand field the effect of these parameters on the energies of the optical transitions was investigated. The results of a series of calculations with e_σ ranging from zero to 120 % of the "best fit" values are summarized in Figure 9.4 (e_π = ¼ e_σ). By increasing the interaction energies (ligand field strength), the splitting of the parental terms increases as expected. By this gradual increase of the ligand field assignment of the resulting terms to the parental terms becomes possible. Inspection of the splitting as function of e_σ shows also, that term interaction becomes increasingly important with increasing e_σ. Thus, only for adjacent states at low e_σ the inspection of their J projection leads to a safe assignment of the resulting terms to their parental terms. Above 110% of the best-fit values for the e_σ the relation to the parental term is completely lost due to the increasing term interaction.

For the excited state energies calculated with the best-fit parameters (Table 9.1), an unambiguous assignment to certain parental terms is impossible without additional criteria. It becomes obvious from Figure 9.4 that only for e_σ in the range from 90% to 110% of the best fit values a reasonable match between observed and calculated transition energies is achieved. As shown in Figure 9.7 the temperature dependence of the effective Bohr magneton number

μ_{eff} is far more susceptible to variation of e_σ. These comparisons allow an estimate of the accuracy of the "best fit" parameter set. Further corroboration for the magnitude of e_σ is obtained by comparison of the observed and calculated splittings of the parental states (Figure 9.5). The influence of the scaling of the interaction parameters with distance $e_\sigma \sim d(\text{U-O})^{-x}$ (x = 5.0, 7.0, 8.0) is shown in Figure 9.5. The various exponents lead in all calculations to rather good matches with the observed transition energies and the effective number of Bohr magnetons. Yet, these data are not very sensitive to x, which in turn cannot be determined more precisely.

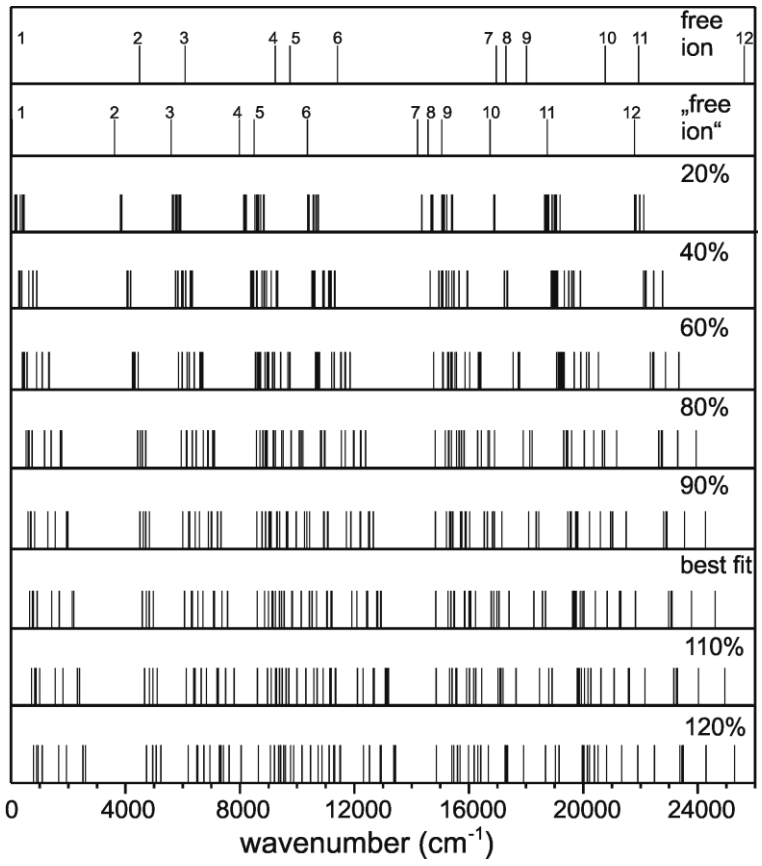

Figure 9.4 Calculated transitions for the free ion U^{4+} ("free ion" means that the nephelauxetic ratio β has been considered) and the chromophore $[UO_6Cl_2]$ with increasing strength of the ligand field (e_σ ranging from zero to 120 % of the "best fit" values). The percentages refer to the "best fit" e_σ and e_π values from table 1. Sequence of the free ion states 1 to 12: $^3H_4$, $^3F_2$, $^3H_5$, $^3F_3$, $^3F_4$, $^3H_6$, $^3P_0$, $^1D_2$, $^1G_4$, $^3P_1$, $^1I_6$, $^3P_2$. $\zeta_{\text{free ion}}$ = 1969 cm^{-1}, ζ_{AOM} = 1797.02 cm^{-1}.

BonnMag calculates the J projections and determines the irreducible representation for each eigenstate by procedures described in literature.[36 - 38] From the J projections and the symmetry analysis of the eigenvector the parental term with the highest contribution to a given eigenstate is determined. As example Figure 9.5 shows the contribution of various parental terms to the states between 8000 and 11000 cm^{-1}. With this analysis the influence of the magnitude of e_σ (ligand field) on the splitting can be better understood.

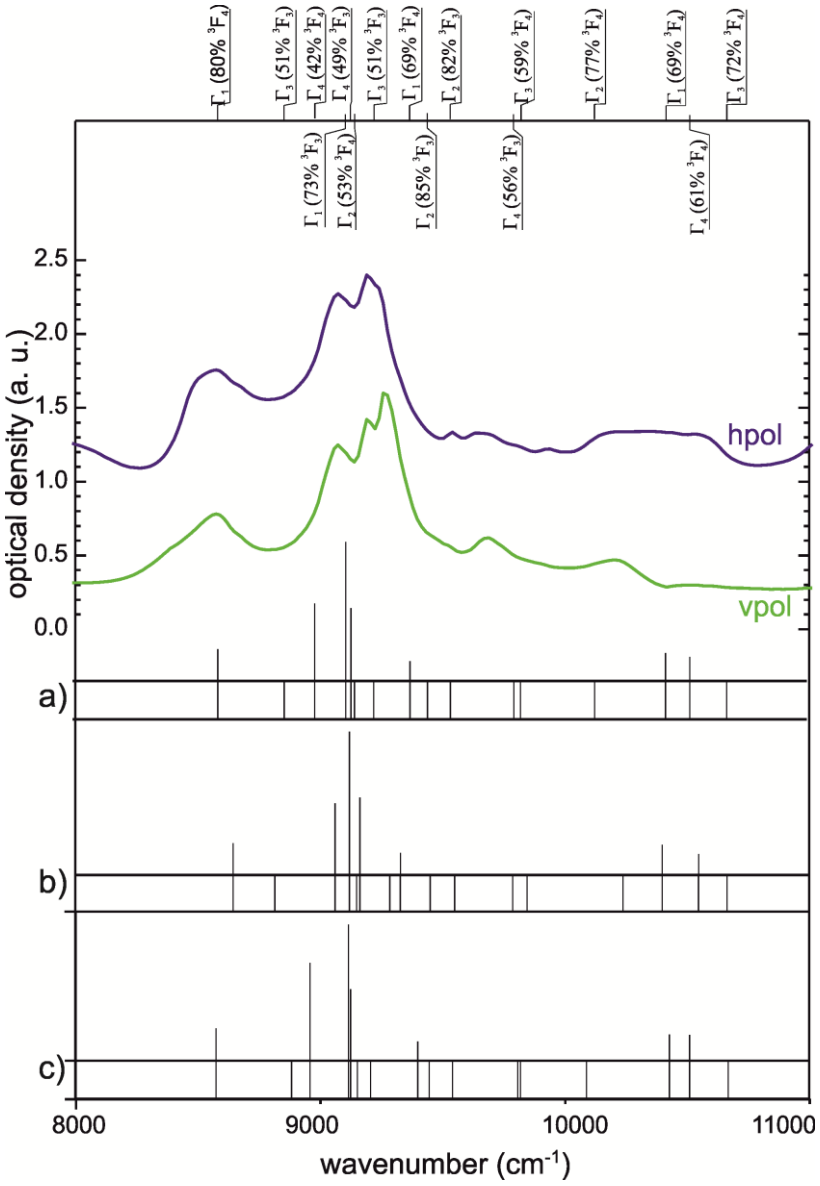

Figure 9.5 UV/vis/NIR-spectra of UPO_4Cl with the simulated transition energies for the region between 8000 and 11000 cm^{-1} calculated by BonnMag and symmetry analysis of the terms. Angular overlap modeling (zero-phonon lines) with estimated intensities (according to Judd-Ofelt theory). The parental terms with the largest contribution to the splitting term are given in parentheses.

The calculations of *J* projections confirm that term interaction between neighboring terms is significant for U^{4+}. Above 10000 cm^{-1} $^3F_4$ interacts with the neighboring state $^3H_6$, so that $^3H_6$ has a considerable admixture of the lower state. Due to the symmetry analysis and calculation of absorption coefficients the quantitative assignment of the terms to the observed transitions becomes possible.

For the 8000-11000 cm^{-1} region (see Figure 9.5) of the spectra the irreducible representations of the split terms were determinated. The point group C_{2v} of the chromophore $[U^{IV}O_6Cl_2]$ was used. It is shown, that according to Judd-Ofelt theory some transitions have no intensity (Figure 9.2 and 9.5). The ground state has an irreducible representation Γ_1 (A_1). Therefore all

transitions are allowed by an electric dipole mechanism [153]. Transitions from the ground state into Γ_1 (A_1) or Γ_4 (B_2) are dipole allowed, whereby the intensities of the transitions into Γ_2 (B_1) or Γ_3 (A_2) are zero [155].

Absorption spectra and line sntregths of UP_2O_7 [154]. and $(U_2O)(PO_4)_2$ [149]. were calculated with parameter sets matching the parametrization of UPO_4Cl (see Figure 9.6). These results are in fair agreement with the observed absorption spectra.

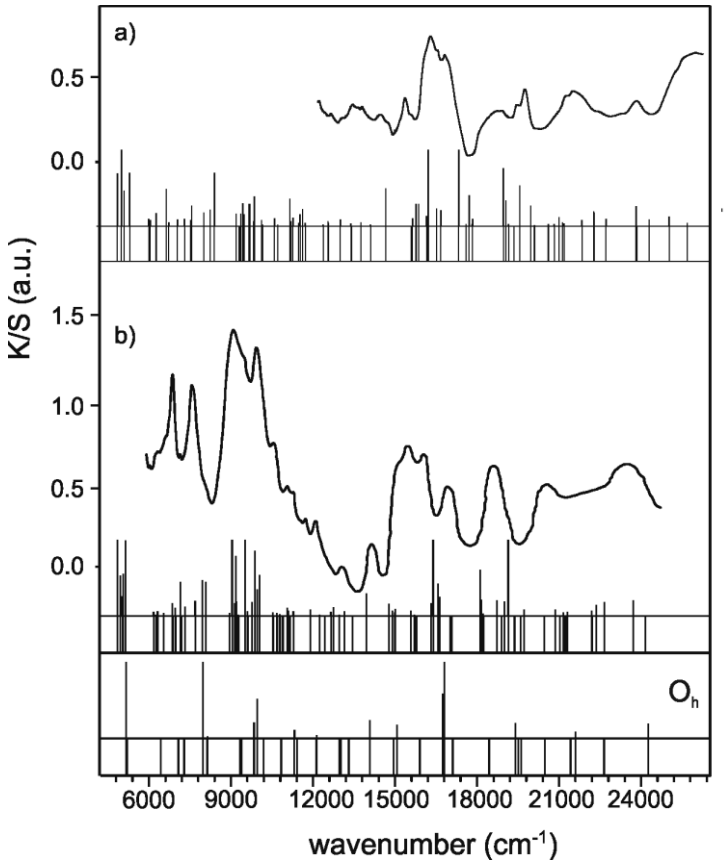

Figure 9.6. Absorption spectra of UP_2O_7 [124] (b) and $(U_2O)(PO_4)_2$ [149] (a). Angular overlap modeling (zero-phonon lines) with estimated relative intensities (according to Judd-Ofelt theory) for the real symmetry and ideal octahedron.

The last parameters which were varied are the spin-orbit coupling constant ζ and Stevens-orbital reduction factor *k*. The spin-orbit coupling constant taken from literature leads to the best fit between calculated and observed magnetic susceptibilities. In order to improve the agreement between the calculated and the experimental magnetic data the Stevens-orbital reduction factor *k* was reduced to 95%. For a consistency check of the used parameter set several calculations of the effective Bohr magneton number μ_{eff} as function of the temperature with two values for *k* were performed. In Figure 9.7a/b/c comparison between results obtained

with k = 1.0, k = 0.95 and k = 0.9 is shown. For k = 1.0 (see Figure 9.7a) the calculated moments are larger, for k = 0.9 smaller than the measured ones.

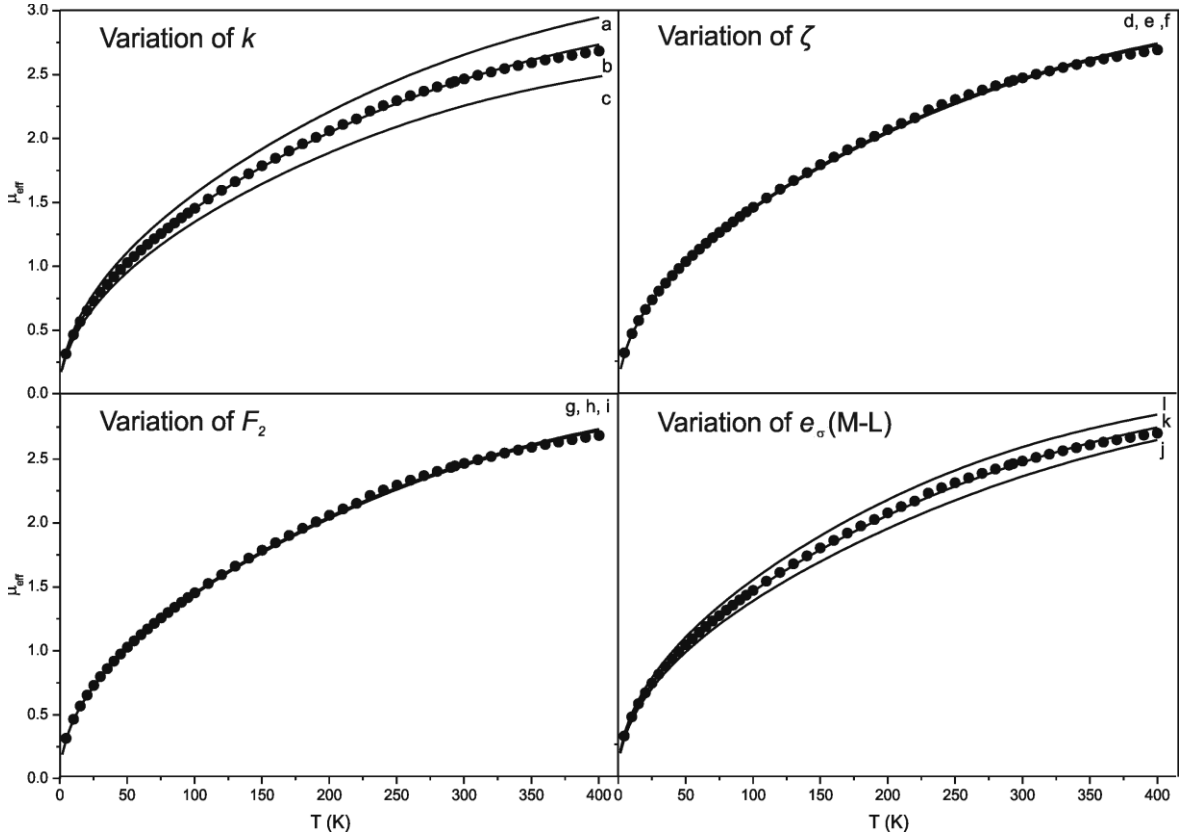

Figure 9.7. Graphical representation of the measured effective Bohr magneton number μ_{eff} (arb. units) vs. T (K) for UPO_4Cl and comparison to the calculated μ_{eff} (solid lines). a) k = 1.0, b) k = 0.95 (best fit), c) k = 0.90, d) ζ = best fit + 5%, e) best fit , f) ζ = best fit - 5%, g) F_2 = best fit values +5%, h) best fit, i) F_2 = best fit values –5%, j) e_σ = best fit values +10%, k) best fit, l) e_σ = best fit values –10%.

As already mentioned the best fit for the absorption coefficients was obtained by reducing the third Judd-Ofelt parameter Ω_6 from $4.529 \cdot 10^{-24}$ m^2 (for Pr^{3+} [90]) to $0.4529 \cdot 10^{-24}$ m^2 for the U^{4+} ion. Parameters $\Omega_2 = 1.078 \cdot 10^{-24}$ m^2 and $\Omega_4 = 2.014 \cdot 10^{-24}$ m^2 (also from Pr^{3+}) were kept unchanged. Only by decreasing parameter Ω_6 with respect to the literature, value for Pr^{3+} a good fit of the calculated to the experimental line strength was achieved. Variation of Ω_2 or Ω_4 does not change the relative line strengths of the absorption coefficients and has only a scaling effect. Only variation of Ω_6 allowed adjusting of the relative magnitudes of the line strengths ("absorption coefficients"). Our calculations show that many of the calculated transitions have no intensity within Judd-Ofelt theory. Thus, the intensity criterion is essential for the assignment of the observed transitions.

The variation procedures show, that these parameters cannot be arbitrarily selected or changed. Based on the combination of absorption spectra and magnetic measurement a reliable parameter set is found.

9.3 Discussion of obtained AOM parameters

For Cs_2UCl_6 (chromophore $[U^{IV}Cl_6]$) with d(U-Cl) = 2.621 Å [155] the interaction parameters e_σ(U-Cl) = 1489 cm^{-1} and $e_{\pi,iso}$(U-Cl) = 338 cm^{-1} [156] have been reported. Using BonnMag with these parameters the energy levels for the chromophore $[U^{IV}Cl_6]$ have been calculated and compared to those observed and calculated by SATTEN [150] (see Table A3). The two sets of calculated energies fit perfectly, thus demonstrating the compliance of the two calculations. For UO_2 (chromophore $[U^{IV}O_8]$) with an uranium-oxygen distance d(U-O) = 2.3729 Å energies e_σ(U-O) = 1908 cm^{-1} have been obtained by GAJEK and MULAK. In case of U^{4+} doped in $ThSiO_4$ $e_\sigma(U\text{-}O)_{2.417\ Å}$ = 1650 cm^{-1} has been reported [[157, 158, 159, 160]. In contrast, transfer of e_σ(U-O) obtained for UPO_4Cl suggests about 30% smaller parameters e_σ(U-O) = 1236 cm^{-1} for UO_2 and e_σ(U-O) = 1086 cm^{-1} for U^{4+} in $ThSiO_4$. Reasons for this differences are not yet clear.

Calculations with variation of the ratio e_π/e_σ = 0.15, 0.25, and 0.35 showed no significant influence of the assumed magnitude of the π-interaction on the magnetic moment per U^{4+} and the excited state energies. An accurate characterization of the ground state splitting by ligand field effects, e.g. by Resonance Raman spectroscopy [161] might allow or even require a more detailed description of the π-interaction, though.

The AOM parameters of U^{4+} in UPO_4Cl are about five times larger than the typical values for Pr^{3+} and significantly smaller than those for transition metals.

9.4 Extraction of ligand field splitting from the AOM calculation

The splitting of the *f* orbitals caused by the various ligand fields is calculated from the AOM parameters e_σ and e_π of the $[U^{IV}O_6Cl_2]$ chromophore and their effect on an f^1 system (Figure 9.8). For these calculations, the Slater-Condon-Shortley parameters as well as the spin-orbit coupling constant were set to zero. Due to the low symmetry (C_{2v}) of the $[U^{IV}O_6Cl_2]$ chromophore in UPO_4Cl the degeneracy of the seven *f* orbitals is lifted completely. In the same way the splitting of the *f* orbitals by an ideally octahedral $[U^{IV}O_6]$ chromophore, the $[U^{IV}O_6]$ chromophore with slight angular distortion in UP_2O_7 and the $[U^{IV}O_7]$ chromophore in $(U_2O)(PO_4)_2$ have been calculated (Figure 9.8). The influence of the small angular distortions

(89.5 ° ≤ ∠(O,U,O) ≤ 90.5 °) of the [$U^{IV}O_6$] chromophore in UP_2O_7 is quite remarkable and leads to the complete removal of the orbital degeneracy compared to the ideal octahedron (see Figure 9.8).

By using the definition of the ligand field strength given by Wybourne [162] (Equation 9.2) Δ for UPO_4Cl, UP_2O_7 (real and ideal geometry) and $(U_2O(PO_4)_2$ was calculated: $\Delta(UPO_4Cl)$ = 3536 cm^{-1}, $\Delta(UO_6$, ideal) = 4081 cm^{-1}, $\Delta(UP_2O_7$, real) = 4143 cm^{-1}, $\Delta((U_2O(PO_4)_2)$ = 5391 cm^{-1}. The Wybourne parameters used for these calculations were obtained from the AOM parameters in BonnMag. The smallest Δ is observed for UPO_4Cl. Typical values for the ligand field splitting of 3*d* metal complexes are Δ = 10000 cm^{-1}. For rare earth elements, this splitting is rather small (Δ ~ 1000 cm^{-1}).

$$S = \left[\frac{1}{3} \sum_k \frac{1}{2k+1} \left((B_0^k)^2 + 2 \sum_{q>0} \left((ReB_q^k)^2 + (ImB_q^k)^2 \right) \right) \right]^{\frac{1}{2}} \qquad \text{Equation 9.2}$$

Δ ligand-field splitting

B_0^k Wybourne parameters with q = 0 and k = 2, 4, 6

$Re\,B_q^k$ real part of Wybourne parameters with q = 1-6 and k = 2, 4, 6

ImB_q^k imaginary part of Wybourne parameters with q = 1-6 and k = 2, 4, 6

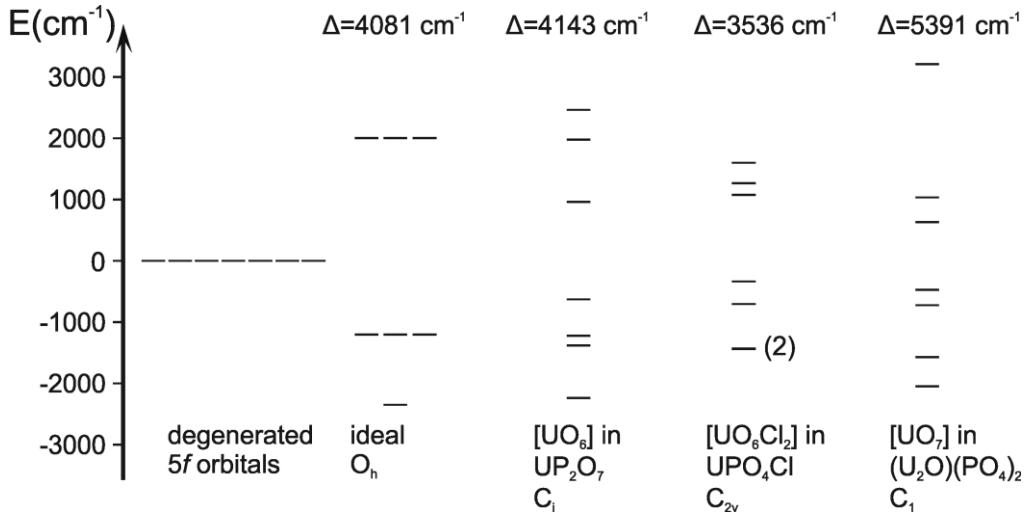

Figure 9.8. Splitting of the *f* orbitals by the chromophores [$U^{IV}O_6$] (O_h symmetry), [$U^{IV}O_6$] in UP_2O_7, [$U^{IV}O_6Cl_2$] in UPO_4Cl, and [$U^{IV}O_7$] in $U_2O(PO_4)_2$ (energies to scale) compared to the ligand field splittings according to Wybourne.

10 Overlap integrals for different coordination polyhedra and ligand-field splitting for *f*-orbitals

For the understanding of the chemical bonding for different metal - ligand interactions the knowledge of the magnitude of the overlap integrals is nessecary. Using program BonnMag it is possible to calculate the angular overlap integrals. Using the direction cosines obtained from the atomic coordinates and the matrix expressing the rotation of a set of metal wavefunctions into the ligand axis frame the angular overlap integral can be calculated. The rotation matrix is reported in Ref. 24. The anti-bonding energy of a given *f*-orbital is writen as

$$E = e_\lambda \cdot (F_\lambda^l)^2 \qquad \text{Equation 5.3}$$

where λ describes the bonding symmetry (σ or π) and F is the angular overlap integral. The F^2 (for σ bonding) and P^2 (for π bonding) values in case of *d*-orbitals are reported by Richardson [63] for different AB_n geometries. Here we present the F^2 and P^2 values for the set of the *f*-orbitals for four different geometries (octahedron, cube, antiprism, triple capped trigonal prism). The positions of the ligands are given in Figure 10.1. Metal atom is at the origin of the coordinate system and the z-axis is along the general rotation axis in the given point group.

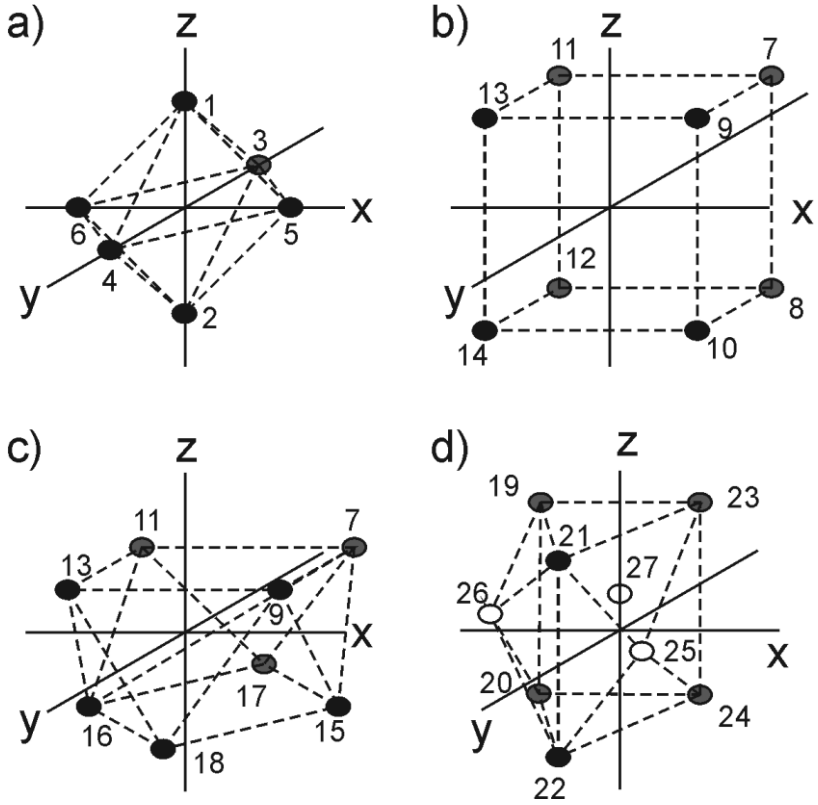

Figure 10.1. Ligand positions for various ML_n geometries. a) octahedron, b) cube, c) antiprism and d) triple capped trigonal prism. Black atoms are in the negative *y* direction (in front), grey atoms in positive *y* direction, white atoms (25-27) the covered atoms of the trigonal prism.

Table 10.1. F^2 values (σ-bonding), *f*-orbitals are defined by their m_l quantum number.

L	0	1	-1	-2	2	3	-3
1	1	0	0	0	0	0	0
2	1	0	0	0	0	0	0
3	0	3/8	0	0	0	5/8	0
4	0	3/8	0	0	0	5/8	0
5	0	0	3/8	0	0	0	5/8
6	0	0	3/8	0	0	0	5/8
7	0.1481	0.1111	0	0.5556	0	0.1852	0
8	0.1481	0.1111	0	0.5556	0	0.1852	0
9	0.1481	0	0.1111	0.5556	0	0	0.1852
10	0.1481	0	0.1111	0.5556	0	0	0.1852
11	0.1481	0	0.1111	0.5556	0	0	0.1852
12	0.1481	0	0.1111	0.5556	0	0	0.1852
13	0.1481	0.1111	0	0.5556	0	0.1852	0
14	0.1481	0.1111	0	0.5556	0	0.1852	0
15	0.1481	0.0556	0.0556	0	0.5556	0.0926	0.0926
16	0.1481	0.0556	0.0556	0	0.5556	0.0926	0.0926
17	0.1481	0.0556	0.0556	0	0.5556	0.0926	0.0926
18	0.1481	0.0556	0.0556	0	0.5556	0.0926	0.0926
19	0.0313	0.4219	0	0.4687	0	0.0781	0
20	0.0313	0.4219	0	0.4687	0	0.0781	0
21	0.0313	0.1065	0.3164	0.1172	0.3516	0.0781	0
22	0.0313	0.1065	0.3164	0.1172	0.3516	0.0781	0
23	0.0313	0.1065	0.3164	0.1172	0.3516	0.0781	0
24	0.0313	0.1065	0.3164	0.1172	0.3516	0.0781	0
25	0	3/8	0	0	0	5/8	0
26	0	0.0938	0.2812	0	0	5/8	0
27	0	0.0938	0.2812	0	0	5/8	0

Table 10.2. P^2 values (for π_x bonding), *f*-orbitals are defined by their m_l quantum number.

L	0	1	-1	-2	2	3	-3
1	0	1	0	0	0	0	0
2	0	1	0	0	0	0	0
3	3/8	0	0	5/8	0	0	0
4	3/8	0	0	5/8	0	0	0
5	3/8	0	0	5/8	0	0	0
6	3/8	0	0	5/8	0	0	0
7	0.1111	3/4	0	0	0	0.1389	0
8	0.1111	3/4	0	0	0	0.1389	0
9	0.1111	0	3/4	0	0	0	0.1389
10	0.1111	0	3/4	0	0	0	0.1389
11	0.1111	0	3/4	0	0	0	0.1389
12	0.1111	0	3/4	0	0	0	0.1389
13	0.1111	3/4	0	0	0	0.1389	0
14	0.1111	3/4	0	0	0	0.1389	0
15	0.1111	0.3749	0.3749	0	0	0.0694	0.0694
16	0.1111	0.3749	0.3749	0	0	0.0694	0.0694
17	0.1111	0.3749	0.3749	0	0	0.0694	0.0694
18	0.1111	0.3749	0.3749	0	0	0.0694	0.0694
19	0.4219	0.3828	0	0.0781	0	0.1172	0
20	0.4219	0.3828	0	0.0781	0	0.1172	0
21	0.4219	0.0957	0.2817	0.0195	0.0586	0.1172	0
22	0.4219	0.0957	0.2817	0.0195	0.0586	0.1172	0
23	0.4219	0.0957	0.2817	0.0195	0.0586	0.1172	0
24	0.4219	0.0957	0.2817	0.0195	0.0586	0.1172	0
25	3/8	0	0	5/8	0	0	0
26	3/8	0	0	0.1562	0.4687	0	0
27	3/8	0	0	0.1562	0.4687	0	0

Table 10.3. P^2 values (for π_y bonding), *f*-orbitals are defined by their m_l quantum number.

L	0	1	-1	-2	2	3	-3
1	0	0	1	0	0	0	0
2	0	0	1	0	0	0	0
3	0	0	5/8	0	0	0	15/16
4	0	0	5/8	0	0	0	15/16
5	0	5/8	0	0	0	15/16	0
6	0	5/8	0	0	0	15/16	0
7	0	0	0.0278	0	0.5556	0	0.4167
8	0	0	0.0278	0	0.5556	0	0.4167
9	0	0.0278	0	0	0.5556	0.4167	0
10	0	0.0278	0	0	0.5556	0.4167	0
11	0	0.0278	0	0	0.5556	0.4167	0
12	0	0.0278	0	0	0.5556	0.4167	0
13	0	0	0.0278	0	0.5556	0	0.4167
14	0	0	0.0278	0	0.5556	0	0.4167
15	0	0.0139	0.0139	0.5556	0	0.2083	0.2083
16	0	0.0139	0.0139	0.5556	0	0.2083	0.2083
17	0	0.0139	0.0139	0.5556	0	0.2083	0.2083
18	0	0.0139	0.0139	0.5556	0	0.2083	0.2083
19	0	0	0.1406	0	5/8	0	0.2344
20	0	0	0.1406	0	5/8	0	0.2344
21	0	0.1055	0.0353	0.4687	0.1562	0	0.2344
22	0	0.1055	0.0353	0.4687	0.1562	0	0.2344
23	0	0.1055	0.0353	0.4687	0.1562	0	0.2344
24	0	0.1055	0.0353	0.4687	0.1562	0	0.2344
25	0	0	1/16	0	0	0	15/16
26	0	0.0469	0.0156	0	0	0	15/16
27	0	0.0469	0.0156	0	0	0	15/16

The overlap integral can be used for the understanding of the chemical bonding and ligand-field effect. By summing of the angular part of the overlap integrals for each ligand in the given chromophore the contribution of all *f*-orbitals to σ- and π-bonding is obtained.

Figure 10.2 shows the splitting of the f-orbitals in the four coordination polyhedra given in Figure 10.1. For the four calculations e_σ = 200 cm^{-1} as well as the ratio e_π/e_σ = 1/4 is used. The largest splitting is obtained for the cubic and the smallest splitting for the antiprismatic coodination sphere.

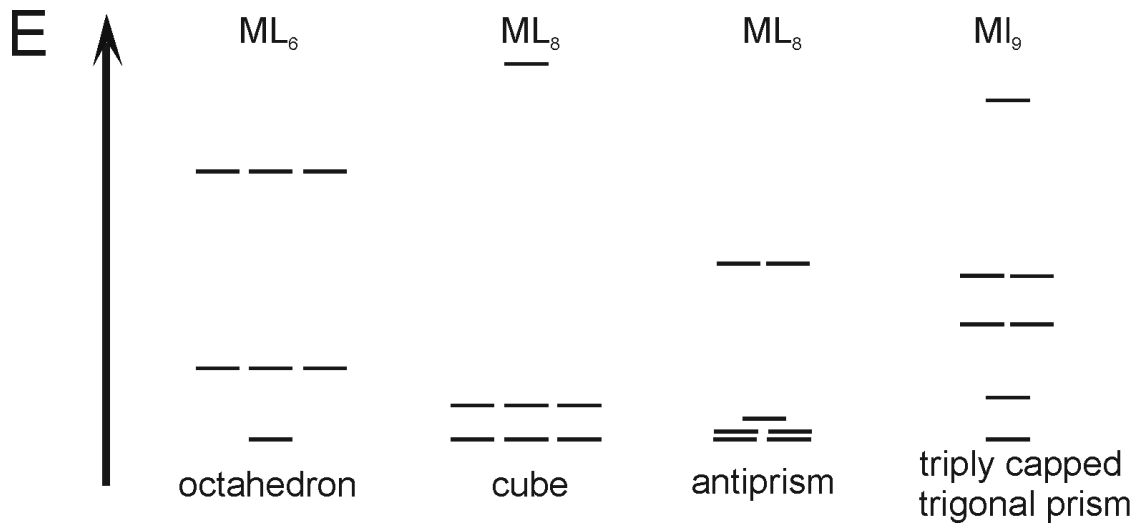

Figure 10.2. Splitting of the *f*-orbitals for octahedral, cubic, antiprismatic polyhedra and 9-fold coordination in a triple capped trigonal prism.

11 Conclusion and outlook

In this thesis the development and application of the computer program BonnMag are described. BonnMag allows calculation of the electronic transition states, magnetic susceptibilities, crystal susceptibilities, temperature dependency of the magnetic moment, *g* tensors (for odd number of electrons) for all f^n systems within the framework of the angular overlap model. In addition to the calculation of the electronic transition states *J* projections of the parental states are determined from the eigenvectors. This procedure allows the unambiguous assignment of the parental states to their split states as well as the statement about the configuration interactions for split states having contributions from several parental states. For an improved analysis of the experimental data estimation of the absorption coefficients is implemented in BonnMag using the Judd-Ofelt theory.

In contrast to *d*-orbitals the shape of the *f*-orbitals is rather difficult to describe the overlap of the metals *f*-orbitals with the ligand orbitals. Thus, the implemented calculation of the angular part of the overlap integral allows better analysis of the bonding situation in considered compounds. For four different coordination polyhedra (octahedron, cube, squared antiprism and triple covered trigonal prism) the angular part of the overlap integrals as well as the splitting of the *f*-orbitals (using the assumption $e_{\pi,x} = e_{\pi,y} = 0.25e_{\sigma}$) were calculated similar to those for d^n systems reported by Richardson [63].

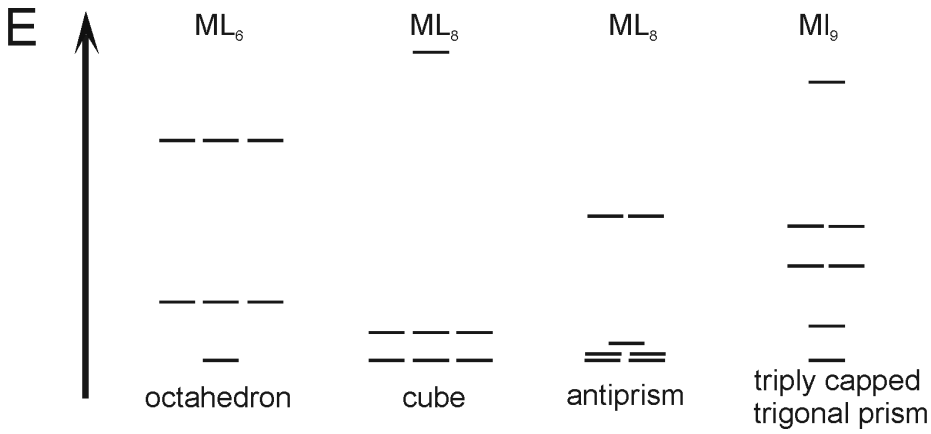

Splitting of the *f*-orbitals for octahedral, cubic, antiprismatic polyhedra and 9-fold coordination in a triple capped trigonal prism.

Several f^n systems were modeled using BonnMag to show the possibilities and limits of AOM.

At first the quality of the calculations using BonnMag was checked and compared to the results of complex *ab initio* calculations. Using the Slater-Condon-Shortley parameters and

spin-orbit coupling constant from CASSCF and NEV-PT2 the energies of all **free Ln^{3+}** ions were calculated. The results obtained by BonnMag are in good agreement with the energies from the *ab initio* calculations. The simple parametrization of the free ion applied in BonnMag describes the energy states not as well as modeling using higher order parameters. For better description of the free ions those complex parametrizations are needed. Nevertheless, the description of the ligand-field influence, which is nearly independent from the description of the free ions, can be modeled using BonnMag with rather good accuracy which was shown on the series of elpasolites $Cs_2NaLnCl_6$ as example for high-symmetry chromophores.

The same modeling procedure was applied to **$Nd_2Hf_2O_7$**. The presented AOM calculations provide a good match to the observed magnetic susceptibilities, transition energies, and (relative) absorption coefficients of the $[Nd^{III}O_8]$ chromophore in $Nd_2Hf_2O_7$.

As further example for the usefulness and accuracy detailed ligand-field analyses within the framework of MO theory with chemically meaningful parameters have been successfully performed for a series of **europium(III) oxo-compounds including *C*-type Eu_2O_3**. The ligand-field analysis for *C*-type Eu_2O_3 not only accounts for the two quite different chromophores $[Eu1O_6]$ and $[Eu2O_6]$ but would be impossible without this differentiation. Such a simplification was suggested several times in literature. The analysis of the various (mostly low-symmetry) ligand-fields around the Eu^{3+} ions show that the angular part of the ligand-field is nicely accounted for by the AOM approach. The radial part, as described by the magnitude of $e_\sigma(Eu^{3+}\text{-}O)$ depends to a good approximation on the distances $d(Eu^{3+}\text{-}O)^{-7.0}$. In addition, an unexpectedly strong influence of the second coordination sphere (next-nearest cations) on $e_\sigma(Eu^{3+}\text{-}O)$ has been discovered. This effect can be attributed to variation of the electronic polarizability of oxygen $\alpha(O^{2-})$. Qualitatively, this influence might be correlated to the optical basicity Λ of the various europium(III) oxo-compounds ($e_\sigma(Eu^{3+}\text{-}O) \sim \Lambda$).

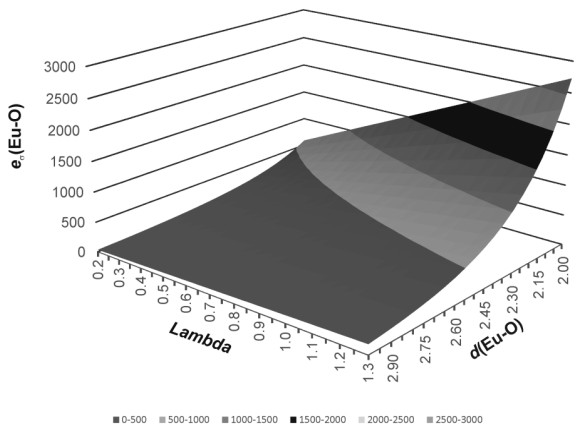

Dependence of e_σ(Eu-O) on *d*(Eu-O) and optical basicity Λ.

The modeling of the electronic transition energies and magnetic moments for the $[U^{IV}O_6Cl_2]$ chromophore in **UPO_4Cl** demonstrate the versatility and power of the new computer program BonnMag. The significance of the AOM parameters obtained for UPO_4Cl has been assessed by variation of each parameter within chemically reasonable limits. Matching the results of AOM simultaneously against observed absorption spectra and magnetic susceptibilities puts rather narrow limits to the parameter space. Using the symmetry analysis and estimated absoprtion coefficients the assignment of the observed bands to the calculated energies can be safely done. It is shown, that thus obtained AOM parameters for UPO_4Cl can be transferred to UP_2O_7 and $U_2O(PO_4)_2$.

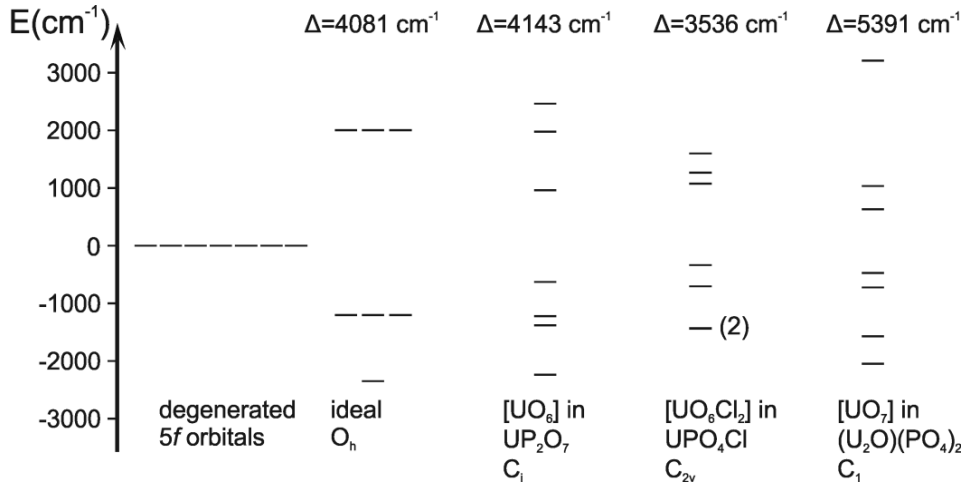

Splitting of the *f*-orbitals by the chromophores $[U^{IV}O_6]$ (O_h symmetry), $[U^{IV}O_6]$ in UP_2O_7, $[U^{IV}O_6Cl_2]$ in UPO_4Cl, and $[U^{IV}O_7]$ in $U_2O(PO_4)_2$ (energies to scale) compared to the ligand field splittings according to Wybourne.

Within the ongoing development of the computer program **BonnMag further options** will be included. The calculation of the Mössbauer parameters, field-dependant magnetic modeling and least-square fitting should be implemented in BonnMag for wide-ranging application on different f^n systems.

The investigations of the chemical bonding between Eu^{3+} and oxygen should be continued. Characterization of synthetically slightly more demanding compounds like the highly basic oxide $BaEu_2O_4$ and the rather acidic sulfate $Eu_2(SO_4)_3$ would be very welcome to provide an extended experimental base for the suggestion of a close relation between $e_\sigma(Eu^{3+}\text{-}O^{2-})$ and the optical basicity of a multinary oxide. Following this reasoning experimental data on the polarizability of the oxygen atoms in multinary europium(III) oxides (from measurements of dielectric constants) would also be of high interest to a more detailed understanding of chemical bonding between the chemical environment and Eu^{3+} in particular and Ln^{3+} in

general. Similar series of oxo-compounds of other Ln^{3+} should be investigated for clarification of the analogies and differences in the bonding situation along the lanthanide series. In addition to the oxo-compounds ligand-fields including nitrogen (nitrides), phosphorus (phosphides), and sulfur (sulfides) should be studied.

In general, the ligand-field effects are very important for the description of the optical and magnetic properties as shown in this thesis. Those investigations are of major importance for the development of the single-molecular or single-ion magnets and luminiscent materials. Modelling of the ligand-fields with those effects should build the basis for the further investigations in this research field.

12 Appendix

12.1 BonnMag User Manual (Version 1.3, 01.06.17)

Introduction:

'BonnMag' is a Fortran 90 computer program which calculates symmetry assigned energy levels, g-values, electric dipole intensities and magnetic susceptibilities of all rare-earth ions. This program is based on the program 'SURGEV' written by W. Urland [60].

The program contains two input parts, 'setup' and 'run'. In 'setup' all input data which are not dependent on particular parameter values are specified (coordinates of all considered atoms, cell parameters). The second data file 'run' contains all parameters used for the ligand-field calculation (interelectron repulsion and ligand field perturbations as Condon-Shortley-parameters, spin-orbit coupling etc.)

The program also produces data files called f_*.out where an asterisk * indicates the number of *f* electrons. The files f_*.out contain the reduced matrix elements which have been taken from Reference [67] . These files are automatically generated by BonnMag during the calculation.

After the calculation the data file 'OUTPUT' is generated, where all parameters and calculated values are located.

Note: The input data files can be called 'setup' and 'run' and will be automatically read by BonnMag if they are located in the actual subdirectory. In this case the output data file is called 'OUTPUT'. If the input data files have different name, the user will be asked to provide the names of these files. The names of both files should be different. The output data file gets the name *.out where * is the name of the 'run' part.

Example: 'setup' is called 'PrZnPO'

'run' is called 'PrZnPO-01' (**Attention!** Use different names)

output data file gets the name 'PrZnPO-01.out'

The input commands:

In the input files each line is called a command. These commands control the extent of the calculations performed by the program. The first four characters (except command TITLE) in each line identify the command, while columns 5-72 are used to convey numerical data. The

data must be separated by spaces. All numbers should be given with one or more decimal places even if it is zero.
The commands in the file RUN can be given in any order unless stated otherwise. In SETUP the commands should be in the specified order (see apendix).

*** An asterisk indicates that the command is compulsory.**

SETUP

Allowed commands:
CELL CONF END LGND MULT PRTL TITLE XREF & "atomic coordinates"

* 'CELL' a b c alpha beta gamma

Unit cell parameters in Angstroms and degrees.

* 'CONF' m

m = number of electrons, $1 \leq m \leq 14$ for f electrons.

* 'END'

This must be the last command.

* 'LGND' m n n1 n2 n3

Defines a local cartesian reference frame for a ligand in terms of the atoms n1, n2, n3 in the atom list. n1, n2, and n3 refer to the atom number in the listing in the input file! The Z axis is parallel to n1 and n2. The Y axis is perpendicular to the plane defined by the 3 atoms. The X axis will form a right-handed coordinate system.
'n' is the ligand type number (ligands with equal bonding parameters e_δ and e_π get the same ligand typ number).
'm' is a ligand number (1-number of ligands).

Note: There must be at least 2 'LGND' commands.

An error will occur if n1, n2, n3 are collinear.

* 'MULT' n

n =1 if there is no center of inversion.

n =2 if there is a center of inversion, in this case only noncentrosymmetric related ligands should be given in the LGND commands.

'PRTL' n

Print level, amount of the output data file is controlled by this command and is not compulsory.

n = 0 (Default value, used if no PRTL keyword is given in SETUP).

Output contains: coordinates of all atoms and distances from each ligand to the metal atom, Slater-Condon-Shortley, spin-orbit and angular overlap,parameters, angular part of the overlap integral, overlap integral, energies with intensities and *J* projections, eigenvectors, magnetic susceptibilities, crystal susceptibilities and g-tensor.

n = 1 additionally: direction cosines for all atoms, crystal field parameters (Wybourne)

n = 2 additionally: Nielson/Koster coefficients, basis set, electrostatic matrices.

* 'TITLE' Title

Title of the calculation (up to 72 characters).

* 'XREF' n1 n2 n3

Defines a global cartesian reference frame in terms of the atoms n1, n2, n3. The Z axis will be in the n2→n1 direction. The Y axis will be perpendicular to the plane defined by the 3 atoms. The X axis will form a right-handed coordinate system.

Note: If symmetry analysis should be done, the Z axis has to coincide with the main rotation axis of the given point group! If there is no atom in the chromophor which fulfills this condition a dummy atom has to be introduced. Otherwise the obtained eigenvalues may be wrong.

* 'Atom commands' x/a y/b z/c

Each atom command starts with up to 4 characters to identify the atom (for the same atoms numbering can be used as like as 'O1'), then the three fractional coordinates with respect to *a, b, c* of the cell command. There must be at least 3 'atom commands'.

Note: Dummy atoms or atoms from a second coordination sphere have to be defined by the character 'X'. The atoms defined by 'X' are not included into the interia tensor calculation.

RUN:

Allowed commands (bold face) and parameters:

EORF EPIX EPIY ESIG **GTEN** JOPS KVAL **LATT MAGN MOLS NVEC** REFR SCSZ **SYML TEMP VLEC**

* 'EORF' n

n = 0 the Slater-Condon-Shortley parameters in RUN are given as E_1, E_2, E_3.
n = 1 the Slater-Condon-Shortley parameters in RUN are given as F_2, F_4, F_6.
(see SCSZ)

* 'ESIG' / 'EPIX' / 'EPIY' } Repeated for each of the n different ligand types

Angular overlap parameters or interaction energies. ESIG = e_σ, EPIX = $e_{\pi,x}$, EPIY = $e_{\pi,y}$. If isotropic π-interaction is assumed the values for EPIX and EPIY should be equal. If π-interaction is zero then it should be given for all ligand types as 0.0. For anisotropic π-interaction EPIX and EPIY can be different for each ligand type.

* 'GTEN' n

n = 0 g-values will not be calculated.
n = 1 g-values will be calculated in appropriate crystal planes.

Note: g-values calculation can be performed just for ions with odd numbers of f-electrons! For ions with even number of f-electrons the calculation result is zero and is wrong!

'JOPS' Ω_2 Ω_4 Ω_6.

Judd-Ofelt-Parameters in m^2 for calculation of intensities of electric dipole transitions.

This command is not compulsory. If no Judd-Ofelt parameters are given in 'RUN' default values for rare-earth ions in LaF_3 will be used [90].

Table 1. Judd-Ofelt parameters for rare-earth ions in LaF_3 [90].

Ion	**Ω_2 (10^{-24} m^2)**	**Ω_4 (10^{-24} m^2)**	**Ω_6 (10^{-24} m^2)**
Ce^{3+}	1.868	3.996	10.61
Pr^{3+}	1.078	2.014	4.529
Nd^{3+}	0.944	1.322	2.486
Pm^{3+}	0.632	1.012	1.910
Sm^{3+}	0.561	0.867	1.580
Eu^{3+}	0.444	0.651	1.119
Gd^{3+}	0.346	0.480	0.774
Tb^{3+}	0.660	1.020	1.865
Dy^{3+}	0.477	0.686	1.159
Ho^{3+}	0.387	0.530	0.846
Er^{3+}	0.375	0.506	0.798
Tm^{3+}	0.368	0.493	0.771
Yb^{3+}	0.309	0.397	0.587

* 'KVAL' k1 k2 k3 etc.

Stevens-orbital reduction factor k ($k \leq 1.0$) reduces the results of magnetic values and g-tensors and is similar to the nephelauxetic ratio β for reducing of Condon-Shortley parameters. It can be varied inside the subroutines which calculate g-values and magnetic susceptibilities. This is helpful for a series of calculations where *k* values are varied. The number of given *k* values corresponds to the number of performed calculations.

* 'LATT' n

Defines the crystal system.

n = 0 crystal susceptibilities will not be calculated.

n = 1 Monoclinic.

n = 2 Orthorhombic.

n = 3 Tetragonal or hexagonal.

Compulsory for GTEN command.

* 'MAGN' n

n =0 magnetic susceptibilities will not be calculated.

n =1 magnetic susceptibilities will be calculated (necessary in case of g-tensor calculation).

* 'MOLS' n

Indicates nature of molecular symmetry. If higher symmetry is given, the calculation of magnetic susceptibilities would be proceed just for unequal directions. Equal directions would get the same results. (For example, if molecular symmetry is cubic the calculation of magnetic susceptibilities would be made one time for one direction).

n = 1 Cubic.

n = 2 Axial.

n = 3 Rhombic

n = 4 Lower symmetry.

* 'NVEC' n

n = 0 No eigenvectors are listed.

n = 1 All eigenvectors are listed.

n = N Lowest N of eigenvectors are listed.

'REFR' n

n = Refraction index used for the Judd-Ofelt analysis (intensity calculations). If no refraction index is given in RUN and intensities will be calculated, the default value of n = 1.8 is used [L. Zundu, C. Xueyuan, Z. Tingjie, *Opt. Commun*., **1997**, *134*, 415].

* 'SCSZ' $F_2(E_1)$ $F_4(E_2)$ $F_6(E_3)$ Zeta (f^n)

Input of Slater-Condon-Shortley electron repulsion parameters F_2, F_4, F_6 (f^n) in cm^{-1} and spin-orbit coupling constant. Zeta is *not* reduced by *k* (Stevens-orbital-reduction factor). These parameters must be explicitly reduced in the input.

The parameters can be taken from the following table

Table 1. Free ion SCS and spin-orbit coupling parameters obtained from NEV-PT2 (F_2, F_4, F_6) and CASSCF (ζ) calculations in cm^{-1} (see text).

Ln^{3+}	F_2	F_4	F_6	ζ	Ln^{3+}	F_2	F_4	F_6	ζ
Ce	0.0	0.0	0.00	685.4	Gd	399.1	58.4	6.52	1576.0
Ce[a)]	0.0	0.0	0.00	643.7	Tb	414.2	59.4	6.69	1761.7
Pr	324.2	52.1	5.25	802.2	Dy	427.6	61.5	6.93	1964.3
Pr[a)]	325.4	51.7	5.23	764.0	Ho	440.8	64.1	7.08	2182.5
Nd	342.7	49.9	5.60	936.2	Ho[a)]	414.6	68.8	7.27	2163.0
Pm	356.6	52.1	5.83	1075.9	Er	454.2	65.7	7.37	2417.5
Pm[a)]	346.2	47.7	5.23	1070.0	Tm	467.4	69.9	7.60	2671.3
Sm	371.8	53.9	6.07	1231.3	Yb	0.0	0.0	0.00	2935.6
Eu	386.1	55.6	6.26	1395.4	Yb[a)]	0.0	0.0	0.00	2918.3
Eu[a)]	401.0	55.4	6.06	1320.0					

'SYML' n

The calculation of symmetry labels (irreducible representation = irrep) in the point group 'n' ($0 < n \leq 32$). 'n' corresponds to the numbering in the tables of Koster et al. [G. F. Koster, J. O. Dimmock, R. G. Wheeler and H. Statz, *"Properties of the 32 point groups"*, MIT Press, **1963**].

1 C_1 (1)	9 C_4 (4)	17 C_{3i} / S_6 ($\bar{3}$)	25 C_{6v} (6*mm*)
2 C_i ($\bar{1}$)	10 S_4 ($\bar{4}$)	18 D_3 (32)	26 D_{3h} ($\bar{6}m2$)
3 C_2 (2)	11 C_{4h} (4/*m*)	19 C_{3v} (3*m*)	27 D_{6h} (6/*m2/m2/m*)
4 C_2 (*m*)	12 D_4 (422)	20 D_{3d} ($\bar{3}2/m$)	28 T (23)
5 C_{2h} (2/*m*)	13 C_{4v} (4*mm*)	21 C_6 (6)	29 T_h (2/m$\bar{3}$)
6 D_2 (222)	14 D_{2d} ($\bar{4}2m$)	22 C_{3h} ($\bar{6}$)	30 O (432)
7 C_{2v} (*mm*2)	15 D_{4h} (4/*mmm*)	23 C_{6h} (6/*m*)	31 T_d ($\bar{4}3m$)
8 D_{2h} (2/*m2/m2/m*)	16 C_3 (3)	24 D_6 (622)	32 O_h (4/m$\bar{3}$2/*m*)

In the output data file the Bethe notation is used for irreducible representations. This command is not compulsory. If SYML is not given in the input file 'RUN' no symmetry analysis will be done.

* 'TEMP' a b c

Limits for temperature range (in K).

a: Lowest temperature.

b: Highest temperature.

c: Number of temperature values in the given range which will be considered for the calculation of magnetic susceptibilities.

* 'VLEC' a b c

Energy limits (in cm^{-1}) for the susceptibility calculations.

a: Cutoff for levels in the 2nd order Zeeman summation.

b: Cutoff for levels in the 1st order Zeeman summation.

c: Energy cutoff for levels to be considered degenerate.

Note: The limit given by "c" also determines when 2 or more levels are considered degenerate when the energy levels are printed.

For calculations till 300 K following limits can be used a = 12000 cm^{-1} and b = 3000 cm^{-1}. For higher temperatures the limit for the 1st Zeeman summation has to be increased till the values for magnetic suceptibilities do not change.

12.2 Supporting Information

7.2.1 Uranium(IV) phosphate chloride

Table A1. "Best-fit parameters" for the angular overlap modeling of the $[U^{IV}O_6]$ chromophore in UP_2O_7.

Slater-Condon-Shortley parameters (cm^{-1})

F_2 = 190.9 F_4 = 33.74 F_6 = 3.99675 ($\beta = F_2 / F_{2,\,f.i.}$ = 0.82)

Slater-Condon-Shortley parameters of the free U^{4+} ion (cm^{-1})

$F_{2,\,f.i.}$ = 234.73 $F_{4,\,f.i.}$ = 41.35 $F_{6,\,f.i.}$ = 4.10

Spin-orbit coupling constant (cm^{-1})

ζ = 1797.02

Interaction parameters e_m(U-O) (m: σ, π)

Ligand	Distance (Å)	e_σ (cm^{-1})	$e_{\pi,iso}$ (cm^{-1})	e_π / e_σ
O1	2.243	1832	458	0.25

Judd-Ofelt parameters (10^{-24} m^2)

Ω_2 = 1.078 Ω_4 = 2.014 Ω_6 = 0.4529

Table A2. "Best-fit parameters" for the angular overlap modeling of the $[U^{IV}O_7]$ chromophore in $U_2O(PO_4)_2$.

Slater-Condon-Shortley parameters (cm^{-1})

F_2 = 190.9 F_4 = 33.74 F_6 = 3.99675 ($\beta = F_2 / F_{2,\,f.i.}$ = 0.82)

Slater-Condon-Shortley parameters of the free U^{4+} ion (cm^{-1})

$F_{2,\,f.i.}$ = 234.73 $F_{4,\,f.i.}$ = 41.35 $F_{6,\,f.i.}$ = 4.10

Spin-orbit coupling constant (cm^{-1})

ζ = 1797.02

Interaction parameters e_m(U-O) (m: σ, π)

Ligand	Distance (Å)	e_σ (cm^{-1})	$e_{\pi,iso}$ (cm^{-1})	e_π / e_σ
O3	2.080	3107	777	0.25
O4	2.236	1873	468	0.25
O2	2.258	1749	437	0.25
O1	2.362	1276	319	0.25
O1'	2.514	825	206	0.25

Judd-Ofelt parameters (10^{-24} m^2)

Ω_2 = 1.078 Ω_4 = 2.014 Ω_6 = 0.4529

Table A3. Comparison of calculated (BonnMag, literature) and observed transition energies for the chromophore $[U^{IV}Cl_6]$ in Cs_2ZrCl_6.

$E_{calc.}$ (BonnMag) (cm^{-1})	$E_{calc.}$ (cm^{-1})	$E_{obs.}$ (cm^{-1})	$E_{calc.}$ (BonnMag) (cm^{-1})	$E_{calc.}$ (cm^{-1})	$E_{obs.}$ (cm^{-1})
860	859	915	13158	13154	
1178	1177		13169	13165	12984
2297	2296		14588	14600	14789
4855	4860		15517	15522	15213
5020	5024	5060	15608	15616	15754
6277	6272	6343	16289	16307	
7036	7032		16826	16849	16797
7109	7107		17035	17049	
7794	7791	8197	17536	17540	
8274	8278	8469	18832	18857	18823
9236	9236		19964	19980	
9299	9299		20015	20034	
9736	9735	9540	20066	20083	
9898	9898		21051	21073	
10051	10052	10065	21775	21796	
10910	10908		21953	21975	
11309	11305	11176	23307	23327	23399
11336	11334		24740	24758	24700
12072	12066	12128	41550	41621	
12803	12798	12878			

Table A4. UPO_4Cl. Calculated and observed transition energies, line strengths (LS) with assignment of the parental terms for the region between 0 and 26000 cm^{-1} (measured transition are above 5010 cm^{-1}) for UPO_4Cl. Irreducible representations are given for split terms of the ground state and for the range 8000-11000 cm^{-1}.

Parental term*	$E_{calc.}$ (cm^{-1})	$E_{obs.}$ (cm^{-1})	$LS_{calc.}$	$LS_{obs.}$	Irred. Repr.
$^3P_2$	24619.		0.4924		
$^3P_2$	23794.		0.0000		
$^3P_2$	23119.		0.2068		
$^3P_2$	23083.	23248	0.3046	0.42	
$^3P_2$	22995.	23043	0.0000	0.25	
$^1I_6$	21840.	22283	0.2715	1.48/0.95	
$^1I_6$	21838.		0.0000		
$^1I_6$	21325.		0.3188		
$^1I_6$	21276.	21527	0.1847	0.32	
$^1I_6$	20844.	21287	0.0000	0.68	
$^1I_6$	20426.	20607	0.0000	0.50	
$^1I_6$	20039.		0.0000		
$^1I_6$	19965.		0.6501		
$^1I_6$	19897.	20327	0.1581	0.54	
$^1I_6$	19755.	19892	0.0000	0.29	
$^1I_6$	19727.	19651	0.0000	0.23	
$^1I_6$	19687.		0.2166		
$^1I_6$	19633.		1.0962		
$^3P_1$	18687.		0.0000		
$^3P_1$	18580.		0.6753		
$^3P_1$	18285.	18691	0.0000	0.72	
$^1G_4$	17409.	17375	0.0629	0.31	
$^1G_4$	17058.	17175	0.3062	0.20	
$^1G_4$	16983.	17015	0.0000	0.28	
$^1G_4$ ($^1D_2$)	16875.		0.0000		
$^1D_2$ ($^1G_4$)	16783.	16665	0.4375	0.11	
$^1D_2$ ($^3P_0$)	16240.	16340	2.8457	0.40	
$^1D_2$	16076.		0.9821		
$^1D_2$	16021.		0.0000		
$^1D_2$	15872.	15940	0.9832	1.16	
$^1G_4$	15847.	15660	0.0000	1.03	
$^1G_4$	15496.		0.0235		
$^1D_2$ ($^1G_4$)	15480.	15379	0.0000	0.33	
$^1G_4$	15374.		0.0000		
$^1G_4$	15276.	14979	0.0374	0.34	
$^1G_4$ ($^3P_0$)	14849.	14584	0.0644	0.26	
$^3H_6$	12935.		0.0000		
$^3H_6$	12920.		0.3669		
$^3H_6$	12820.	13183	0.0000	0.32	
$^3H_6$	12782.	12943	0.3386	0.35	
$^3H_6$	12457.		0.0000		
$^3H_6$	12428.		0.1936		
$^3H_6$	12087.	12188	0.2202	0.17	
$^3H_6$	11914.	12068	0.0000	0.32	
$^3H_6$	11213.	11588	0.0000	0.33	
$^3H_6$	11207.	11348	0.4133	0.26	
$^3H_6$	11187.		0.7593		
$^3H_6$	11054.	11152	0.2379	0.36	
$^3H_6$	11034.		0.0000		
$^3F_4$	10673.	10592	0.0000	0.30	Γ_3
$^3F_4$	10523.		0.6527		Γ_4
$^3F_4$	10424.		0.7483		Γ_1
$^3F_4$	10134.	10272	0.0000	0.31	Γ_2

$^3F_4$ ($^3F_3$)	9830.		0.0000		Γ_3
$^3F_3$	9803.	9592	0.0352	0.21	Γ_4
$^3F_3$	9545.		0.0000		Γ_2
$^3F_3$	9451.		0.0000		Γ_2
$^3F_4$	9379.		0.5326		Γ_1
$^3F_3$ ($^3F_4$)	9231.	9316	0.0000	1.70	Γ_3
$^3F_4$ ($^3H_5$)	9152.	9200	0.0000	1.50	Γ_2
$^3F_3$ ($^3F_4$)	9138.	9196	1.9633	1.45	Γ_4
$^3F_3$	9117.	9076	3.7466	1.26	Γ_1
$^3F_4$ ($^3F_3$)	8989.		2.0879		Γ_4
$^3F_3$ ($^3F_4$)	8865.		0.0000		Γ_3
^3F	8593.	8556	0.8633	0.77	Γ_1
$^3H_5$	7561.	7876	0.0000	0.67	Γ_2
$^3H_5$	7359.	7480	0.8567	0.92	Γ_1
$^3H_5$	7112.	7280	0.0000	1.09	Γ_3
$^3H_5$	7111.		0.0000		Γ_2
$^3H_5$	7110.		0.6662		Γ_4
$^3H_5$	7063.	7040	0.8043	1.24	Γ_1
$^3H_5$	6700.		2.0104		Γ_4
$^3H_5$	6533.	6520	0.0000	0.72	Γ_3
$^3H_5$	6332.		1.2806		Γ_4
$^3H_5$	6296.	6080	0.0000	0.70	Γ_3
$^3H_5$	6059.		0.0000		Γ_2
$^3F_2$	4964.		2.6821		Γ_1
$^3F_2$	4826.		2.4950		Γ_1
$^3F_2$	4727.		0.0000		Γ_3
$^3F_2$	4580.		2.2483		Γ_4
$^3F_2$	4572.		0.0000		Γ_2
$^3H_4$	2179.		1.3987		Γ_4
$^3H_4$	2120.		0.0000		Γ_3
$^3H_4$	1669.		0.9005		Γ_1
$^3H_4$	1406.		0.0000		Γ_2
$^3H_4$	903.		0.1431		Γ_1
$^3H_4$	775.		0.0000		Γ_3
$^3H_4$	735.		0.0000		Γ_2
$^3H_4$	643.		0.0152		Γ_4
$^3H_4$	0.		0.0000		Γ_1

7.2.2 Europium(III)-compounds

Table A5. AOM parameters e_σ and e_π for thedifferent d(Eu-L) (L: O, Cl).

Compound	Ligand	d(Eu-L)	e_σ(Eu-L)	e_π(Eu-L)
$EuPO_4$	O4	2.380	404.0	101.0
	O3	2.383	400.5	100.1
	O1	2.386	397.0	99.2
	O4'	2.457	323.3	80.8
	O2	2.475	307.2	76.8
	O1'	2.476	306.3	76.6
	O3'	2.494	299.5	74.9
	O2'	2.583	227.8	57.0
	O2''	2.777	137.2	34.3
$EuSbO_4$ [a)]	O1	2.263	977.47	244.37
	O4	2.282	921.91	230.48
	O4'	2.311	843.91	210.98
	O2	2.386	674.85	168.85
	O1'	2.397	653.46	163.37
	O4''	2.536	440.41	110.10
	O3	2.626	345.01	86.25
	O1''	2.859	190.28	47.57
$EuAsO_4$	O1	2.350	441.5	110.4
	O2	2.466	315.1	78.8
$EuVO_4$	O1	2.356	433.7	108.4
	O1'	2.470	311.6	77.9
Eu_2O_3 [a)]	O1 (Eu1)	2.304	862.0	215.51
	O1'(Eu2)	2.287	907.9	226.97
	O1 (Eu2)	2.342	768.8	192.19
	O1''(Eu2)	2.425	602.4	150.61
$Eu_2Ti_2O_7$ [b)]	O2	2.210	882.4	220.6
	O1	2.517	355.0	88.7
EuOCl	O1	2.286	535.7	133.9
	Cl'	3.080	142.4	35.6
	Cl	3.107	134.0	33.5
$EuNbO_4$ [c)]	O2	2.366	589.5	147.4
	O1	2.421	560.7	140.2
	O2'	2.383	501.9	125.5
	O1'	2.456	453.9	113.5
$EuTaO_4$ [c)]	O2	2.366	589.5	147.4
	O1	2.416	535.0	133.8
	O2'	2.399	509.2	127.3
	O1'	2.508	392.0	98.0

[a] $e_{\sigma,\,norm}(Eu\text{-}O)_{2.38\ Å}$ increased by a factor of 1.7 relative to $e_{\sigma,\,norm}(Eu\text{-}O)_{2.38\ Å}$ in $EuPO_4$;
[b] $e_{\sigma,\,norm}(Eu\text{-}O)_{2.38\ Å}$ increased by a factor of 1.3 relative to $e_{\sigma,\,norm}(Eu\text{-}O)_{2.38\ Å}$ in $EuPO_4$;
[c] $e_{\sigma,\,norm}(Eu\text{-}O)_{2.38\ Å}$ increased by a factor of 1.4 relative to $e_{\sigma,\,norm}(Eu\text{-}O)_{2.38\ Å}$ in $EuPO_4$;

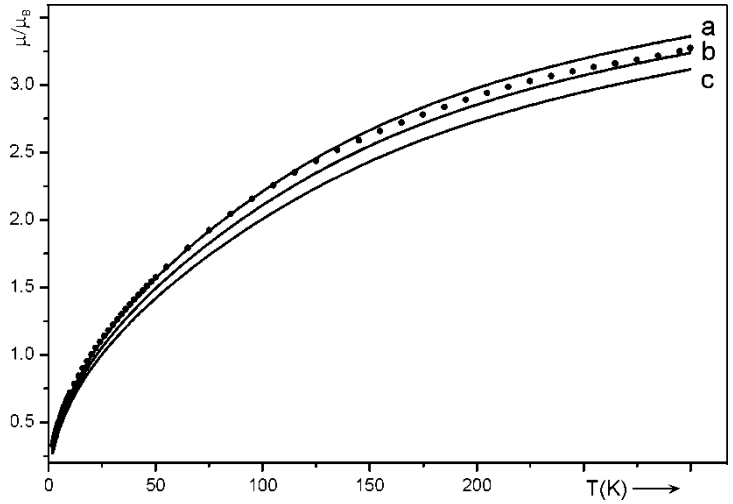

Figure A1. Variation of μ/μ_B vs. T for $EuPO_4$ with k in comparison to the observed temperature dependence. a) k = 0.95, b)) k = 1.0, c)) k = 1.05.

7.2.3 Calculation of the transition energies and ligand field splitting of $Cs_2NaLnCl_6$

Table A6. AOM parameters used for the calculations of the transitions energies for *Ln* in $Cs_2NaLnCl_6$. $e_\sigma : e_\sigma = 1/3$. e_σ, e_π in cm^{-1}.

Ln^{3+}	Ce	Pr	Nd	Pm	Sm	Eu	Gd	Tb	Dy	Ho	Er	Tm	Yb
e_σ	420	410	390	-	340	380	-	330	320	310	280	280	270
e_σ	140	136.7	130	-	113.3	126.7	-	110	106.7	103.3	93.3	93.3	90

12.3 List of figures

12.4 List of tables

13 References

[1] A. F. Holleman, E. Wiberg, N. Wiberg, *Lehrbuch der Anorganischen Chemie*, Walter de Gruyter, Berlin, 102. Auflage, **2007**.

[2] M. Sagawa, S. Fujimura, N. Togawa, H. Yamamoto, Y. Matsuura, *J. Appl. Phys*. **1984**, *55*, 2083.

[3] U. Müller, *Anorganische Strukturchemie*, Teubner, Stuttgart, **2011**.

[4] W. A. J. Velge, K. H. J. Buschow, *J. App. Phys*. **1968**, *39*, 1717.

[5] H. Yamamoto, *Rare Earths '04 Nara (Japan)*, Book of Abstracts FI01, **2004**.

[6] H. Shinjoh, *Rare Earths '04 Nara (Japan)*, Book of Abstracts HI01, **2004**.

[7] K. Mikami, H. Terada, H. Matsuzawa, *Angew. Chemie* **2002**, *41*, 35544.

[8] J. Bille, W. Schlegel, *Medizinische Physik 3*, *Medizinische Laserphysik*, Springer, Berlin, **2005**.

[9] C. F. G. C. Geraldes, *Rare Earths '04 Nara (Japan)*, Book of Abstracts CO02, **2004**.

[10] R. D. Shannon, *Acta Crystallogr. A* **1976**, *32*, 751.

[11] W. Klemm, *Magnetochemie*, Akademischer Verlag, Leipzig, **1936**.

[12] H. van Vleck, *The Theory of Electric and Magnetic Susceptibilities*, Oxford University Press, London, **1932**.

[13] S. T. Hatscher, H. Schilder, H. Lueken, W. Urland, *Pure Appl. Chem*. **2005**, *77*, 497.

[14] B. N. Figgis, M. A. Hitchman, *Ligand Field Theory and Its Applications*, Wiley-VCH New York, **2000**.

[15] H. Bethe, *Ann. Physik* **1929**, *3*, 133.

[16] A. B. P. Lever, *Inorganic electronic spectroscopy*, Elsevier, New York, **1998**.

[17] E. Riedel, *Anorganische Chemie*, Walter de Gruyter, Berlin, New York, **2007**.

[18] F. A. Cotton, *Chemical Applications of Group Theory*, John Wiley & Sons New York, **1990**.

[19] H. Thauern, *PhD thesis*, University of Bonn, **2006**.

[20] W. Urland, E. J. Zehnder, R. Kremer, *Chem. Phys. Lett* **1984**, *106*, 417.

[21] W. Urland, H. Gunsilius, G. Kliche, *Z. Allg. Anorg. Chem*. **1987**, *553*, 90.

[22] D. Manthey, *Programm Orbital Viewer V1.04*, Florida, **2004**.

[23] W. Urland, *Chem. Phys. Lett*. **1977**, *46*, 457.

[24] W. Urland, *Chem. Phys*. **1976**, *14*, 393.

[25] W. Urland, *Chem. Phys. Lett*. **1977**, *50*, 445.

[26] M. Gerloch, R. Slade, *Ligand Field Parameters*, Cambridge Univ. Press, **1973**.

[27] Orbitron, University of Sheffield, http://winter.group.shef.ac.uk/orbitron/AOs/4f/, 2017.

[28] R. Glaum, *Thesis of Habilitation*, University of Gießen, **1999**. URL: http://bibd.uni-giessen.de/gdoc/1999/uni/h990001b.htm

[29] K. W. H. Stevens, *Proc. Roy. Soc.***1954**, *A219*, 542.

[30] E. U. Condon, G. H. Shortley, *The Theory of Atomic Spectra*, Cambridge Univ. Press **1967**.

[31] L. H. Gade, *Koordinationschemie*, Wiley-VCH **1998**.

[32] S. Minomura, H. G. Drickamer, *J. Chem. Phys*. **1961**, *35*, 903.

[33] H. G. Drickamer, C. W. Frank, *Electronic transitions and the High Pressure Chemistry and Physics of Solids*, Chapman and Hall, London **1973**.

[34] D. Reinen, M. Atanasov, S.-L. Lee, *Coord. Chem. Rev*. **1998**, *175*, 91.

[35] B. G. Wyborne, J. Chem. Phys. 1962, 36, 2301.

[36] J. B. Goodenough, *Magnetism and the Chemical Bond*, Interscience Publ., New York, **1963**.

[37] P. J. Hay, J. C. Thibeault, R. Hoffmann, *J. Am. Chem. Soc.* **1975**, 4884.

[38] D. Heiman, *Nanomagnetism*, Northeastern University, **2009**.

[39] O. Kahn, *Molecular Magnetism*, Wiley-VCH, **1993**.

[40] H. Lueken, *Magnetochemie*, Teubner, **1999**.

[41] R. S. Mulliken, *J. Phys. Chem.* **1962**, *66*, 2306.

[42] R.S. Mulliken, *J. Phys. Chem.* **1955**, *23*, 1833.

[43] R. S. Mulliken, *J. Am. Chem. Soc*. **1952**, *74*, 811.

[44] W. Urland, K. Feldner, R. Hoppe, *Z. Anorg. Allg. Chem*. **1980**, *465*, 7.

[45] H. E. Housecroft, A. Sharpe, *Anorganische Chemie*, 2th edition, Pearson, **2006**.

[46] H. Lincke, T. Nilges, R. Pöttgen, *Z. Anorg. Allg. Chem*. **2006**, *632*, 1804.

[47] R. Glaum, R. Gruehn, M. Möller, *Z. Anorg. Allg. Chem*. **1986**, *543*, 111.

[48] S. Tanabe, Y. Sugano, *J. Phys. Soc. Japan* **1954**, *9*, 753.

[49] H. Lincke, T. Nilges, R. Pöttgen, *Z. Anorg. Allg. Chem*. **2006**, *632*, 1804.

[50] M. Stichnote, *Diploma thesis*, University of Bonn, **2011**.

[51] A. Carrington, A. D. Mclachlan, *Introduction to Magnetic Resonance With Applications to Chemistry and Chemical Physics; Chapter 5/7/9*, A Science paperback, Cambridge, **1983**.

[52] M. H. L. Pryce, *Proc. Chem. Soc* **1950**, *A63*, 25.

[53] M. Kaupp, M. Bühl, V. G. Malkin, *Calculation of NMR and EPR Parameters: Theory and Applications*, Wiley-VCH Verlag, **2014**.

[54] E. Krausz, *Aust. J. Chem*. **1993**, *46*, 1041.

[55] E. Krausz, *AOS news* **1998**, *12*, 21.

[56] P. Kubelka, F. Munk., *Z. Techn. Phys.* **1931**, *12*, 593.

[57] M. Gerk, *Ph. D. thesis*, University of Gießen, **1996**.

[58] W. Buckel, *Supraleitung*, VCH Verlagsgesellschaft, Weinheim, 5th edition, **1993**.

[59] A. Bronova, *Master thesis*, University of Bonn, **2013**.

[60] W. Urland, *Thesis of Habilitation*, University of Gießen, **1980**.

[61] C. K. Jørgensen, R. Pappalardo, H.-H. Schmidtke, *J. Chem. Phys*. **1963**, *39*, 1422.

[62] E. Larsen, G. N. LaMar, *J. Chem. Ed*. **1974**, *51*, 633.

[63] D. E. Richardson, *J. Chem. Ed.* **1993**, *70*, 372.

[64] M. Gerloch, D. J.Mackey, *J. Chem. Soc*. *A* **1970**, 3030.

[65] M. Gerloch, D. J.Mackey, *J. Chem. Soc*. *A* **1970**, 3040.

[66] M. Gerloch, D. J.Mackey, *J. Chem. Soc*. *Dalton Trans*. **1972**, 1555.

[67] C. W. Nielson, G. F. Koster, *Spectroscopic Coefficients for p^n, d^n and f^n Configurations*, Cambridge MIT Press, **1963**.

[68] M. Gerloch, *Magnetism and Ligand Field Theory*, Cambridge Univ. Press, **1983**.

[69] M. Gerloch, R. F. McMeeking, *J. Chem. Soc. Dalton* **1975**, 2443.

[70] M. Riley, *Inorg. Chim. Acta* **1998**, *268*, 55.

[71] G. H. Dieke, *Spectra and energy levels of rare earth ions in crystals*, Interscience Publishers, New York, **1968**.

[72] R. N. Zare, *Angular Momentum*, Wiley & Sons, New York, **1988**.

[73] T. Damhus, *Ph. D. Thesis*, Univesity of Copenhagen, **1984**.

[74] F. A. Cotton, *Chemical applications of group theory*, Wiley & Sons, New York, **1990**.

[75] S. Sugano, Y. Tanabe, H. Kamimura, *Multiplets of Transition.Metal Ions in Crystals*, Academic Press, New York, *1970*.

[76] B. Henderson, G. F. Imbusch, *Optical spectroscopy of inorganic solids*, Clarendon Press, Oxford, **2006**.

[77] G. F. Koster, J. O. Dimmock, R. G. Wheeler, H. Statz, *Properties of the thirty.two point groups*, MIT Press, Cambridge Massachusetts, **1963**.

[78] T. Fließbach, *Mechanik*, 5th edition, Elsevier/Spektrum Akademischer Verlag, München, **2007**.

[79] S. T. Thorton and J. B. Marion, *Classical Dynamics of Particles and Systems*, 5th edition, Cengage Learning, **2003**.

[80] S. Hüfner, *Optical Sectra of Transparent Rare Earth Compounds*, Academic Press New York, **1978**

[81] M. Tinkham, *Group theory and quantum mechanics*, Dover Publications Inc, NY, **2004**.

[82] David Bishop, *Group theory and chemistry*, Dover Publications Inc, NY, **1993**.

[83] B. R. Judd, *Phys. Rev.*. **1962**, *127*, 750.

[84] G. S. Ofelt, *J. Chem. Phys*. **1962**, *37*, 511.

[85] M. J. D. Powell and R. Orbach, *Proc. Phys. Soc*. **1961**, *78*, 753.

[86] B. R. Judd, *Proc. Roy*. **1957**, *A241*, 414.

[87] C. W. Nielson, G. F. Koster, *Spectroscopic Coefficients for p^n, d^n and f^n Configurations*, Cambridge MIT Press, **1963**.

[88] M. Rotenberg, R. Bivens, N. Metropolis, J. K. Wooten, *The 3-j and 6-j Symbols*, Cambridge MIT Press, **1964**.

[89] W. F. Kruppke, *Phys. Rev.*. **1966**, *145*, 325.

[90] R. P Leavitt and C. A. Morrison, *J. Chem. Phys*. **1980**, *73*, 749.

[91] M. J. Weber, *Phys. Rev*. **1967**, *157*, 262.

[92] M. J. Weber, *Optical Properties of Ions in Crystals*, Wiley Interscience, NY, **1967**.

[93] M. J. Weber, B . H. Matsinger, V. L. Donlan, J. T. Surratt, *J. Chem. Phys*. **1972**, *57*, 562.

[94] F. Neese et al., ORCA 4.0, *An ab initio, DFT and semiempirical SCF-MO package*, MPI Mülheim, **2017**.

[95] D. Aravena, F. Neese, D. A. Pantazis, *J. Chem. Theory Comput.* **2016**, *12*, 1148.

[96] D. Aravena, M. Atanasov, F. Neese, *Inorg. Chem*. **2016**, *55*, 4457.

[97] J. Sugar, *Phys. Rew. Lett*. **1965**, *14*, 731.

[98] G. S. Ofelt, *J. Chem. Phys*. **1963**, *38*, 2171.

[99] M. H. Crozier, W. A. Runciman, *J. Chem. Phys*. **1961**, *35*, 1392.

[100] Atomic Energy Levels – The Rare-Earth Elements, W. C. Martin, R. Zalubas, and L. Hagan, in Nat. Stand. Ref. Data Ser., NSRDS-NBS 60, 422 pp. (Nat. Bur. Stand., U.S., **1978**).

[101] F. S. Richardson, M. F. Reid, J. J. Dallara, R. D. Smith, *J. Chem. Phys.* **1985**, *83*, 3813.

[102] W. Urland, *Chem. Phys. Lett.* **1981**, *83*, 116.

[103] D. Aravena, M. Atanasov, F. Neese, *Inorg. Chem*. **2016**, *55*, 4457.

[104] M. Atanasov, D. Ganyushin, K Sivalingam, F. Neese, Molecular Electronic structures of Transition Metal Complexes II. *In Structure and Bonding Vol. 143*, Springer, Berlin Germany, **2012**.

[105] B. T. M. Willis, *Acta Crystallog*. **1965**, *18*,75.

[106] R. Ubic, I. Abrahams,y, Y. Hu, *J. Am. Ceram. Soc*. **2008**, *91*, 235.

[107] J. H. Chun and R. Kremer, *personal communication*, University of Stuttgart, **2013**.

[108] F. S. Richardson, M. F. Reid, J. J. Dallara, R. D. Smith, *J. Chem. Phys.* **1985**, *83*, 3813.

[109] F. Hund, *Z. Physik* **1927**, *40*, 742.

[110] A.Landé, *Z. Physik* **1923**, *15*, 189.

[111] S. Golbs, F. M. Schappacher, R. Pöttgen, R. Cardoso.Gil, A. Ormeci, U. Schwarz, W. Schnelle, Y. Grin, M. Schmidt, *ZAAC* **2013**, *12*, 2139.

[112] K. Binnemans, *Coord. Chem. Rev***. 2015**, *295*, 1.

[113] a) Y. Yang and N. L. Huang Lu, *Conf. Proceed.* 1972, *5*, 801.

[114] N. L. Huang Lu, J. H. van Vleck, *J. App. Phys.* 1969, *40*, 1144.

[115] T. Aitasalo, J. Hölsä, M. Latsusaari, J. Legendziewicz, L. Lehto, J. Linden, M Marysko, *J. Alloys and Comp.* **2004**, *380*, 296.

[116] E. D. Jones, *J. Appl. Phys.* **1968**, *39*, 1090.

[117] N. Kannengießer, *part of planned Ph. D thesis.*,University of Bonn.

[118] D. F. Mullica, D. A. Grossie, L. A. Boatner, *Inorg*. *Chim. Acta* **1985**, *109*, 105.

[119] S. Golbs, R. Cardoso-Gil, M. Schmidt, *Z. Kristallogr*. **2009**, *224*, 169.

[120] D: F. Mullica, E. L. Sappenfield, M. M. Abraham, B. C. Chakoumakos and L. A. Boatner, *Inorg. Chim. Acta*. **1996**, *248*, 127.

[121] H. Bärnighausen, G. Brauer, N. Schultz, *Z. Anorg. Allg. Chem*. **1965**, *338*, 250.

[122] C. Keller, *Z. Allg. Anorg. Chem.* **1962**, *318*, 89.

[123] E. Chtoun, L. Hanebali, P. Garnier, J. M. Kiat, *Eur. J. Sol. St. Chem.*. **1997**, *34*, 553.

[124] S. Gerlach, R. Cardoso-Gil, E. Milke, M. Schmidt, *Z. Anorg. Allg. Chem*. **2007**, *633*, 83.

[125] Z. K. Heiba, Y. Akin, W. Sigmund, Y. S. Hascicek, *J. Appl. Crystalogr*. **2003**, *36*, 1411.

[126] G. S. Ofelt, *J. Chem. Phys.* **1963**, *38*, 2171.

[127] W. Urland, *Chem. Phys. Let*. **1981**, *83*, 116.

[128] R. Bazzi, M. A. Flores, C. Louis, K. Lebbou, W. Zhang, C. Dujardin, S. Roux, B. Mercier, G. Ledoux, E. Bernstein, P. Perriat, O. Tillement, *J. Col. Inter. Sci*. **2004**, *273*, 191.

[129] G. D. Del Cul, G. M. Murray, J. R. Peterson. *Eur. J. Sol. St. Chem.* **1996**, *28*, 155.

[130] K. Qiu, J. Li, J. Li, X. Lu, Y. Gong, J. Li, *J. Mater. Sci*. **2010**, *45*, 5456.

[131] J. D. Cashion, A. H. Cooke, M. J. M. Leask, T.L. Thorp, M. R. Wells, *J. Mat. Sci.* **1968**, *3*, 402.

[132] P. Dasgupta, Y. M. Jana, A. Nag Chattopadhyay, R. Higashinaka, Y. Maeno, D. Ghosh, *J. Phys. Chem.* **2007**, *68*, 347.

[133] P.Caro and P. Porcher, *J. Magn. Mat*. **1986**, *58*, 61.

[134] M. Crosswhite, H. Crosswhite, F. W. Kaseta, R. Sarup, *J. Chem. Phys*. **1976**, *64*, 1981.

[135] W. T. Carnall, H. Crosswhite, H. M. Crosswhite, J. G. Conway, *ibid* **1976**, *64*,3582.

[136] H. M. Crosswhite, H. Crosswhite, N. Edelstein, K. Rajnak, *ibid*., **1976**, *67*, 3002.

[137] W. T. Carnall, J. V. Beitz, H. Crosswhite, K. Rajnak, J. B. Mann, *in Systematics and the Properties of Lanthanides*, edited by S. P. Sinha, Reidel, Boston, **1983**.

[138] W. T. Carnall, H. Crosswhite, H. M. Crosswhite, *Argonne National Laboratory Report*, **1977**.

[139] M. Faucher, D. Garcia, C. K. Jørgenson, *Chem. Phys. Let*. **1986**, *129*, 387.

[140] C. Goerller-Walrand, K. Binnemans, *In Handbook on the Physics and Chemistry of Rare Earths Vol 21*., L. Eyring, K. A. Gschneidner, Amsterdam : North-Holland, **1995.**

[141] W. Urland, *Z. Naturforschung*. **1980**, *35*, 247.

[142] J. A. Duffy, *Bonding. Energy Levels & Bands in Inorganic Solids*, Longman Scientific & Technical, **1990**.

[143] J. A. Duffy, M. D. Ingram, *J. Am. Chem. Soc.* **1971**, 6448.

[144] X. Zhao. X. Wamg, H. Lin, Z. Wang, *Physica.* **2007**, B392, 132.

[145] A. Lebouteiller, P. Courtine, *J. Sol. St. Chem.* **1998**, *137*, 94.

[146] F. Hulliger, *J. Magn. Magn. Mat*. **1978**, *8*, 83.

[147] A. Bronova, R. Glaum, T. Bredow and W: Urland, *Inorg. Chem*. **2016**, *55*, 6853.

[148] A. Bronova, T. Droß, R. Glaum, A. Kostencki, H. Lueken, A. Rhode, M. Speldrich, W. Urland, *Inorg. Chem*. **2016**, *55*, 6848.

[149] T. Dross, *Dissertation*, University of Bonn, **2004**.

[150] R. A. Satten, C. L. Schreiber, E. Y. Wong, *J. Chem. Phys* **1965**, *42*, 162.

[151] J. F. Wyart, V. Kaufman, J. Sugar, *Phys. Scripta* **1980**, *22*, 389.

[152] K. W. H. Stevens, *Proc. Roy. Soc*.**1954**, *A219*, 542.

[153] S. Hüfner, *Optical Sectra of Transparent Rare Earth Compounds*, Academic Press New York, **1978**.

[154] A. Cabeza et. al. *J. Solid St. Chem*. **1996**, *121*, 181.

[155] T. Schleid, G. Meyer, L. R. Morss, *J. Less-Com. Met*. **1987**, *132*, 69.

[156] K. D. Warren, *Inorg. Chem*. **1977**, *16*, 2008.

[157] Z. Gajek, J. Mulak, *J. Solid St. Chem*. **1993**, *107*, 413.

[158] Z. Gajek, *J. Magn. Magnet. Mat*. **2004**, 272.

[159] Z. Gajek, *J. Magn. Magnet. Mat*. **1988**, *76*, 363.

[160] Z. Gajek, J. Mulak, *J. Phys. Cond. Matter* **1992**, *4*, 427.

[161] D. A. Skoog, J. Holler, S. R. Crouch, *Principles of Instrumental Analysis*, Brooks/Cole Boston, 2006.

[162] C. Goerller-Walrand, K. Binnemans,. In *Handbook on the Physics and Chemistry of Rare Earths Vol 23*, K. A. Gschneidner, L. Eyring, Eds., North-Holland, Amsterdam, **1996**.